A STUDY OF CLOUD FRACTION AS A FUNCTION OF OPTICAL DEPTH USING UNIVERSITY OF WISCONSIN LIDAR DATA

By

Michael V. Mores

A thesis submitted in partial fulfillment
of the requirements for the degree of

Master of Science
(Atmospheric and Oceanic Sciences)

at the

University of Wisconsin – Madison

2004

Approved by: _____ _____

Steven A. Ackerman — Date

Professor of Atmospheric and Oceanic Sciences
Advisor

A STUDY OF CLOUD FRACTION AS A FUNCTION OF OPTICAL DEPTH USING UNIVERSITY OF WISCONSIN LIDAR DATA

by Michael V. Mores

Abstract

Thin cirrus clouds have interested and concerned scientists for decades due to the large global coverage and the incomplete understanding of the total radiative properties. Optical depth and height determination of these thin clouds has proven troublesome for scientists using satellite-derived data (such as MODIS) due to the small amount of reflected solar radiation. Studies have shown that when thin cirrus is present, satellites often classify these clouds as lower level clouds or render the clouds undetectable (Wylie 1989). Although the field of view is much smaller than the global coverage of a weather satellite, active remote sensing instruments such as lidar are excellent candidates for retrieving accurate optical depth and height information due to the superior vertical resolution and the ability to detect thin cirrus not detectable by satellites. By using various optical depth thresholds, the amount of cloud cover can be determined for an optical depth lower limit such as 1.0, 0.5, or 0.1. This information can then be used to determine the relative cloud fraction that an instrument may not be detecting.

The purpose of this study is to calculate the cloud fraction as a function of various optical depth thresholds using data taken from the University of Wisconsin Arctic High Spectral Resolution Lidar. Results from this study show that over the course of a year when lidar data was gathered at the University of Wisconsin – Madison, there was a 15% increase in the amount of detected cloud cover between an optical depth lower threshold of 2 and that of 0.05. Also found in this study is that for a given cloud fraction, various optical depth limits show as much as a three kilometer difference in altitude when viewing the clouds from above.

This study of cloud classification based on optical depth thresholds has shown promising results for future work. Research of this type is useful for scientists calculating the lower optical depth limit of an instrument in orbit as well as validating the percentage of cloud fraction the satellite can view over a given month or season.

Acknowledgements

I would first like to thank my advisors Ed Eloranta and Steve Ackerman for the support and encouragement that allowed me to finish this thesis. Ed was most insightful when it came to developing informative plots while Steve gave me advice on my written work and taught me the significance of writing through all of my research. Other thanks go out to my professors and readers Dr. Pao Wang and Dr. Ralf Bennartz.

This work would not have been done if it weren't for the impressive engineering skills and work ethic of Jim Hedrick, Igor Razenkov, and Joe Garcia. Each of them is an expert in their respective field, and together they were able to create the autonomous lidar that provided the data used in this thesis. I would not have been able to collect data without them.

Finally, I would like to thank my family and friends. Thanks to Gijs deBoer and Rebecca Flood for the helpful talks, kindness, and being the great roommates they are. Thanks to my parents, Mike and Cheri, for without their support, I would not have gotten this far in my education. Finally, a thank you goes to my girlfriend, Rebecca Fredericks, for all of her love and dedication since the day we met.

Table of Contents

Chapter		Page
1	**Introduction**	**1**
	1.1 Scientific Motivation	1
	1.2 Satellite Cloud Detection Techniques	2
	1.3 Lidar Cloud Detection	4
	1.4 Thesis Overview	5
2	**Lidar Measurements**	**6**
	2.1 Introduction	6
	2.2 The Single Channel Lidar Equation	7
	2.3 The High Spectral Resolution Lidar	9
	2.4 Calibration of AHSRL Data	12
	2.5 AHSRL Atmospheric Measurements	15
	2.6 Assessment of Photon Counting and Calibration Errors	22
	2.6.1 Description of Multiple Scattering	24
	2.6.2 Photon Counting and Calibration Errors	25
3	**Defining Clouds Based on Optical Depth Thresholds**	**28**
	3.1 Introduction	28
	3.2 Cloud Boundaries Based on Aerosol Backscatter Thresholds	30
	3.3 Cloud Boundaries Based on Optical Depth Thresholds	38
4	**Cloud Fraction as a Function of Optical Depth**	**43**
	4.1 Introduction	43
	4.2 Cloud Fraction	43
	4.3 Temporal and Spatial Average Comparison	48
	4.4 Optical Depth Error Estimates	51
	4.5 Additional Case Studies	53
	4.5.1 February 16th, 2004	53
	4.5.2 May 15th, 2004	59
5	**Results of a Twelve-Month Study and Discussion**	**62**
	5.1 Cloud Percentage over Twelve Months of Lidar Data	62

5.2 Optical Depth Results as a Function of Altitude..... 64
5.3 Distribution of Cloud Phases Over Twelve Months of Data..... 68
5.4 Comparison with ASOS Observations at the Dane County Airport..... 70
6 Summary and Future Work..... **73**
References..... **75**
Appendix A: Instrumentation..... **79**
Appendix B: Results from each month..... **81**

List of Figures

Figure	Page
2.1 Attenuated backscatter from April 4th, 2004, from 2-10 UTC	8
2.2 Spectral diagram of the HSRL transmitter and receiver	10
2.3 Aerosol backscatter for April 4th, 2004, from 2-10 UTC	12
2.4 Top view of the AHSRL	13
2.5 The AHSRL with protective housing removed	14
2.6 Time averaged plot of optical depth for April 4th, 2004	17
2.7 Time averaged plot of the scattering ratio for April 4th, 2004	18
2.8 Time averaged plot of the aerosol and molecular backscatter returns for April 4th, 2004	19
2.9 Circular depolarization ratio for April 4th, 2004	21
2.10 Cloud phase definition table	23
2.11 Cloud phase RTI figure for April 4th, 2004	23
2.12 Sample optical depth profile with error bars for April 20th, 2004, at 10 UTC	27
3.1 Aerosol backscatter and depolarization for April 24th, 2004	31
3.2 Aerosol backscatter for a single time bin	33
3.3 Cloud boundaries based on a backscatter threshold for April 24th, 2004	34
3.4(A-D) Cloud boundaries based on multiple backscatter thresholds for April 24th, 2004	36
3.5 Optical depth profile for a single time bin	39
3.6 Cloud boundaries based on an optical depth threshold for April 24th, 2004	40
3.7 Cloud boundaries based on multiple optical depth thresholds for April 24th, 2004	41
4.1 Cloud optical depth vs. time profiles and phase information for April 24th, 2004	44
4.2 Total sorted optical depth for April 24th, 2004	46
4.3 Cloud percentage as a function of optical depth thresholds for April 24th, 2004	47
4.4 Temporal resolution comparison plot for June 2004	49
4.5 Spatial resolution comparison plot for June 2004	50
4.6 Total cloud fraction, plus sigma cloud fraction, and minus cloud fraction for June 2004	52
4.7 Aerosol backscatter and depolarization for February 16th, 2004	54
4.8 February 16th, 2004 plot of multiple optical depth thresholds	55
4.9 Optical depth and phase information for February 16th, 2004	56

4.10 Cloud fraction for February 16th, 2004..... 57
4.11 Aerosol backscatter and depolarization for May 15th, 2004..... 58
4.12 May 15th, 2004 plot of multiple optical depth thresholds..... 59
4.13 Optical depth and phase information for May 15th, 2004..... 60
4.14 Cloud fraction for May 15th, 2004..... 61
5.1 Cloud percentage as a function of optical depth thresholds for twelve months..... 63
5.2 Cloud fraction looking from ground up for twelve months..... 65
5.3 Cloud fraction looking from sky down for twelve months..... 67
5.4 Distribution of ice vs. water for a year's worth of data..... 69
5.5 Hours of data in each month..... 71
5.6 Cloud fraction for each month along with Dane County Airport Observations..... 72
Appendix 2 Cloud fraction results for each of the twelve months in this study..... 83

Chapter 1

INTRODUCTION

1.1 Scientific Motivation

Upper level ice clouds come in several forms including thin cirrus, cirrostratus, cirrus incinus, and contrails. Liou (1986) theorized that cirrus and cirrostratus are most likely associated with either high-pressure systems or upper-level troughs, while cirrus uncinus are related to either mesoscale or larger-scale synoptic disturbances. Studies have shown that upper level clouds have a considerable impact on the radiative budget of the earth (Cox 1971, Liou 1986, Wylie 1989, Stephens 1990, Sassen 2001 Part II). Thin, partially transmissive cirrus in the upper troposphere transmit incoming solar shortwave radiation, while reducing the outgoing terrestrial radiation to space, therefore potentially warming the earth (Stephens 1990, Wylie 1995). However, the impact of this warming or cooling is also a function of the particle size. Many research programs using multiple instruments have investigated the radiative properties of cirrus clouds, including the ISCCP (International Satellite Cloud Climatology Project), FIRE (First ISCCP Regional Experiments), and ARM (Atmospheric Radiation Measurement).

Improving our basic knowledge of cirrus cloud properties would benefit the large scale models used to simulate the effects of cirrus clouds on climate and possible feedbacks to climate change (Sassen 2001 Part II). Sassen (2000 Part I) wrote that the "dominance of infrared greenhouse warming verses solar albedo cooling depends sensitively on both the heights and microphysical compositions of the modeled cirrus." Thirty years prior, Platt (1973) noted that "a value of [optical depth] is important, as all theoretical computations of visible scattering in

clouds relate the cloud albedo to its optical thickness, and if one could obtain the infrared emissivity and shortwave albedo of cirrus, this would allow a full description of the radiative effect of the cloud." To do this, scientists must understand more about the radiative cloud properties of cirrus clouds and how these cloud properties are coupled to the cloud microphysical and macrophysical properties, such as effective particle size, optical depth, emissivity, and average cloud height.

1.2 Satellite Cloud Detection Techniques

With the functional use of weather satellite data, many studies have estimated cirrus cloud global coverage. Wylie et al. (1998) found throughout an eight-year study using the High Resolution Infrared Radiation Sounder (HIRS) that cirrus and transmissive clouds were found in 42-44% of global observations. Estimates of cloud optical thickness suggest that 50% of detected cirrus has an optical depth of less than or equal to 0.3 (Sassen 2000 Part I). Data analysis of thin cirrus cases shows that these clouds are often mistaken for lower-level clouds or not even detected (Wylie 1989, Baum 2003, Platnik 2003). These upper level clouds are especially hard to identify on visible satellite images because little solar radiation is reflected and the clouds appear dark or broken (Wylie 1989).

Due to its multispectral capabilities, the 36 channel Moderate Resolution Imaging Spectroradiometer (MODIS) combines multiple cloud detection approaches. The MODIS cloud mask indicates whether a given view of the earth's surface is unobstructed by clouds or optically thick aerosol (Ackerman et al 1998). The current cloud mask contains 48 bits of information for

each pixel, although for most applications one only needs the first 8 bits. One bit warns that thin cirrus might be present, even though the final mask product may show no obstruction.

Development of the MODIS cloud mask algorithm is based on previous research to characterize global cloud cover (Ackerman et al 1998). For example, the ISCCP algorithm indicates only two types of conditions: cloudy and clear. This algorithm is based on a series of thresholds in the 0.6 and the 11-micron channels, where each value is compared to its corresponding clear-sky composite value. Ambiguity in this method is caused by both measurement errors and natural variability (of the clear sky composite) while the thresholds are based on uncertainty values in the radiance estimates. This method of cloud detection minimizes false detections, but may miss thin clouds that resemble clear sky conditions.

Another approach, the NOAA Cloud Advanced Very High Resolution Radiometer (CLAVR) algorithm, uses five spectral channels of the Advanced Very High Resolution Radiometer (AVHRR) to derive a cloud mask. This method applies various cloud tests to arrays of pixels, and depending on the number that pass the tests, the array is labeled a percentage of "cloudy" or "clear". This algorithm can also distinguish between a number of cloud types, including low stratus, thin cirrus, and deep convective cloud systems (Ackerman et al 1998).

CO_2 slicing (Wylie et al. 1995) is a method of distinguishing transmissive clouds from opaque clouds and clear-sky using HIRS data. Using radiances within the broad CO_2 absorption band around 15 μm, clouds at various levels of the atmosphere can be detected. This method is useful for detecting thin cirrus clouds that are often missed by simple infrared and visible approaches. Problems may arise in this algorithm, however, when the difference between clear sky and cloud radiance for a spectral band is less than the instrument noise (Ackerman et al 1998). Due to problems associated with the CO_2 slicing method of determining cloud height,

cloud height accuracy increases as the cloud optical thickness increases and is most problematic for optically thin cirrus (Baum 2003).

1.3 Lidar Cloud Detection

While passive remote sensing instruments on satellites are capable of providing a global picture of the aerosol optical thickness, the instruments cannot retrieve the necessary vertical dimension necessary for the study of cloud transport and evolution (Léon 2003). Active remote sensing instruments such as radar (radio detection and ranging) and lidar (light detection and ranging) have a greater vertical sensitivity and can provide detailed measurements of the cloud height and a number of optical properties. Lidar observations from both sides of clouds (ground based and airborne) indicate that cirrus do not have distinct boundaries at their tops (Wylie 1989), and often have large variances in density. These two characteristics give cirrus a variable cloud top height and cause complications for passive instruments of low or moderate resolution.

The University of Wisconsin Arctic High Spectral Resolution Lidar (UW-AHSRL) (Eloranta 2003) has been in continuous operation since the summer of 2003 from a rooftop located in Madison, WI. This autonomous system is capable of measuring aerosol backscatter cross-section, altitude, thickness, and optical depth at a 7.5 m vertical resolution. While this type of resolution and accuracy is unmatched by current satellite retrievals, the measurements are limited to only what passes directly over the system due to the small field of view. Although they lack the global coverage present in satellite passive remote sensing techniques, instruments such as lidar are often considered "truth" due to their superior vertical resolution with regards to the aerosol backscatter, cloud particle phase, and optical depth (Frey, et al. 1999). Much research

has been done in the last thirty years on validating satellite retrievals when thin cirrus is present (e.g., Smith and Platt 1978, Wylie and Menzel 1989, Smith and Frey 1990).

As mentioned previously, instruments such as the AVHRR and MODIS have difficulty detecting thin cirrus clouds. From analyzing lidar data, it is possible to detect and classify clouds based on the measured optical depth and gain a better understanding of how the term "cloud fraction" is dependant on individual instrument sensitivity measurements of optical depth. In this study, UW-AHSRL data will be used in an attempt to determine cloud fraction using a series of optical depth thresholds, and show that a large difference in cloud fraction is calculated depending on the optical depth threshold used. Although beyond the scope of this thesis, this study can then be used as a validation tool to effectively test the limitations of the MODIS optical depth algorithm for thin cirrus.

1.4 Thesis Overview

Chapter 2 describes in detail the lidar equations and how optical properties are calculated. Various plots produced by the UW-AHSRL website are shown. An explanation of the optical depth threshold algorithm is presented in Chapter 3. Chapter 4 uses this algorithm to illustrate how the cloud fraction is calculated. Error estimates based on both the retrieved lidar optical depth as well as temporal and vertical averaging are shown. Chapter 5 contains results covering one year of lidar data while Chapter 6 includes a summary and ideas for future work. Lastly, Appendix A shows specifications of the AHSRL and Appendix B includes the cloud fractions for each of the twelve months of lidar data, from September 2003 through August 2004.

Chapter 2

LIDAR MEASUREMENTS

2.1 Introduction

Light Detection and Ranging (LIDAR) instruments were first developed in the 1960's to measure stratospheric aerosols and later used to measure the backscatter cross-section, altitude, thickness, cloud phase, and optical depth of cirrus clouds. A lidar operates by sending a short pulse of light into the atmosphere and receives backscattered photons on the receiving telescope. For visible wavelengths of light, scattering occurs for both aerosols and molecules, while absorption is negligible for clouds containing water and ice (Grund 1990); the common definition of aerosols includes cloud droplets and crystals, dust, pollen, etc. Since the speed of light is known, the altitude of the scattering medium can be calculated as a function of time using the simple equation:

$$r = \frac{ct}{2} \qquad \text{Eq. 2.1}$$

where r is the range to the scattering volume, c is the speed of light, and $\frac{t}{2}$ is the total round trip time divided by 2 (considering only the distance to the particle).

This chapter will investigate both the traditional lidar (also called the single channel lidar) and the high spectral resolution lidar (HSRL), and will explain how the profiles of extinction cross-section, aerosol backscatter cross-section, optical depth, depolarization, and backscatter phase function are derived from the returned signal. Starting with the general form of the lidar equation, the molecular and aerosol components can be separated, allowing each of the other parameters to be calculated.

2.2 The Single Channel Lidar Equation

A traditional lidar has a single detector that counts photons backscattered from both molecules and aerosols. The following equation is shown in terms of the number of received photons rather than power received.

$$N(r) = F(r) N_0 \frac{cA}{2r^2}\left(\beta_a(r)\frac{\mathrm{P}_a(\pi,r)}{4\pi} + \beta_m(r)\frac{\mathrm{P}_m(\pi,r)}{4\pi} \right) e^{-2\tau(r)} \qquad \text{Eq. 2.2}$$

where

$N(r)$ = the number of photons incident on the receiver from range r;
$F(r)$ = a geometrical factor, which is dependant on the receiver optics and the transmitter beam divergence;
N_0 = the number of transmitted photons;
c = speed of light, in m/s;
A = area of the receiver telescope, in m^2;
$\beta_a(r), \beta_m(r)$ = aerosol and molecular scattering cross sections per unit volume from range r, in m^{-1};
$\frac{\mathrm{P}_a(\pi,r)}{4\pi}, \frac{\mathrm{P}_m(\pi,r)}{4\pi}$ = aerosol and molecular backscatter phase functions from range r, in sr^{-1};
$\tau(r)$ = optical depth of the layer between ranges r_1 and r_2, and is given by: $\int_{r_2}^{r_1} \beta_e(r)dr$;
$\beta_e(r)$ = total extinction cross section per unit volume at range r, in m^{-1};

If the lidar has multiple receiver fields of view (FOVs), the number of transmitted and received photons as well as the geometrical factor will have FOV dependence. The geometrical factor, $F(r)$, is a correction factor and accounts for the telescope being out of focus at close ranges. This is a dimensionless quantity and is assumed to be unity at heights far above the system. Figure 2.1 shows an example of a single channel lidar return measured on April 4th, 2004. The backscatter shows a thin cirrus cloud with a relatively clear boundary layer.

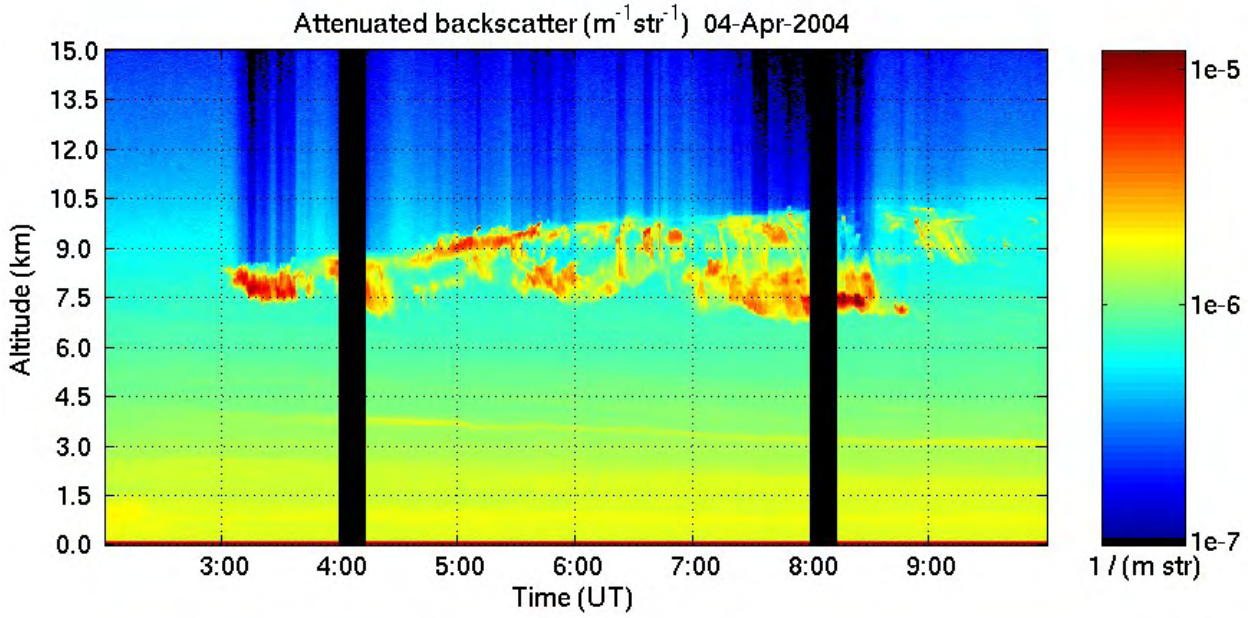

Figure 2.1 – The attenuated backscatter from April 4th, 2004, from 2 to 10 UTC. This image is the result of one quantum detector containing of the backscattered photons of both aerosols and molecules. The black vertical lines at 4 and 8 UTC represent calibration periods. The quality of the signal declines above the cloud due to the reduced number of returned photons.

A single channel lidar has limited capability in retrieving cloud properties as an assumption is required regarding the relationship between the backscatter and extinction cross-sections, $\beta'_a = \beta_a \frac{P_a(\pi)}{4\pi}$ and β_e, respectively. A commonly used inversion method for the single channel lidar is the Klett technique (Klett 1981). The method uses a power law relationship between the extinction and backscatter cross-sections. Hughes (1985) showed that this method cannot be applied to optically thin clouds and can often be unreliable although it is still used with single channel lidar systems. The power law is based on mathematical convenience rather than atmospheric physical properties.

2.3 The High Spectral Resolution Lidar

The shortcoming of the single channel lidar can be overcome by separating the received signal into molecular and aerosol components (Shipley et al. 1983, Grund 1987, and Piironen 1994). The thermal motion of atmospheric molecules causes a Doppler frequency shift in the returned signal, while heavier (and therefore slower moving) aerosols do not cause a noticeable broadening of the received spectrum. The returned signal passes through a polarizing cube, which separates photons that have a different polarization than the transmitted signal (used to determine cloud phase).

The remaining signal then passes through a 50/50 beam splitter, so that half the signal travels to the combined detector (the combined detector is the basis of the single channel lidar), and the other half passes through an iodine absorption cell. Scattering due to molecules can be isolated from the returned signal by using this iodine gas absorption filter to remove aerosol scattering. Comparing the combined channel and the molecular channel allows the lidar to isolate aerosol-scattered photons. By doing this, the need for assumptions in the lidar equation (Eq. 2.2) is removed, and gives a large advantage over the single channel lidar. Figure 2.2 shows a diagram of the HSRL.

Rayleigh scattering theory allows the molecular backscatter phase function to be written as $\frac{P_m(\pi,r)}{4\pi} = \frac{3}{8\pi}$. With this separation, the lidar equation can be divided into two equations:

$$N_a(r) = F(r) N_0 \frac{cA}{2r^2}\left(\beta_a \frac{P_a(\pi,r)}{4\pi}\right) e^{-2\tau(r)} \qquad \text{Eq. 2.3}$$

$$N_m(r) = F(r) N_0 \frac{cA}{2r^2}\left(\beta_m \frac{3}{8\pi}\right) e^{-2\tau(r)} \qquad \text{Eq. 2.4}$$

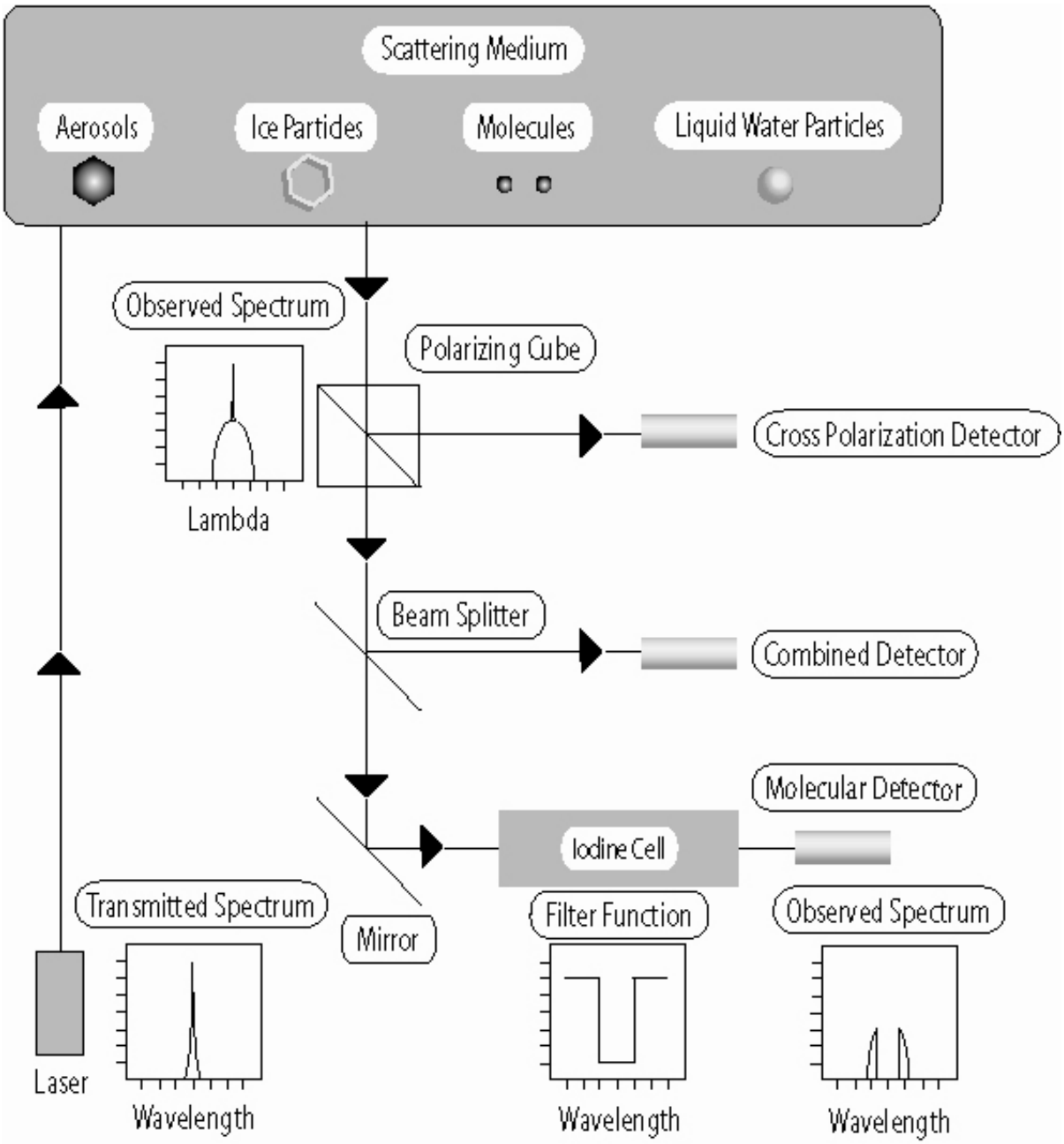

Figure 2.2 – A spectral diagram of the HSRL transmitter and receiver. A narrow laser pulse is transmitted into the atmosphere above the lidar and the backscattered signal is returned into the same telescope (not shown here). The return signal passes through a polarization cube so that the amount of depolarization can be measured (to determine cloud phase). The signal is again split, this time with a 50/50 beam splitter, where half the signal travels to the combined detector and the remainder passes through an iodine absorption cell, removing the aerosol components. By subtracting the molecular channel from the combined channel, the aerosol channel can be isolated.

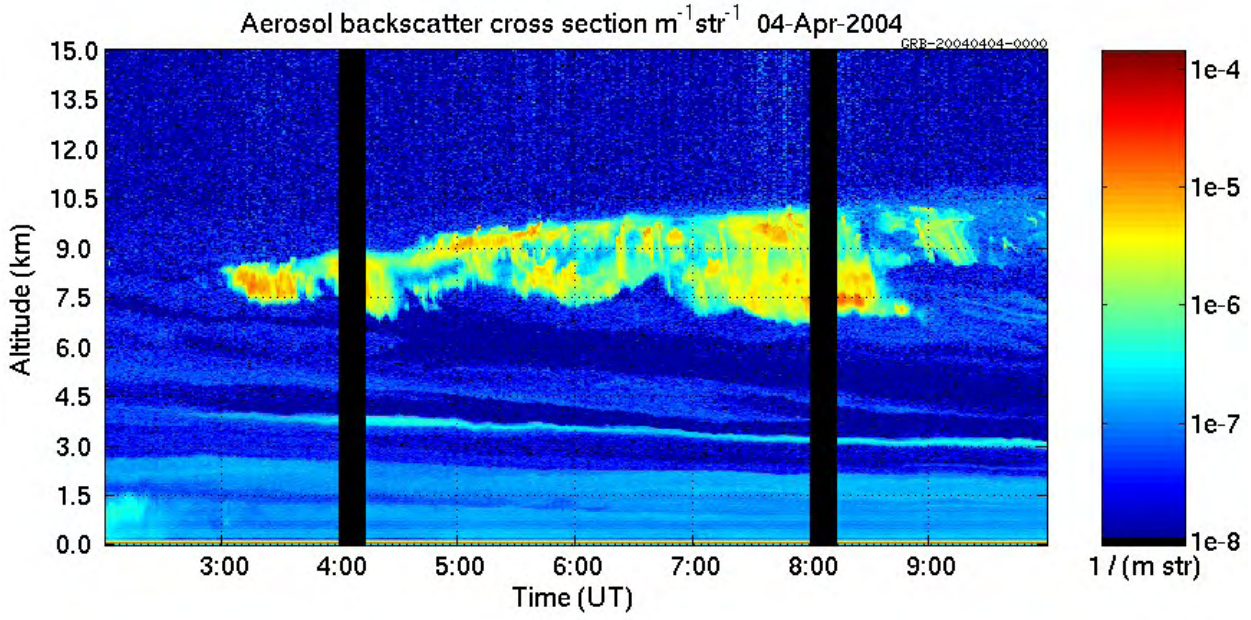

Figure 2.3 – Aerosol backscatter cross section from April 4th, 2004. Compared to Figure 2.1, this image is far more detailed. When the aerosol and molecular signals are separated, the assumptions from the lidar equation are removed and the signal quality improves.

Figure 2.3 shows the aerosol backscatter cross section from April 4th, 2004 from 2 to 10 UTC as seen by an HSRL system. Separating the aerosol and molecular signals allows for an improved returned signal above cloud tops, as shown when compared to Figure 2.1. The aerosol backscatter cross section image shows the clarity of the boundary layer.

With the addition of an atmospheric temperature and pressure profile (commonly available from a nearby radiosonde), the theoretical molecular scattering cross-section can be calculated (also from Rayleigh theory) by using Equation 2.5:

$$\beta_m(r) = C_{air}\frac{P(r)}{T(r)} \qquad \text{Eq. 2.5}$$

where $C_{air} = 3.786\times10^{-6}\left[\frac{K}{hPa^{-1}m^{-1}}\right]$ (used for a wavelength of 532 nm), $P(r) =$ Pressure, and $T(r) =$ Temperature at range r

2.4 Calibration of AHSRL Data

As mentioned previously, the HSRL discriminates between photons backscattered from aerosols and molecules based on the molecular Doppler spectral broadening of the returned signal. In fact, penetration of the clouds, and hence cloud top altitudes, are assured in HSRL data by the presence of molecular backscatter signal from above the cloud (Grund 1990). The iodine cell used to subtract aerosol-scattered photons in the molecular channel is not a perfect absorber, and therefore there is a small amount of leakage of aerosol-backscattered photons.

To account for these imperfections, a calibration scan of the iodine spectrum is preformed intermittently throughout data recording. The laser is tuned across the absorption peak of the iodine filter and both the combined and molecular channels are recorded. The fraction of the actual molecular signal measured in the molecular channel (Cmm) is measured by convoluting both the molecular and combined channels with the broadened molecular spectrum computed from the atmosphere. The rejection efficiency of the iodine cell to aerosol backscattered photons is measured by tuning the laser to the absorption peak of the iodine cell and measuring the number of photons received in the molecular channel relative to the combined channel (Cam). The measured signals are then:

$$S_{a+m}(r) = \eta\left[N_a(r) + C_{ma}N_m(r)\right] \qquad \text{Eq. 2.6}$$

$$S_m(r) = \eta\left[C_{am}N_a + C_{mm}N_m(r)\right] \qquad \text{Eq. 2.7}$$

where

S_{a+m} = signal measured with the combined channel;
S_m = signal measured with molecular channel;
N_a, N_m = total number of aerosol and molecular backscatter photons incident on the receiver field of view;

C_{am} = aerosol transmission of the molecular channel relative to the combined channel;

C_{mm} = molecular transmission of the molecular channel relative to the combined channel;

C_{ma} = molecular transmission of the aerosol channel relative to the combined channel;

η = system efficiency factor that includes the optical transmission of the combined channel and photomultiplier quantum efficiency

The following two equations can be solved to present the separated aerosol and molecular backscatter signals. More details can be found in Piironen (1994) on the calibration sequence and the coefficients.

$$N_m(r) = \frac{S_m(r) - C_{am} S_{a+m}(r)}{\eta\left(C_{mm} - C_{ma} C_{am}\right)} \qquad \text{Eq. 2.8}$$

$$N_a(r) = \frac{C_{mm} S_{a+m}(r) - \eta C_{ma} S_m(r)}{\eta\left(C_{mm} - C_{am} C_{ma}\right)} \qquad \text{Eq. 2.9}$$

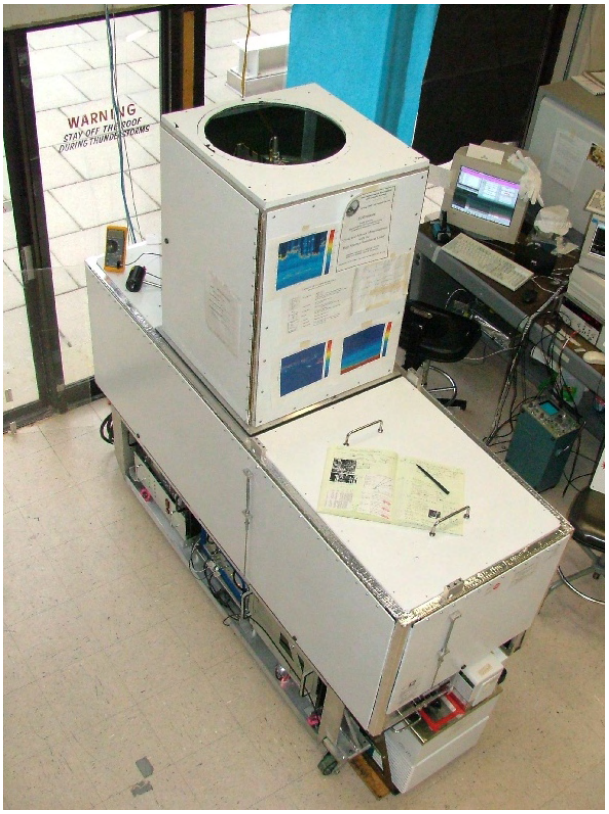

Figure 2.4 – A top view of the AHSRL during operational testing while the system was located in Madison, WI.

Figure 2.5 – The AHSRL with the protective housing removed. The power supply, laser cooling system, and on-board computer can be seen in the lower compartment. The tilted table is meant to reduce specular reflections due to horizontal ice particles sometimes present in clouds. Among other components located on the table is the laser (the black box on the furthest corner of the table), the primary telescope, and the grey detector box (located at the near corner of the table). The system is temperature controlled and is able to run months at a time controlled only through a network connection.

2.5 AHSRL Atmospheric Measurements

The UW-AHSRL has been in nearly constant operation in Madison, WI, since the summer of 2003 (seen with protective housing attached in Figure 2.4). Figure 2.5 shows the AHSRL with the protective housing removed a short time before the system was transferred to a rooftop to begin continuous operation. While previous UW-Madison lidar systems have needed a scientist or graduate student to manually perform calibration measurements for every few hours of data reception, this lidar automatically performs the calibration sequence every few hours (or when deemed necessary).

While calibration scans are performed on a regular basis for the AHSRL, the calibration coefficients used by the system are updated at regular intervals and are applied when data is extracted from the website. Even though the system has been in operation for over a year, many adjustments and experiments to reach optimal performance have been completed. While the accuracy of the calibration coefficients is within acceptable limits for vast majority of the data collected thus far, it should be noted that the quality of the coefficients was checked for the cases mentioned in this thesis, but not for the entire data set involved in the twelve-month study.

The lidar is controlled solely through a network connection and should be capable of running unaided for months at a time. The UW-Madison Lidar website allows one to retrieve data from as far back as June 2003, in either the form of visual images or as netCDF files (see http://lidar.ssec.wisc.edu). This system was transported to Barrow, Alaska, in the fall of 2004 to aid in the Atmospheric Radiation Measurement (ARM) project.

The AHSRL uses the returned signal to calculate of a number of important atmospheric measurements - one of the most useful is the cloud optical depth. The simple optical depth

between ranges r_1 and r_2 can be independently measured using the molecular return and the molecular scattering cross-section:

$$\tau(r_2) - \tau(r_1) = \frac{1}{2}\ln\left(\frac{\beta_m(r_2)r_1^{\,2}}{\beta_m(r_1)r_2^{\,2}}\frac{N_m(r_1)}{N_m(r_2)}\right) \qquad \text{Eq. 2.10}$$

Figure 2.6 shows an optical depth profile from the AHSRL for the case of 2 to 10 UTC on April 4th, 2004 (seen in Figure 2.3). This is a time averaged plot of the eight hour period, as will be each of the following images. At the time this thesis was completed, the lidar data suffered from an overlap correction problem that occurred at low altitudes when the telescope was not in focus. In order to calculate the correct optical depth of a cloud, the difference between the cloud top and bottom is measured, despite the negative side of the X-axis of the plot. In this image, the optical depth near the ground is labeled as below 0 – which, by definition, is impossible. In this case, the average optical depth of the cloud is near 0.1 – (– 0.04) = 0.14.

By combining Equations 2.8 and 2.9, the scattering ratio can be defined as:

$$SR(r) = \frac{N_a(r)}{N_m(r)} \qquad \text{Eq. 2.11}$$

The $SR(r)$ is FOV independent in that the terms containing FOV cancel. Figure 2.7 shows a time average plot of the scattering ratio – a quick check to detect the presence of and thickness of a cloud. While the location of the thin cirrus can easily be seen between 7 and 10 km, there is also a small amount of aerosol backscatter that can be seen between 0 and 5 km. This can be checked by a quick comparison with Figure 2.3.

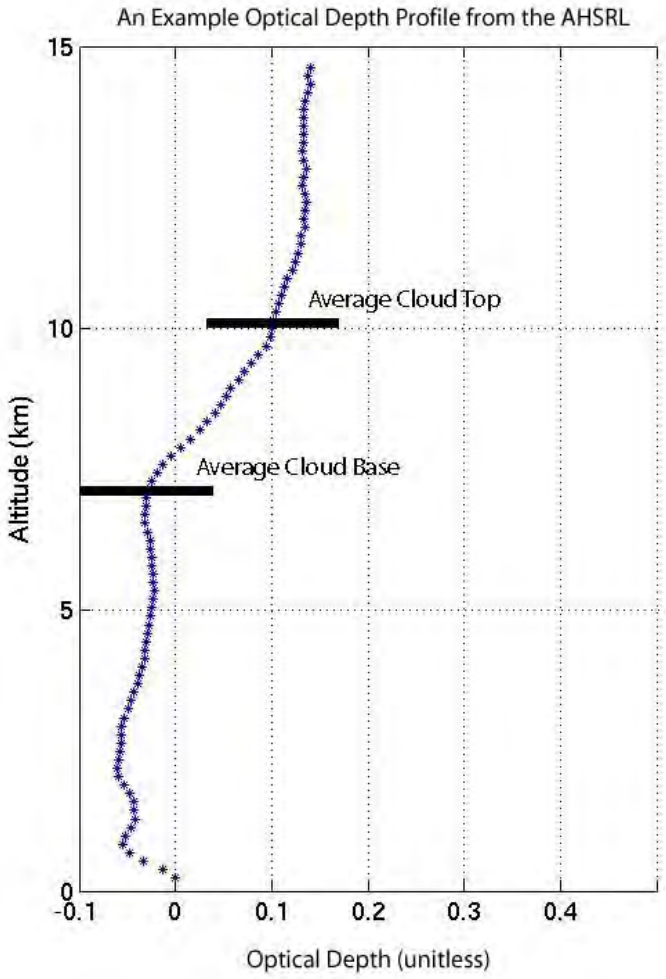

Figure 2.6 – A time averaged plot of the optical depth for the case of April 4th, 2004 (2 to 10 UTC). The optical depth of the cloud is the difference between the cloud top and cloud bottom, despite negative numbers caused by an overlap correction problem when the telescope is out of focus at low altitudes. In this case, the cloud boundaries (as estimated from Figure 2.3) are around 7.5 and 10 km, with an average cloud optical depth of 0.1 – (-0.04) ~ 0.14.

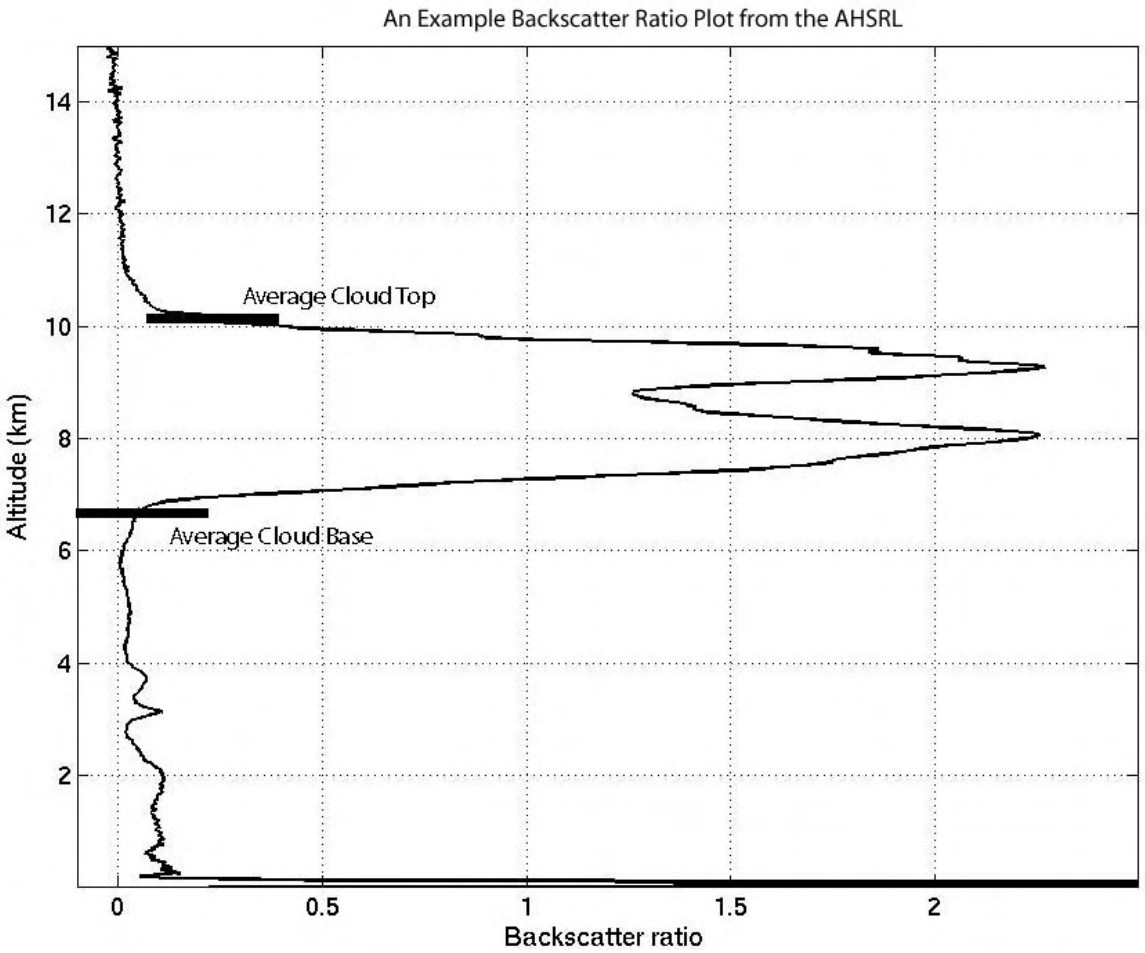

Figure 2.7 – A time averaged plot of the scatter ratio (SR) for the case of April 4th, 2004 (2 to 10 UTC). The cloud boundaries are clearly visible near 7 and 10 km. A small amount of backscatter can be seen below 5 km, due to the boundary layer. Above the cloud (higher than 12 km), the scattering ratio approaches 0, indicating no clouds were present at that height on this day.

The aerosol backscatter cross-section and aerosol extinction profiles can be defined as:

$$\beta'_a(r) = \beta_a(r)\frac{P(\pi,r)}{4\pi} = SR(r)\beta_m(r)\frac{3}{8\pi} \qquad \text{Eq. 2.12}$$

$$\langle \beta_e(r_1,r_2)\rangle = \left\langle \frac{\partial \tau}{\partial r} \right\rangle = \frac{\tau(r_2)-\tau(r_1)}{r_2-r_1} \qquad \text{Eq. 2.13}$$

where $\langle \beta_e(r_1,r_2)\rangle$ is the average value of total extinction cross section and is a range derivative of the optical depth.

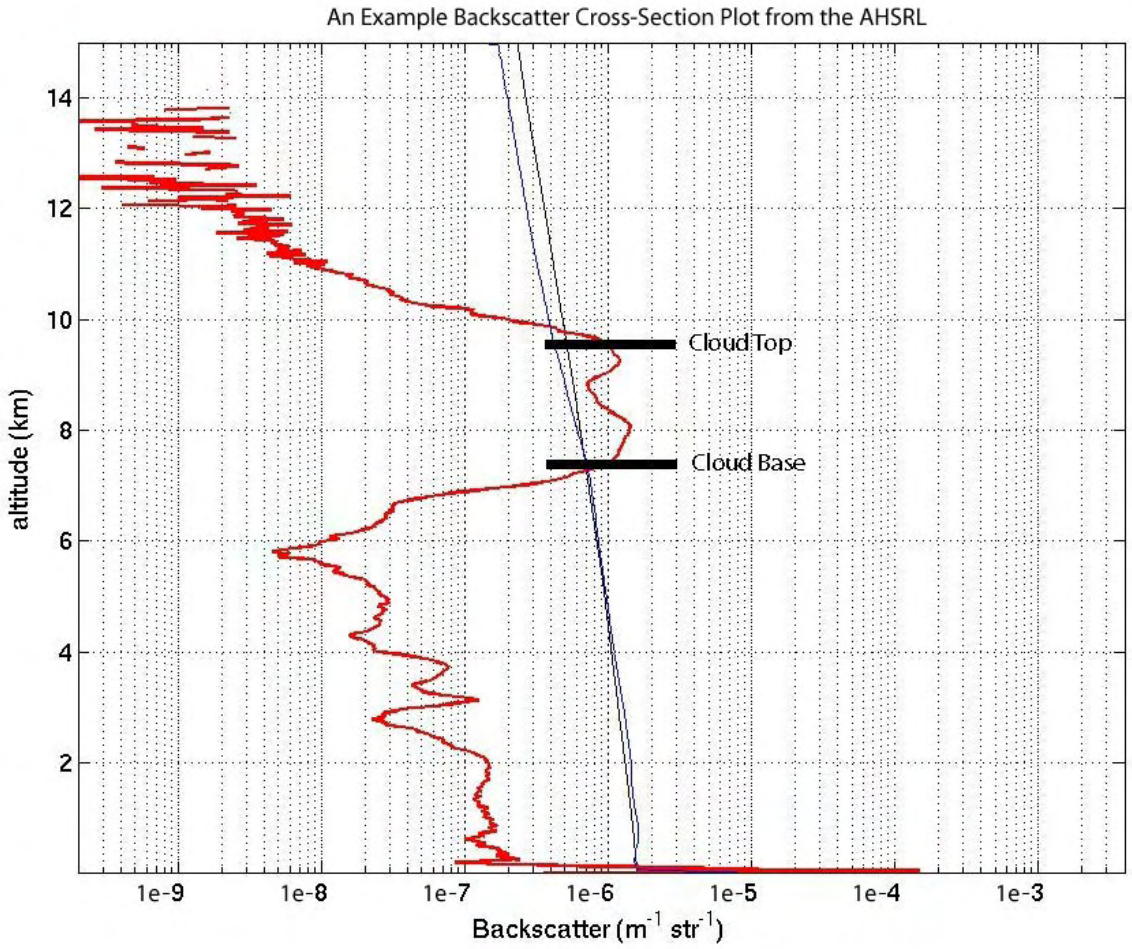

Figure 2.8 – Aerosol backscatter (red) theoretical molecular (black) and actual molecular (blue) returns. The cloud top and base are labeled as defined by a threshold of 1e-6 (m str)$^{-1}$. Plots of this type show a large variation depending on the altitude and thickness of clouds.

Figure 2.8 shows the time-averaged aerosol and molecular cross sections for the case of April 4th, 2004. The black line represents the theoretical molecular channel, as determined from the pressure and temperature profile. The blue line is the actual molecular profile, which was computed by removing the aerosol-scattered photons using the iodine cell. Finally, the red line shows aerosol-scattered photons. The peak in the aerosol channel near the ground is most likely caused by internal reflections in the lidar and from the penthouse window. Within the first few kilometers, the detectors receiver photons scattered from boundary layer haze and dust. The

cloud top and base in the figure are determined by locating the altitude where the aerosol backscatter crosses a threshold of 1e-6 (m str)$^{-1}$. The justification for this threshold will be explained in Section 3.2.

Although the probability function of the backscatter phase function is peaked at $\frac{P_a(\pi)}{4\pi} = 0.04$, Holz (2002) showed that the results vary between the ranges of 0.14 and 0.005 and shows a large dependence on depolarization. The peak of the distribution is consistent with bullet rosettes, spheres, and solid columns – typical of the ice particle shapes found in cirrus clouds. This information is important for a single channel lidar that require estimates of the backscatter phase function to make a measurement of the cloud optical depth.

The optical depth profile may also be calculated from $\frac{P_a(\pi)}{4\pi}$ by the following equation when the correction value of the backscatter phase function is used. This can only be done when multiple scattering contributions from the cloud are small. Kuehn (2001) has more detail on multiple scattering contributions and corrections.

$$\tau(r_2) - \tau(r_1) = \int_{r_1}^{r_2} \frac{\beta'_a(r)}{\left\langle \frac{P_a(\pi)}{4\pi} \right\rangle} dr \qquad \text{Eq. 2.14}$$

Through the use of a quarterwave plate, the signal is transmitted as a circularly polarized wave into the atmosphere. As Sassen (2001 Part II) stated it perfectly, "whereas spherical particles do not cause depolarization during single backscattering, the internal skew ray paths through arbitrarily shaped crystals of ice normally produce copious amounts of backscatter depolarization using visible and near-infrared lasers." On the return trip to the detectors, both

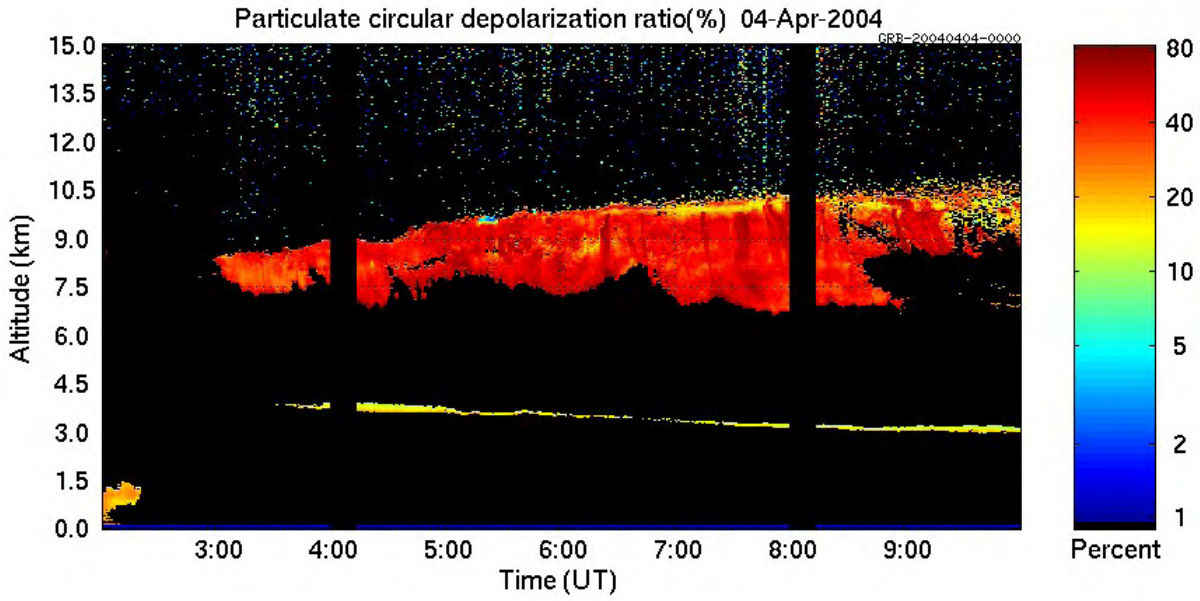

Figure 2.9 – Circular depolarization ratio for the given time period of April 4th, 2004 from 2-10 UTC. This figure shows that this particular cloud has a depolarization of over 25%, indicating ice.

the originally polarized (from spherical water particles) and the polarization shifted waves (reflected from ice particles) once again pass through the quarterwave plate. Any alteration in the polarization of the return signal is transformed into a linearly polarized wave of different orientation than the original (perpendicular to the original), and the use of a beam splitter in the detector box allows the cross polarization channel to measure this shift. Depolarization is defined as the number of received photons with the same circular polarization as the transmitted beam divided by the number of received photons with the opposite circular polarization.

$$\delta = \frac{N_{a(\text{received photons with polarization same as transmitted polarization})}}{N_{a(\text{received photons with polarization opposite transmitted polarization})}} \qquad \text{Eq. 2.15}$$

Circularly depolarization values higher than 25% indicate ice, and the depolarization ratio will increase as multiple scattering increases. Lidar systems with larger FOVs may not be able to

discriminate between ice and water clouds as well as a system with a smaller FOV. The depolarization of most of the cloud in Figure 2.9 is over 25%, indicating an ice composition typical of cirrus clouds.

Systems are regularly built so that the transmitted beam is a few degrees off nadir. Research conducted by Liou (1986) and Sassen (2001 Part II) shows that "the light specularly reflected off a properly oriented crystal face will produce very strong, but nondepolarized backscattering." If the lidar was not tilted a few degrees, false cloud phase readings may occur due to these reflections, and clouds might be identified as composed of water instead of ice.

Dr. Eloranta devised a simple cloud classification system given in Figure 2.10 through logic as well as experimentation in order to easily identify cloud phases. This is merely a rough guideline to determine cloud phases, and is by no means 100% exact. By using the depolarization as well as the backscatter cross section, water haze and dust can be distinguished from water and ice. Figure 2.11 shows the cloud used in this case study to be an ice composition surrounded by a thin layer of haze, as speculated by looking at Figure 2.9. The following chapter will utilize this cloud classification scheme and will illustrate how optical depth and backscatter thresholds are used to define cloud boundaries.

3.1 Assessment of Photon Counting and Calibration Errors

The measured molecular signal provides a known target at each altitude from which the aerosol backscatter cross-section can be calculated. This method of separation removes the earlier mentioned assumptions of the single channel system and leaves errors caused by multiply scattered photons, photon counting statistics, and calibration errors.

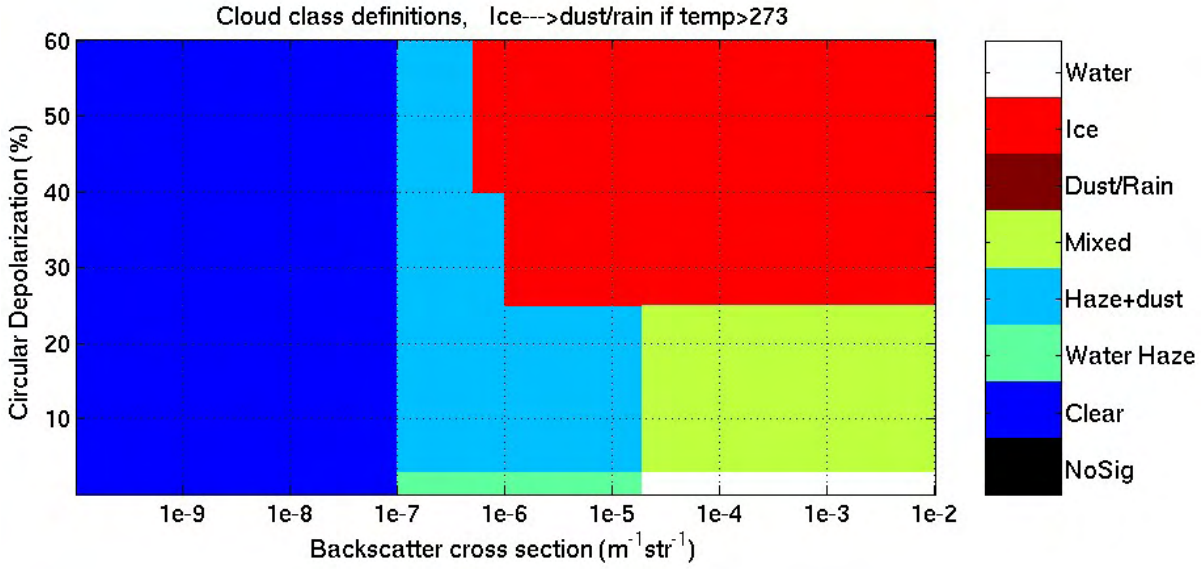

Figure 2.10 – Cloud phase definitions based on the backscatter scatter cross section and the circular depolarization developed by Dr. Eloranta. Depolarization of more than 25% indicates ice clouds while depolarization values of less than 3% indicate water. In between these values, the cloud composition is assumed to be mixed phase. This scheme is useful in creating plots such as Figure 2.11

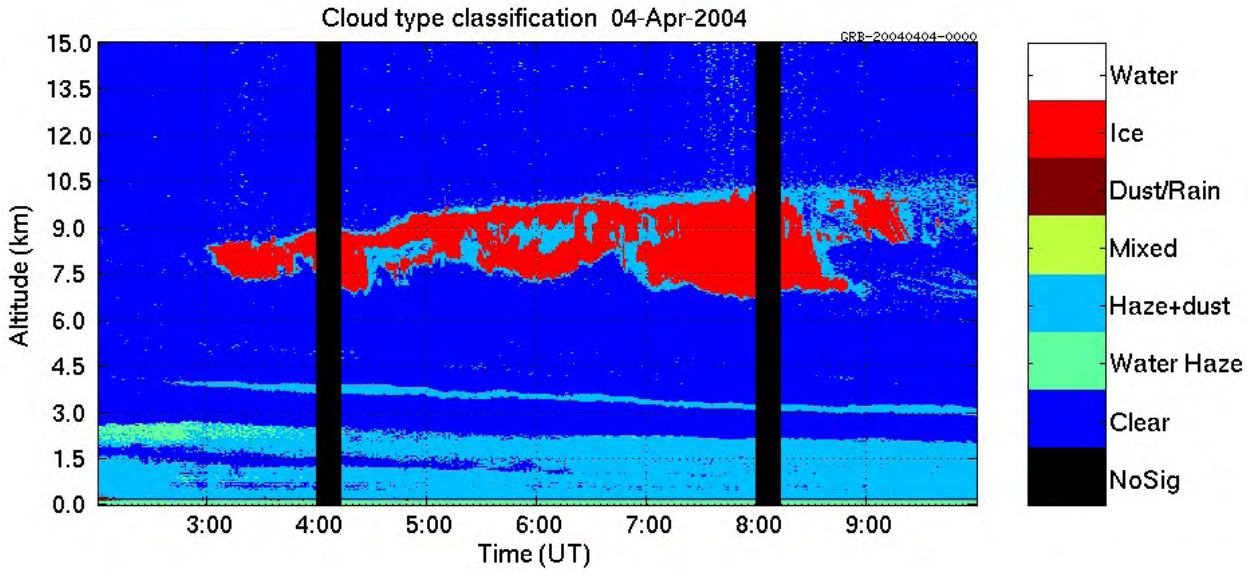

Figure 2.11 – Based on the depolarization and backscatter cross section of Figure 2.9, this cloud is classified as ice with the boundary layer consisting of mostly haze and dust.

2..1 Description of Multiple Scattering

The received lidar signal contains both single photons and those that have been scattered multiple times. Eloranta (1967) conducted some of the earliest research regarding multiple scattering, and provided the mathematical framework for modeling the double scattered lidar return as well as compared model output to lidar measurements of hazes and fogs. Research since then has shown that multiple scattering is a function of the receiver FOV, transmitter divergence, cloud optical depth, effective particle size, and scattering phase function in the backscatter direction (Bissonnette 1996, Eloranta 1998). Several investigators have conducted research involving multiply scattered measurements, and have shown the ability to determine the effective particle size and particle distribution of clouds (Allen and Platt 1977, Kuehn 2001).

Although important for large fields of view, the multiple scattering contributions cause small errors in the AHSRL measurements due to the 45 μrad field of view. The single scatter lidar equation assumes that when a photon is scattered it is removed from the beam. In reality, up to half the total scattered energy is forward scattered, some of which remains in the receiver field of view and contributes to the lidar signal. Multiple scattering has the largest impact when there is a large change in the extinction cross-section, such as cloud boundaries.

Multiple scattering processes can adversely affect the divergence of optical beams propagating through these clouds (Grund 1990). Platt (1973) showed that a visible optical thickness can be obtained directly from the lidar data but its value is lower than the true value due to near-forward, multiple-scattered radiation being detected by the laser receiver. The literature on the correction of multiply scattered photons is extensive, and more information can be found in Eloranta (1967, 1998), Allen (1977), Bissonnette (1996), and Léon (2003).

2..2 Photon Counting and Calibration Errors

The AHSRL collects photons scattered from both molecules and aerosols, and as such, the photon counting errors are given by a Poisson distribution based on the following formula:

$$\sigma = \sqrt{N} \qquad \text{Eq. 2.16}$$

where N = number of photons counts

Based on the propagation of these statistical errors in the raw data through the lidar equation, errors can result in the measured optical properties, such as optical depth and depolarization. Piironon (1994) and Holz (2002) show that the error associated with optical depth can be approximated as the sum of the errors in the molecular return and the molecular scattering cross-section. Equation 2.17 shows this dependence (where $\Delta\beta_m(R)$ and ΔN_m represent the errors in the molecular scattering cross-section and molecular return, respectively).

$$(\Delta\tau(R))^2 \approx 2\left(\frac{\partial\tau(R)}{\partial\beta_m(R)}\right)^2(\Delta\beta_m(R))^2 + 2\left(\frac{\partial\tau(R)}{\partial N_m(R)}\right)^2(\Delta N_m)^2 \qquad \text{Eq. 2.17}$$

The error associated with the molecular scattering cross-section is related to the uncertainties in the radiosonde profile - specifically the pressure and temperature. Currently, the profiles are taken from radiosondes from Green Bay, Wisconsin. The primary discrepancies are caused by the geographic and temporal separation (Green Bay is approximately 150 km north of Madison). The AHSRL attempts to collect the radiosonde data every twelve hours, and therefore the time differences can often be large between the profile and the data collection. Radiosondes will be launched routinely on location when the system is moved the Barrow, Alaska.

While the error in the density profile is assumed to be random, a study performed by Holz (2002) has shown that the optical depth is particularly sensitive to the errors in the lapse rate of the temperature profile. The optical depth error is sensitive to the error in the temperature difference between the top and base of the cloud. This uncertainty affects the error in the calibration coefficient Cmm, and with a three-minute time average, cloud optical depths can be detected with a suitable accuracy. While errors below the cloud base are mostly produced by the uncertainties in the radiosonde profile, once the signal enters a cloud, the errors are almost entirely due to the inaccuracy of measuring the molecular scattering cross-section.

Figure 2.12 shows a typical optical depth profile from April 20th, 2004, at 10 UTC which includes the error bars related to both the molecular counts and the molecular scattering cross-section. As seen, the errors below the cloud base are small (due to the density profile) and once the signal encounters the cloud, the errors begin to grow as the returned molecular signal begins to decrease. In this example, the cloud optical depth is approximately 0.75 ± 0.06, or an estimated error of 8%.

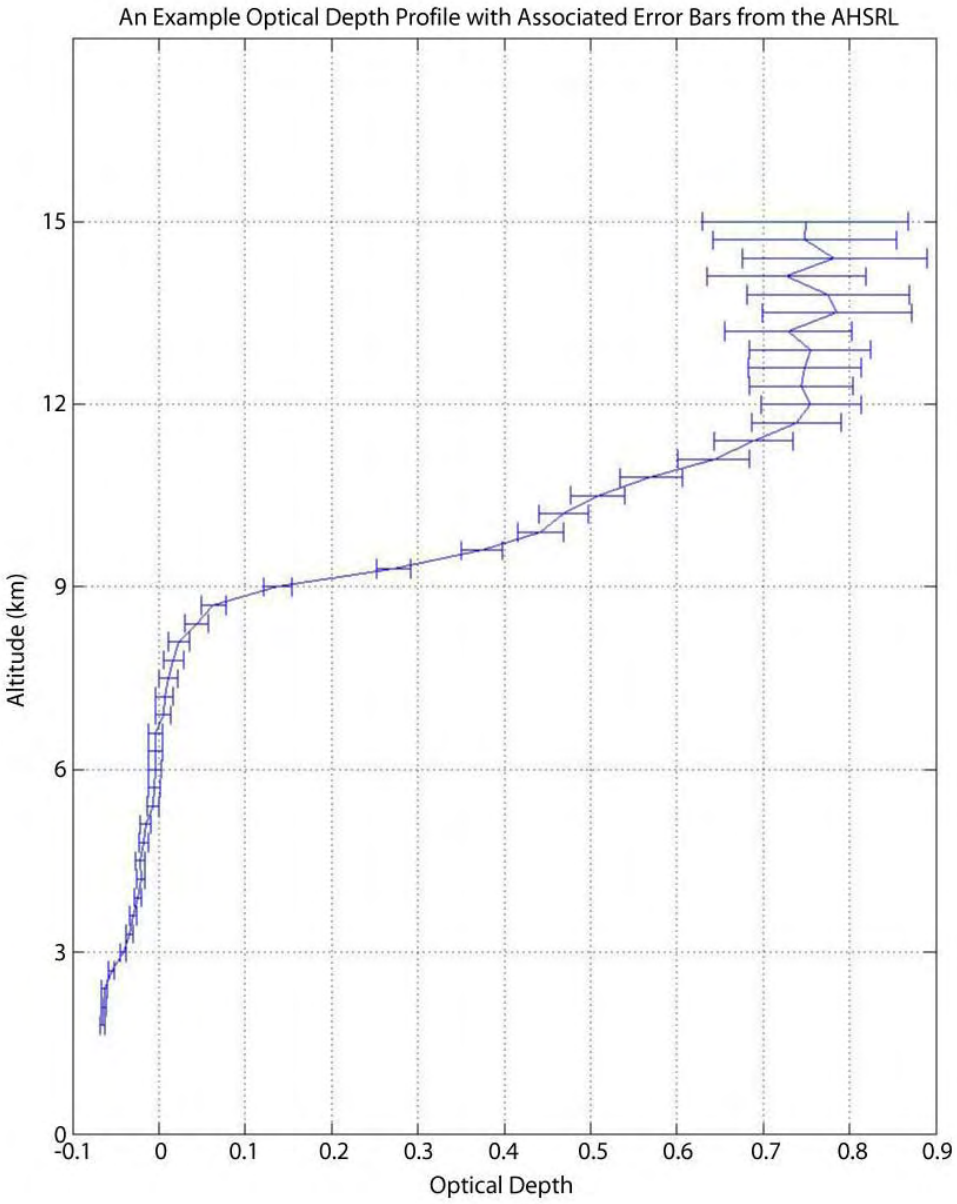

Figure 2.12 – A sample optical depth profile from April 20th, 2004, at 10 UTC. The error bars are estimated from Equation 2.17. Below the cloud base, the errors are due to uncertainties in the density and temperature profile. The error due to temperature is only sensitive to the error in the temperature difference between the cloud base and cloud top. Once the signal penetrates the cloud base, however, the errors are almost entirely due to uncertainties in the molecular return. In this particular case, the optical depth is approximately 0.75, with an uncertainty of ± 0.06, leaving an error of ~ 8%.

Chapter 3

DEFINING CLOUDS BASED ON OPTICAL DEPTH THRESHOLDS

3.1 Introduction

Although satellite retrievals of global cloud cover are invaluable to scientists, calculations of the optical depth and height of thin cirrus clouds lack the accuracy necessary for a complete understanding of the full climactic radiative effect of the cloud. In fact, Wylie and Menzel (1989) estimated that 50% of cirrus clouds with infrared optical depth of 0.1 (τ visible ~ 0.2) were not detected in their satellite data analysis using CO_2 slicing. While these calculations were performed fifteen years ago, their concerns about the ability to detect thin cirrus are still present in recent work (Frey et al 1999, Sassen et al 2000 Part I, Plantnik et al 2003). The overall aim of these studies is to acquire more data for use in the radiative transfer equation.

Many studies have performed research on cirrus cloud cover using optical depth as a guideline, both from the ground and from space. For example, using 860 hours of lidar data between 1992 and 1999, Sassen found that the mean and median optical depth values for the cirrus sample were 0.75 $\pm$ 0.91 and 0.61 (Sassen 2001 Part III). In this same paper, Sassen calculated that the derived values of τ range from 0.003 to 3.0, with around 30% of cirrus having an optical depth of less than 0.3. As a simple classification system, he categorized opaque cloud as those with $\tau > 6$, clouds with an optical depth less than 1.4 as thin clouds, and that subvisible cirrus have $\tau \leq 0.03$.

It is important for scientists to learn the optical depth detection limit of an instrument in order to discover the amount of thin cirrus the instrument may be overlooking. Wylie (1998)

wrote that the threshold for cloud detection of the HIRS appears to be τ VIS > 0.1. Sassen (2000 part I) writes that the MODIS instrument should be able to detect clouds with a lower optical depth limit of 0.3. The UW-AHSRL has made optical depth measurements of as high as 5 using an integration time of three minutes for low altitude clouds, and as low as 0.05 when thin clouds remain overhead for long periods of time. Clouds optically thinner than this are removed from the dataset due to large errors associated with lapse rate uncertainties and molecular counting statistics.

Besides having different optical depths limits, satellites and lidar return also differ in their resolution and fields of view. The MODIS instrument has a 1 km vertical spatial resolution and depending on the spectral channel being used, either a 250 m, 500 m, or 1 km horizontal resolution. The vertical resolution of the UW-AHSRL is 7.5 meters and the FOV is 45 μrad – therefore the lidar detects only what passes directly over the system. While satellites are capable of detecting clouds at various levels in the atmosphere (assuming the satellite can see through the upper level clouds), opaque lower clouds attenuate the lidar signal, making it impossible to detect high and mid-altitude clouds.

If a cloud was viewed from both the lidar and a satellite simultaneously, differences may result between the retrieved cloud height and optical depth due to variances in temporal and spatial resolution and averaging (Stone 1990). While the lidar is capable of finding the very top of the uppermost layer of thin cirrus, the IR radiances detected by satellite emanate mostly from some level beneath the top of the cloud, depending on the emissive characteristics of the cloud (Frey 1999). Minnis (1990) deducted that there are also random errors due to variations in microphysics, morphology, and cloud depth for a given hour, and although the magnitude of these errors are currently (and may always be) unknown, they are potentially large.

3.2 Cloud Boundaries Based on Aerosol Backscatter Thresholds

The data contained in this thesis was taken from the UW-AHSRL website as a netCDF file and stored in a PostgreSQL database for convenience. Through the website, the data was averaged at 3 minutes with a vertical average of 300 meters; that is, 3 minutes and 300 meters of data were averaged into one data point. These particular values were chosen as a compromise between the MODIS and the AHSRL vertical spatial and temporal resolution discussed above, and allowed detailed plots to be created without excessive computational time. While this algorithm was created specifically for these averages, any new averaging limits can be chosen and can be easily added to the database for a future study. A comparison between using different spatial and temporal averages will be discussed later in this thesis.

In order for an algorithm to calculate cloud fraction, the "definition" of a cloud must first be determined. By using the cloud classification scheme developed by Dr. Eloranta (Figure 2.10), an aerosol backscatter cross section value of 1e-6 $(m\ str)^{-1}$ was used in the first case study to determine the cloud base and top for each time profile. By choosing this value, the amount of false cloud base detection by dust and haze in the boundary layer can be minimized. While this value was used in this test case, other values were explored and will be evaluated later this in this chapter.

Figure 3.1 shows the first test case - April 24th, 2004. The aerosol backscatter cross-section and the depolarization are shown in different panels. As seen, a single layer high altitude cloud is present between 9 and 19 UTC that begins with an average height of around 10.5 km. Optically thicker clouds move into the area between 19 and 2355 UTC. High values of the back-

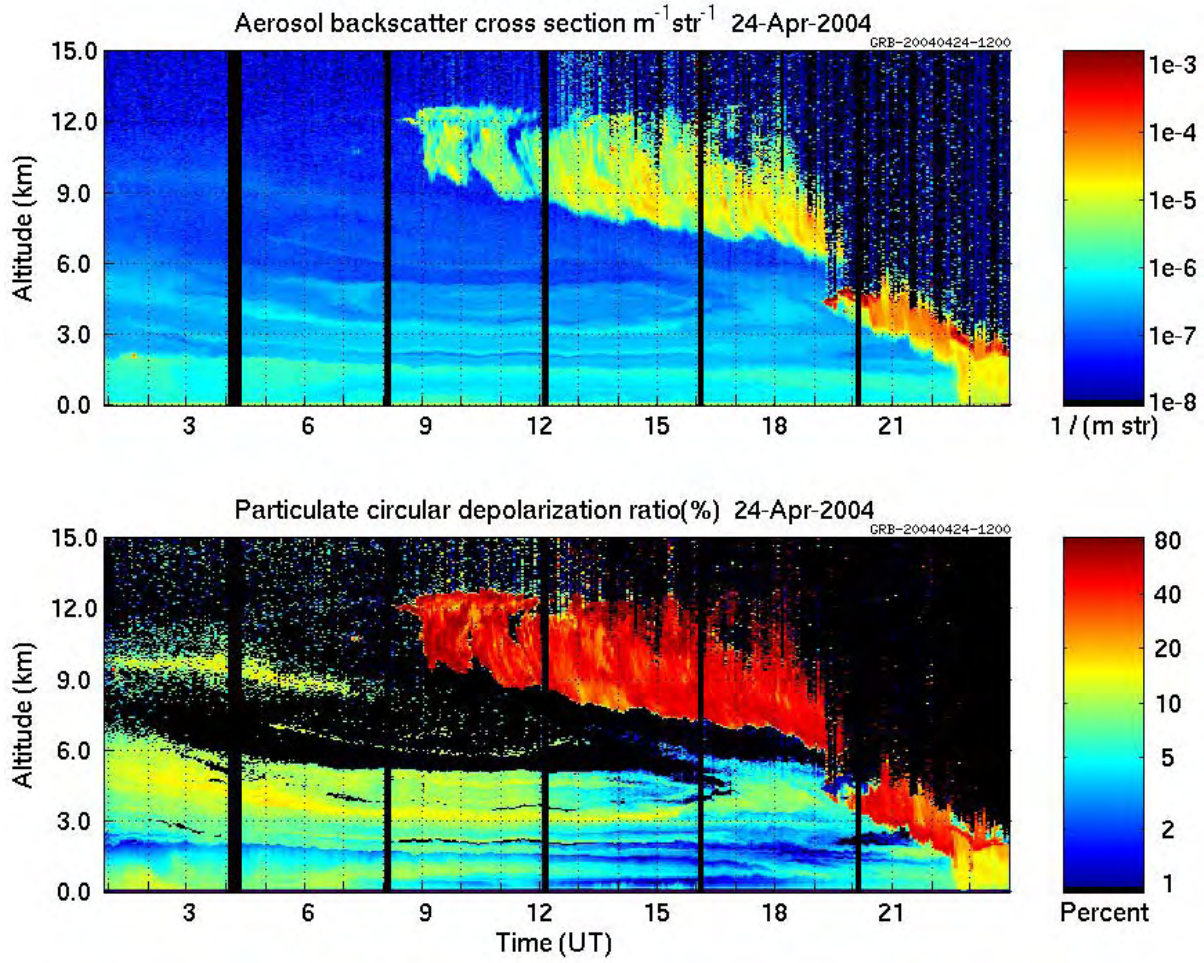

Figure 3.1 – The aerosol backscatter and depolarization plots from April 24th, 2004. This day was one of the case studies in which the algorithm was developed and tested, due to the occurrence of high thin clouds (9-19 UTC) and opaque lower clouds with precipitation (22-23 UTC). Late in the day (19-2355 UTC) the cloud top could not be determined due to the optically thick clouds. The depolarization in the lower panel indicated the occurrence of ice (high depolarization) and water clouds (low depolarization).

scatter cross section indicate where water clouds are present (end of the day), while low values indicate clear sky (between 0 and 9 UTC).

The lower panel of Figure 3.1 shows the depolarization of the test case. The cloud contains mostly ice though 19 UTC (as indicated in red) while water clouds and precipitation can be seen between 19 and 2355 UTC (indicated as the dark blue regions and the regions falling to the ground, respectively). Clear sky and areas above cloud tops that the lidar signal cannot penetrate are indicated in the plot by the black regions. This particular case study was chosen to test the cloud fraction algorithm due to the presence of clear sky, thin cirrus, and opaque clouds.

Figure 3.2 shows the aerosol backscatter cross-section of a single time profile at approximately 1042 UTC. The algorithm determines the cloud base and the cloud top when the backscatter cross section passes a given threshold – in this case, the threshold is 1e-6 $(m\ str)^{-1}$ is used. The cloud base and top heights are identified in the figure where the cloud passes this threshold.

It is important at this time to discuss the presence of multilayer clouds, and how the algorithm deals with such cases. In the example shown in this chapter, thin cirrus are present until 19 UTC, when thicker water clouds move into the lidar field of view. It is uncertain from these images if the high cirrus remains or disappears when the low clouds move into the area. Since most low altitude clouds have an optical depth greater than 2, the signal cannot penetrate these clouds in order to detect multilayer clouds. In cases such as this, the algorithm calculates the total cloud optical depth for that time profile to be the maximum value of 2 (identified as "opaque clouds" in the remainder of this thesis).

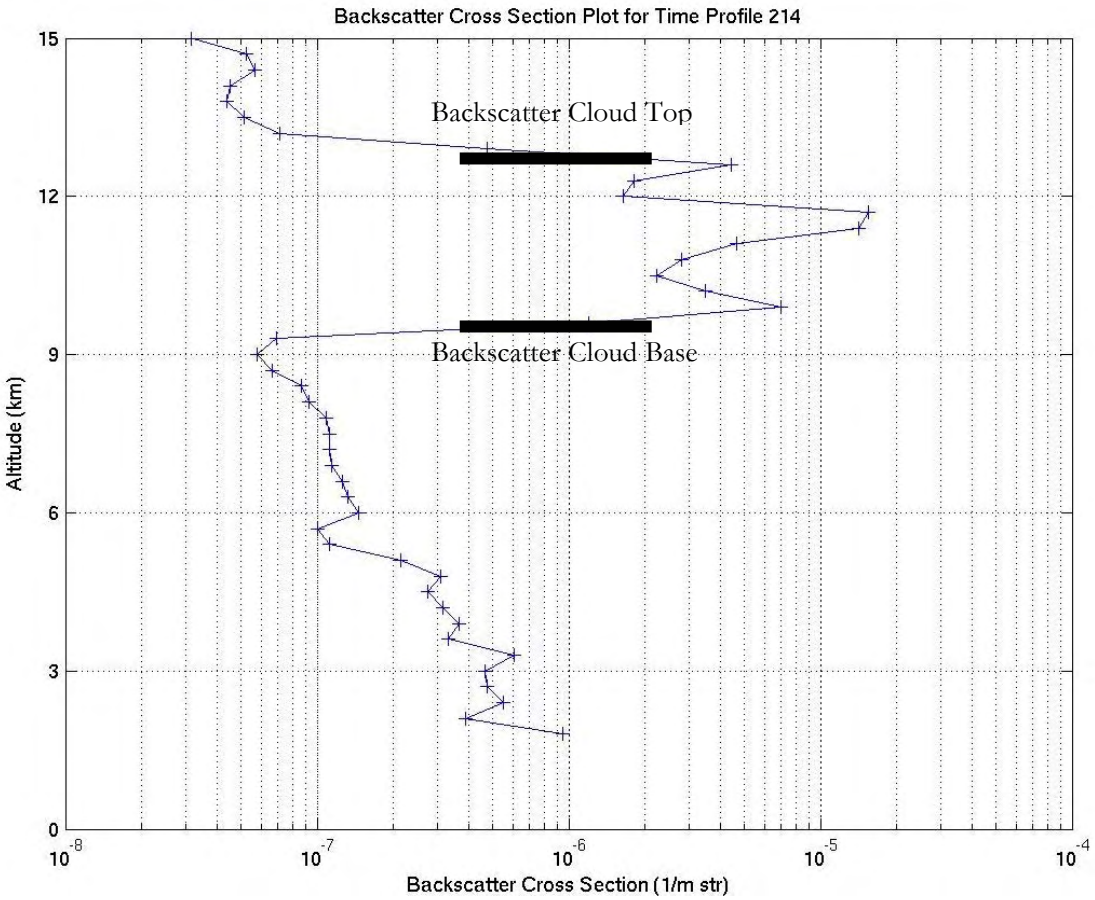

Figure 3.2 – An example of the aerosol backscatter cross-section for a single time bin at 1042 UTC (three minute averaged). The vertical data points are set to a 300-meter average. The threshold algorithm determines the cloud base and height to be the data points when the aerosol backscatter cross section reaches 1e-6 (m str)$^{-1}$. The backscatter cloud base and top heights are identified above. This threshold was chosen to limit the amount of boundary layer dust and haze detected. The lower two kilometers of data are removed for the same reason.

While rare, the lidar signal can occasionally pass through the lower cloud of a multilayer system and accurately measure of the height of the top cloud. If a given backscatter cross section profile such as Figure 3.2 crosses this threshold multiple times (this figure obviously does not), the algorithm calculates the cloud base and top to be that of the lower cloud and upper cloud, respectively. This is done because this study focuses on the total optical depth of each time profile, and multilayer clouds are not of interest.

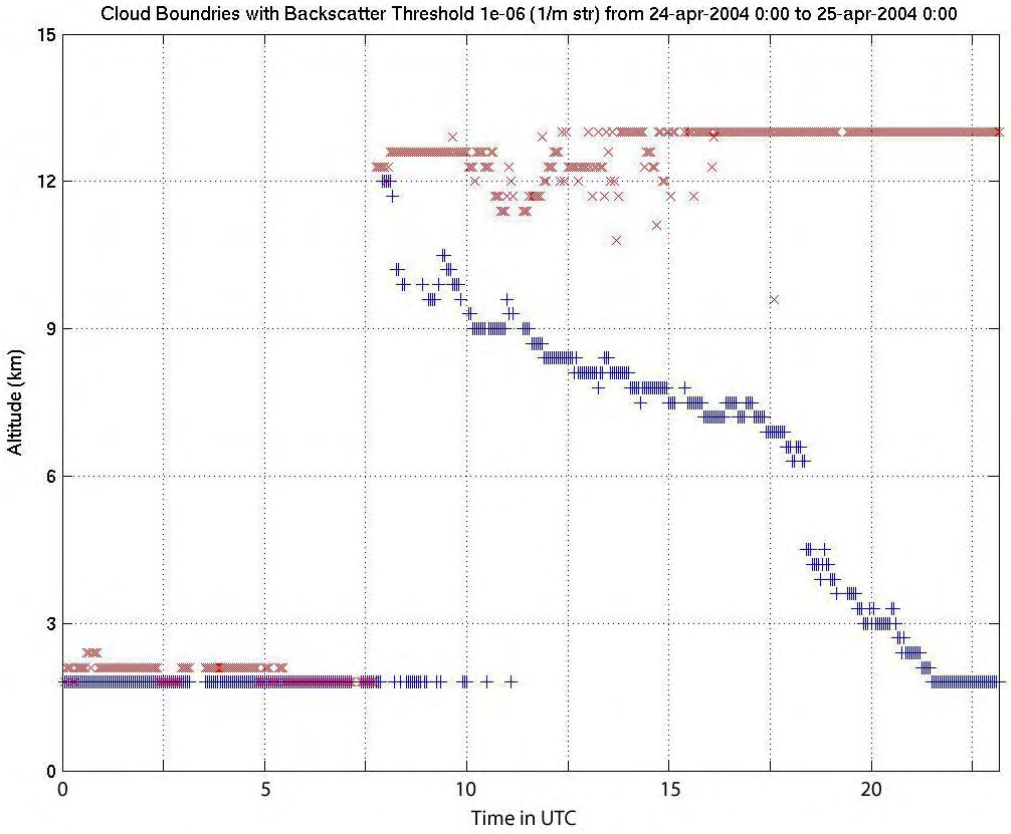

Figure 3.3 – Cloud boundaries based on the aerosol backscatter cross section of 1e-6 (m str)$^{-1}$ from the case study of April 24th, 2004. The blue plus signs represent cloud bases while the red x's show the upper boundary. The algorithm implemented removes calibration periods so that missing data is not confused with other cases. From 0 through 7 UTC, there is a thin cloud area that crosses the backscatter threshold, although future plots show the low optical depth. The lower two kilometers of data were removed to reduce false cloud base detection due to boundary layer haze and dust. A cloud top altitude of 13 km indicates the molecular signal was attenuated substantially, and the maximum optical depth was reached. This can be seen after 13 UTC.

Applying this condition to each time profile in the April 24th case, Figure 3.3 was created showing the determined cloud top and base for the entire day. Calibration periods, missing data, and the lower 2 km of the atmosphere of data are removed to avoid false detection in the boundary layer. Therefore, data points located at altitude '0 km' indicate that no clouds were present above 2 km that passed this backscatter threshold (none are present in this figure). If the backscatter threshold was crossed at the first data point (2 km) as in the cases between 0-7 and

22-24 UTC, the cloud base was set at the lower threshold. Occasionally, the cloud base and the cloud top are determined to be the same data point – the only data point to pass the backscatter threshold. This can be seen between 6 and 8 UTC. When the cloud top was not detected as in the case of a thick cloud (19 through 24 UTC), the cloud top is identified at 13 km in the figure, to show that the maximum optical depth of 2 was reached. In developing the algorithm in this manner, all non-opaque clouds under the lower height limit are not included in this study. Thus, any optical depth due to boundary layer haze was excluded from the individual time profiles.

In order to determine an appropriate value for the lower backscatter threshold, a sensitivity study was performed to compare how various thresholds detected cloud boundaries. This study was done over the hours of 8-12 UTC in the case study date of April 24th, 2004. Figure 3.4A shows the cloud boundaries as determined by changing the backscatter threshold from 1e-5 to 7e-7 (m str)$^{-1}$ with increments of 0.1e-6 (m str)$^{-1}$. Areas in blue represent the lower thresholds while areas in red are parts of the cloud where the backscatter cross-section is equal to or greater than 1e-5 (m str)$^{-1}$. As seen in the picture, aerosols in the boundary layer trigger this lower threshold (meaning they have backscatter cross-sections of around 7e-7 (m str)$^{-1}$. This implies that the threshold is too low.

Figures 3.4B and 3.4C show the same image but with lower backscatter cross-section thresholds of 8e-7 and 9e-7 (m str)$^{-1}$, respectively. As expected, the boundary layer causes fewer false cloud base readings due to the higher thresholds, and the actual cloud base becomes more apparent. The backscatter cross-section threshold color scale in Figure 3.4D varies from 1e-5 to 1e-6 (m str)$^{-1}$, and shows the cloud with no false base detection. It is this reason that in the rest of the study, a value of 1e-6 (m str)$^{-1}$ was chosen as the lower aerosol backscatter cross section threshold.

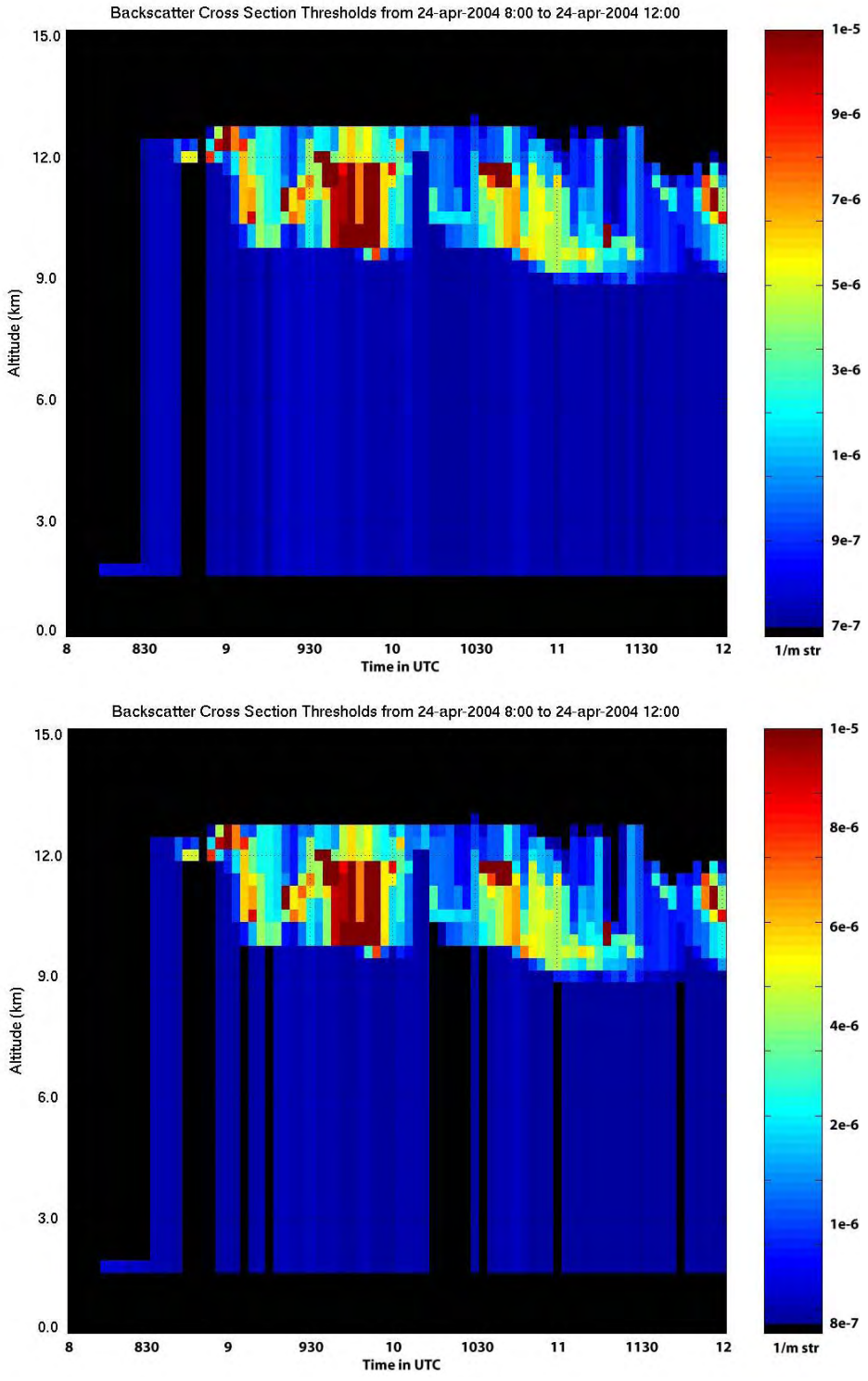

Figures 3.4 (A-B) – Cloud boundaries based on a series of aerosol backscatter cross section thresholds of the cloud from April 24th, 2004. The thresholds range from 7e-7 to 1e-5 and 8e-7 to 1e-5 (m str)$^{-1}$, respectively. As mentioned in the text, the lower the threshold, the more boundary layer haze the algorithm detects.

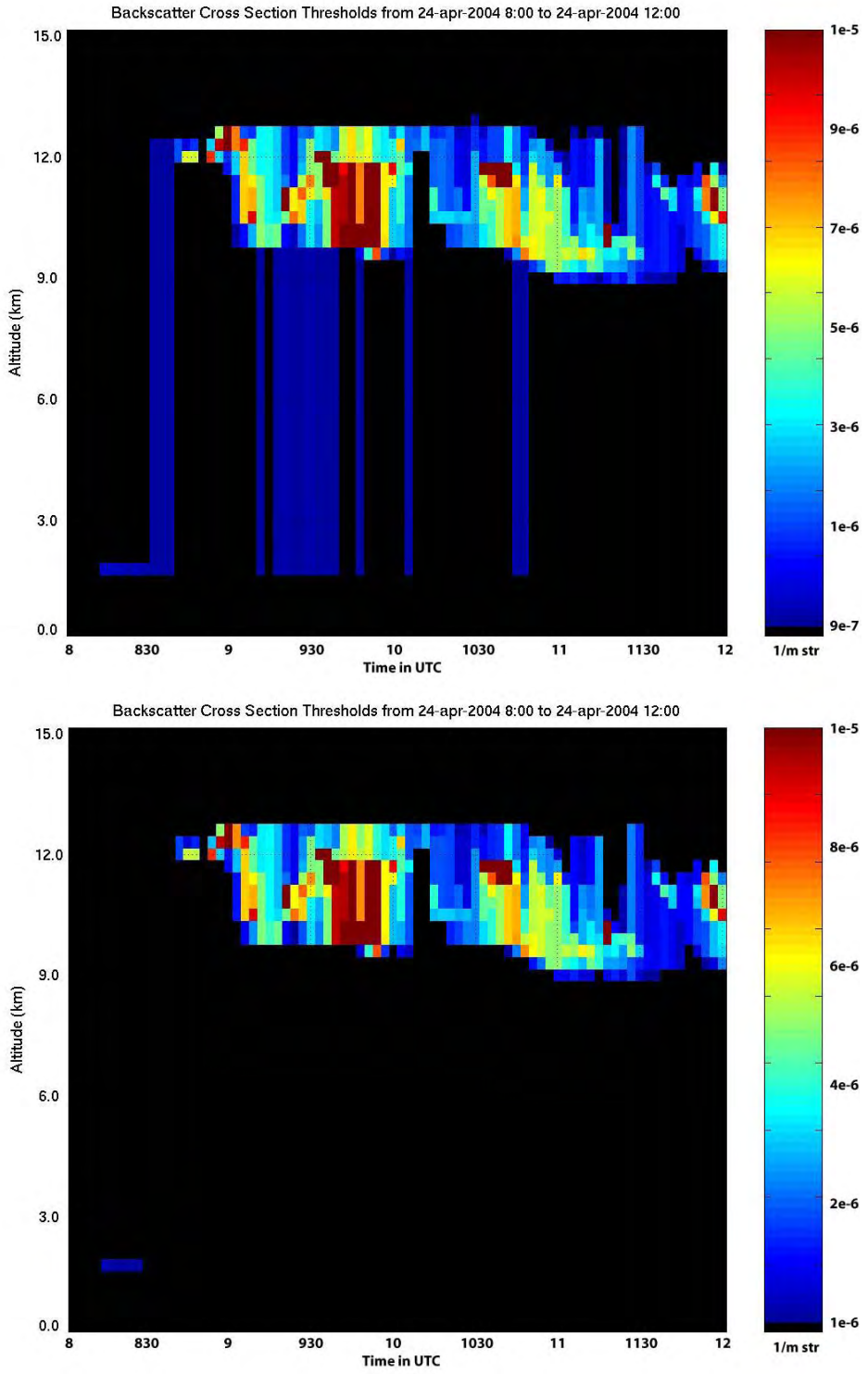

Figures 3.4 (C-D) – Cloud boundaries based on aerosol backscatter cross section thresholds of the cloud from April 24th, 2004. The thresholds range from 9e-7 to 1e-5 and 1e-6 to 1e-5 (m str)$^{-1}$, respectively. As seen, the best cloud detection threshold is 1e-6 (m str)$^{-1}$ in that it reveals no false boundary layer detection.

3.3 Cloud Boundaries Based on Optical Depth Thresholds

Once a suitable cloud base and top are identified by using a reasonable aerosol backscatter cross-section threshold, the total optical depth of the cloud in each time bin is calculated. From this point, an optical depth threshold is applied to determine cloud boundaries. In this case study, the example optical depth threshold used was 0.05 – that is, the algorithm located the data point identified as the backscatter cloud base, identified the optical depth of the cloud at that point, and increased the height bins until the optical depth had crossed the optical depth threshold. The same was done for the cloud tops by lowering the height bins until the threshold was crossed. This was done in order to show how the cloud base and top heights vary if different optical depth thresholds are applied. Figure 3.5 shows the optical depth plot for the same time profile shown in Figure 3.2. The cloud boundaries identified by the optical depth threshold are one height bin above and below the cloud base and top, respectively. Both the backscatter and optical depth defined cloud tops and bases are identified in the figure.

This procedure was then applied to the entire day involved in this case study, and the result is shown in Figure 3.6. Compared to Figure 3.3, the top height decreased slightly while the base height increased by a small number of height bins. Once again, the lower 2 km were removed to avoid the influence of the boundary layer. While the optical depth threshold of 0.05 was an example for this case, different optical depth thresholds were applied to the same time period in Figure 3.4. This is "zoomed in" on the cirrus between 8 and 12 UTC, and can be seen in Figure 3.7. This figure shows how the cloud fraction changes as various optical depth thresholds are applied ranging from 0.01 to 0.4, with an interval of 0.01.

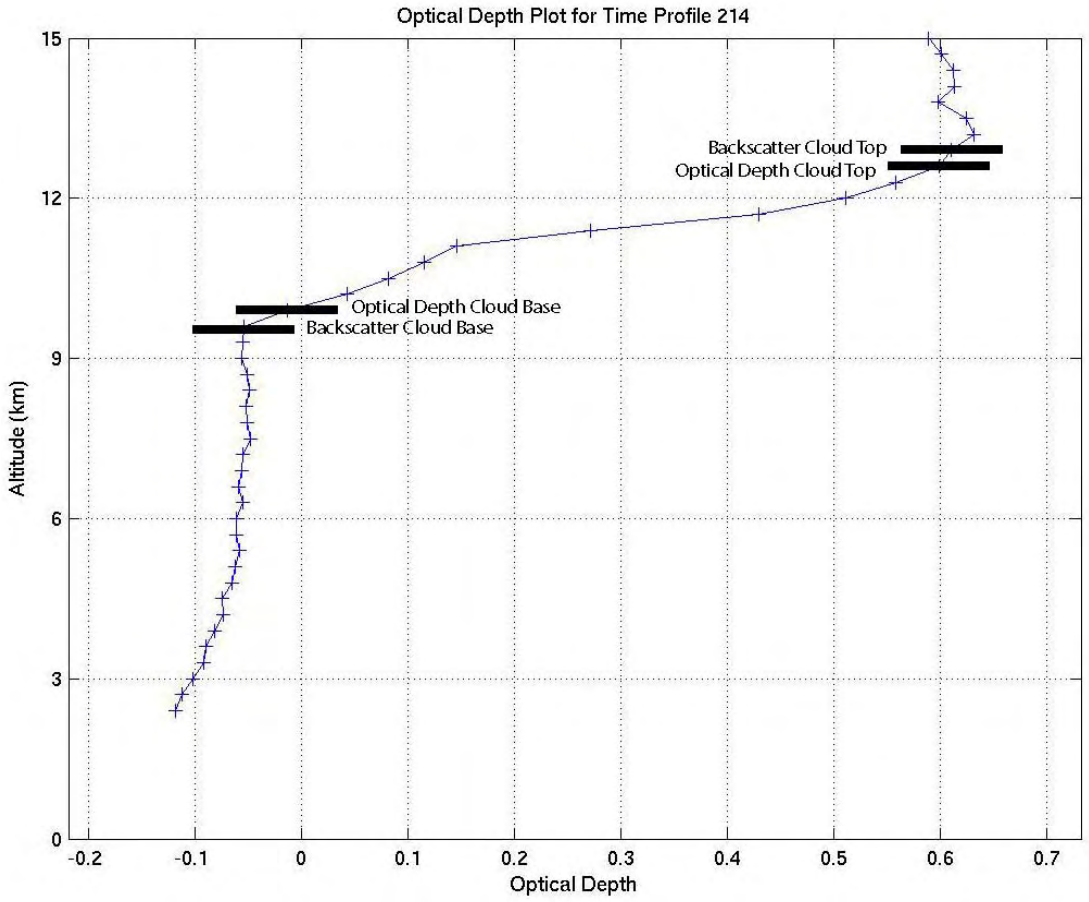

Figure 3.5 – An example of the optical depth profile for a single time bin at 1042 UTC. The backscatter threshold set detects the cloud base and height as the backscatter reaches 1e-6 (m str)$^{-1}$, and then applies an optical depth threshold to the cloud top and base height. Shown in the figure are the cloud top and base (as defined by the 1e-6 (m str)$^{-1}$ backscatter threshold) and the cloud base and top as defined by an optical depth limit of 0.05. In this case, the cloud boundary based on the optical depth threshold only changes the top and base by one height bin of 300 m.

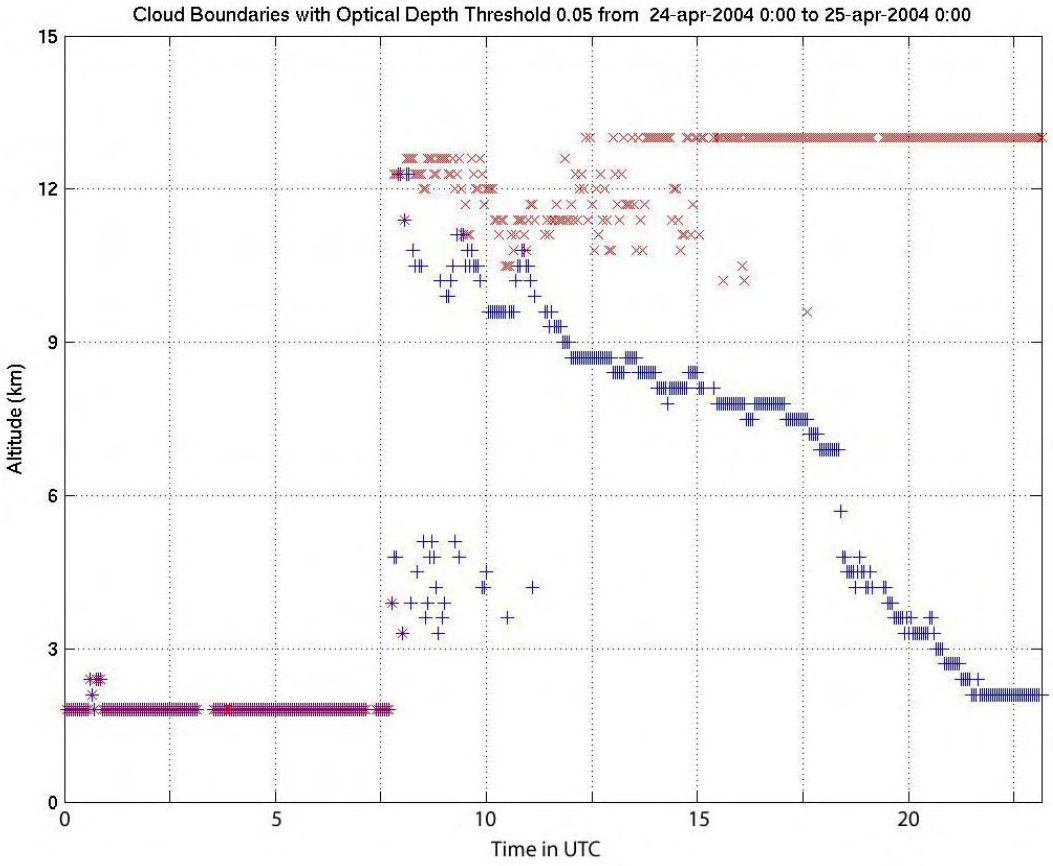

Figure 3.6 – Cloud boundaries as determined by an optical depth threshold of 0.05. Once again, the plus signs represent the cloud base while the x's show the cloud top. The aerosol backscatter cloud top was determined, and the algorithm searched for the next data point that passed an optical depth limit of 0.05 in this example. This development allows a given time period to be viewed with various optical depth thresholds. The same routine was applied to the cloud base.

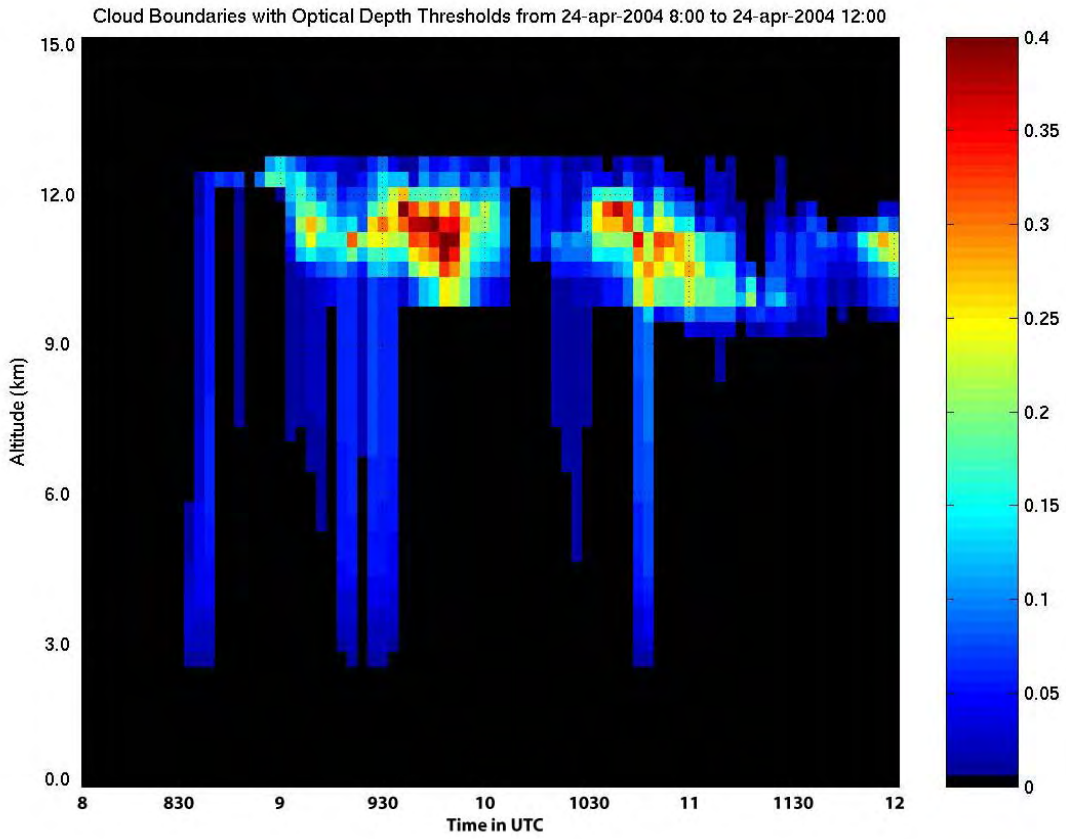

Figure 3.7 – An example identifying a cloud based on a series of optical depth thresholds between 0 and 0.4 for the case of 8-12 UTC on April 24th, 2004. Similar to Figure 3.4, this figure shows how the fractional coverage of the cloud changes when different thresholds are applied. An instrument with a lower threshold limit of 0.3 would not detect most of the cloud present in this image.

In summary, an aerosol backscatter cross section of 1e-6 $(m\ str)^{-1}$ was used to define the cloud base and cloud top because a sensitivity study showed this threshold detected the actual cloud more accurately and minimizes the impact of boundary layer aerosols. The total cloud optical depth is then calculated. For simplicity, all cloud optical depths greater than 2 were set equal to 2, symbolizing opaque clouds too thick for the cloud top to be identified by the ground-based lidar. Based on these applied optical depth thresholds, the total cloud fractional coverage can be calculated - this is the focus of Chapter 4.

Chapter 4

CLOUD FRACTION AS A FUNCTION OF OPTICAL DEPTH

4.1 Introduction

One purpose of this thesis is to investigate cloud fraction as a function of defining a cloud based on a series of optical depth thresholds. While Chapter 3 described the method of defining clouds based on an aerosol backscatter cross-section and optical depth thresholds, this chapter contains details on how cloud fraction is determined.

4.2 Cloud Fraction

The total cloud optical depth is calculated between the cloud base and top as determined by the selected backscatter cross-section of 1e-6 $(\text{m str})^{-1}$. Figure 4.1 shows the optical depth and the detected cloud phases for the example of April 24th, 2004. The figure shows that a small optical depth was detected from 0 to 8 UTC near 2 km, followed by a thin cirrus layer (shown as ice) beginning at 8 UTC. An optical depth of 2 (the maximum for this study) was first reached near 12 UTC, and for a few hours the cloud top was intermittently determined. The clouds remained optically thick throughout the day (as indicated by the "Max Cloud Depth Reached" markings. The vertical lines between 15 and 23 UTC indicate places where a change in the cloud phase was detected. This can be compared to the plot of the aerosol backscatter cross-section and depolarization (Figure 3.1). Multiple cloud phases are present in both figures after 15 UTC.

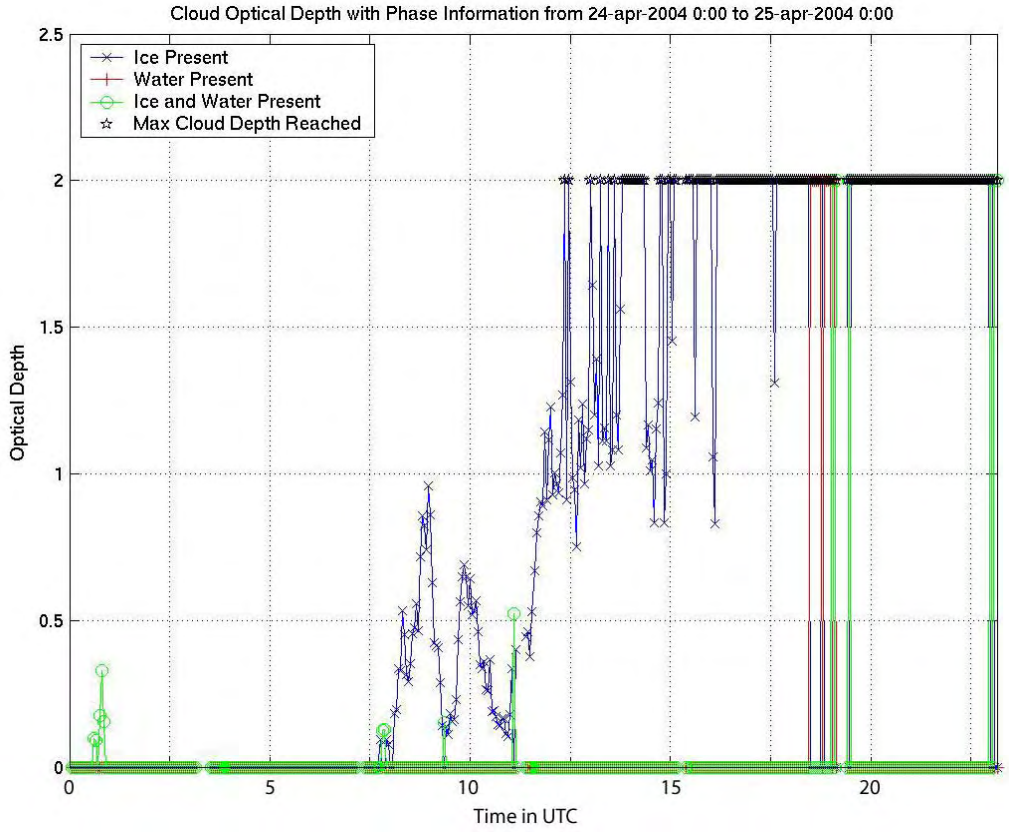

Figure 4.1 – April 24th, 2004, as a plot as the cloud optical depth vs. time. Also seen is the cloud phase and the moments the maximum cloud optical depth is reached at 2 km (as the black data points). The blue line represents time profiles of clouds that contain ice, the red line represents water clouds, and the green line shows profiles where both ice and water are present. The vertical lines between 15 and 23 UTC represent data points where the depolarization indicates changes in the cloud phase, even though the max cloud depth is reached. Notice that this example contains profiles containing both few mixed or water – this is due to nearly all water profiles leading to a "max optical depth reached" detection limit.

The cloud phase algorithm uses the measured depolarization at every level inside the cloud (based on the backscatter top and bottom) for each time profile. If only ice is present, the cloud is identified as ice; the same is true for water clouds. If both water and ice are present in the given time profile, regardless of the height of either, the algorithm indicates both phases are present, and should not be thought of as mixed phase clouds.

Frequently in the atmosphere, clouds precipitate both ice and liquid water, and if the molecular signal is attenuated substantially, the signal may not penetrate the ice precipitation in order to detect the water cloud above. In this case, the cloud would be identified by the algorithm as ice. While this may seem problematic, these are the cases where the maximum optical depth is reached, and no assumptions are made about the cloud phase; this is similar to the earlier mention of multilayer clouds.

Figure 4.2 shows the same cloud optical depth from Figure 4.1, but sorted by increasing optical depth. Instead of time on the X-axis, the scale has been converted to the total number of time profiles without the calibration periods and other missing data. The plot shows that for this case, the day of April 24th, 2004, approximately 140 of the total time profiles were clear sky (as indicated by a measured optical depth of zero above 2 km). Roughly 100 profiles had an optical depth of between 0 and 1 (shown by subtracting 140 from 240). Approximately 40% of the sky had an optical depth of 2 or above (subtracting 260 from 440).

Figure 4.3 uses the sorted data in Figure 4.2 to present how the cloud percentage of the sky changes as a function of the different optical depth thresholds. Plots of this nature show the cloud fraction as a function of a minimum optical depth threshold. For example, the case of April 24th, 2004, an instrument with a minimum optical depth detection limit of 0.2 would have viewed a cloud cover of 62% while an instrument whose lower limit is 1 would see a cloud cover of 46%.

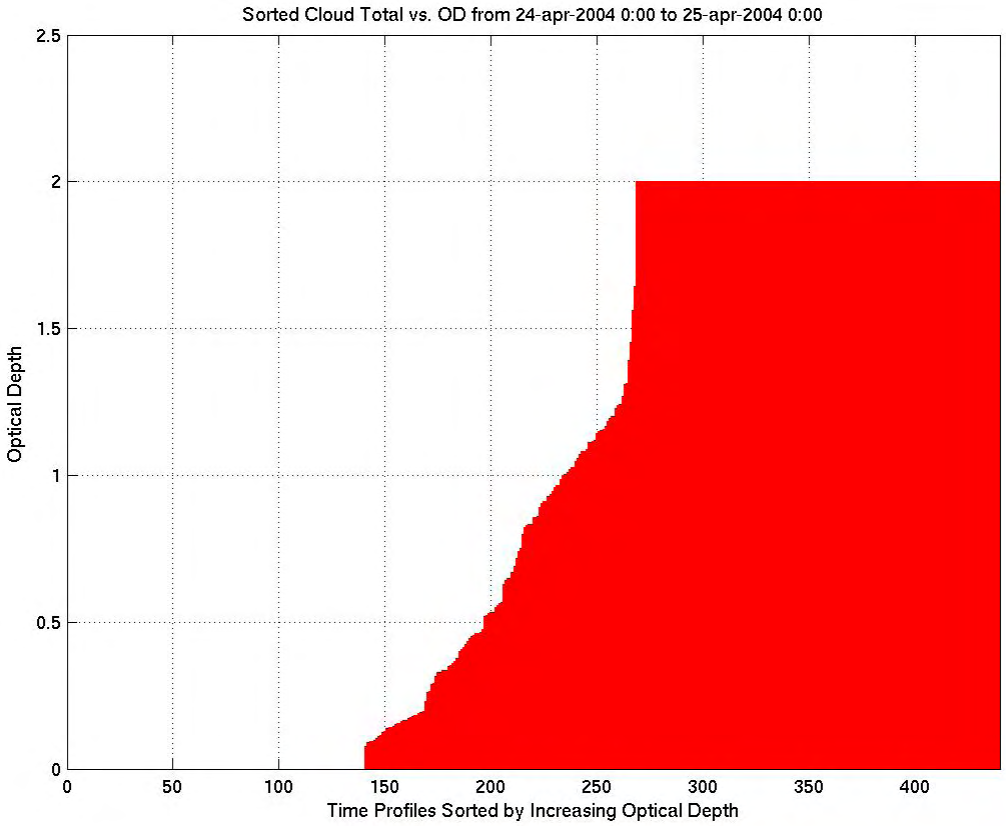

Figure 4.2 – The total sorted optical depth from Figure 4.1 (April 24th, 2004). The number of clear sky cases can be viewed from this graph (around 140 time bins, or around 33%), as well as the number of times the cloud reached an optical depth of 2 (a little over 180 time profiles, or around 40% percent of the entire day). Calibration and missing data are removed from this plot, and only profiles with optical depth information are shown.

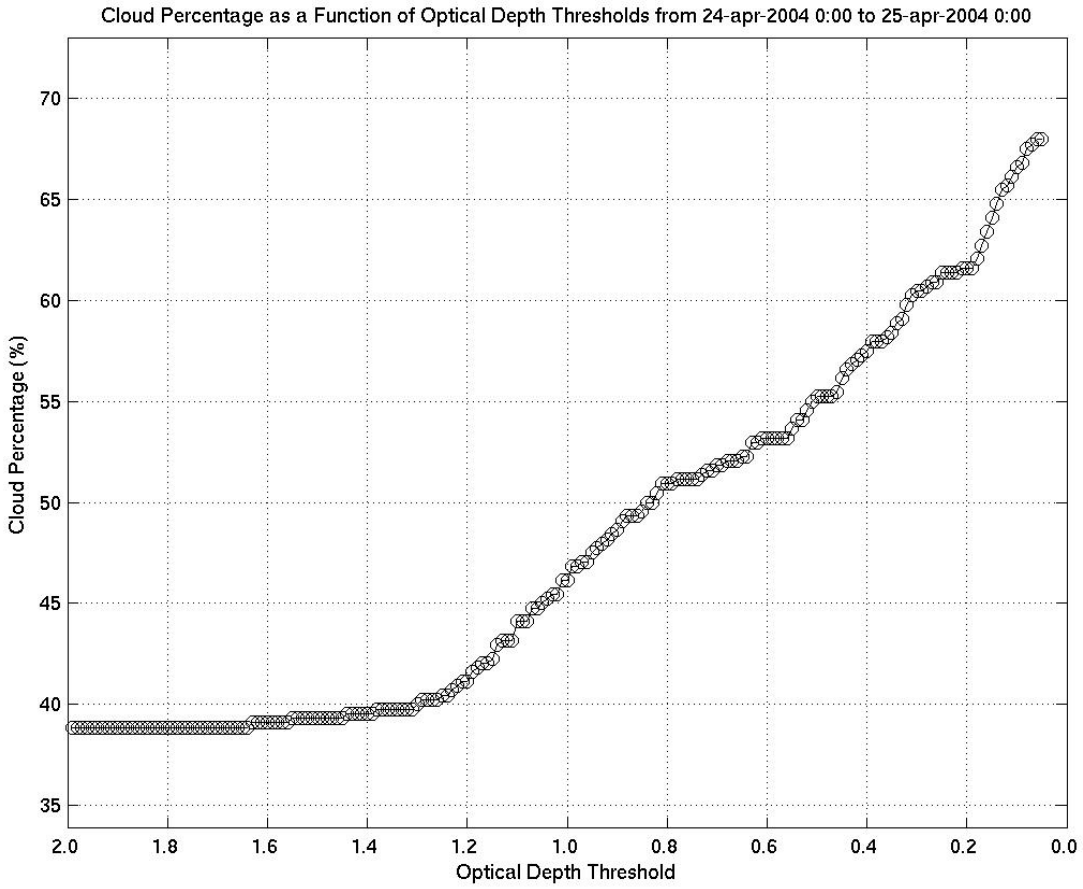

Figure 4.3 – Cloud probability as a function of optical depth for the day of April 24th, 2004. This plot shows that if an instrument has a lower optical depth threshold of 0.2, the detected cloud cover will be 62%. If an instrument had a lower optical depth threshold of 0.8, it would see around 51% cloud cover. Most clouds in this example had optical depths between 0 and 1.2, as seen in the figure.

Figure 4.3 shows that there was little difference in the cloud cover percentage between instruments that had a lower optical depth limit of 2 compared to a lower limit of 1.2. If a given satellite required validation and measured a 60% cloud cover, we can deduct that the lower optical depth limit of the instrument is near 0.3.

4.3 Temporal and Spatial Average Comparison

To better understand errors associated with temporal and spatial averaging on cloud fraction, a comparison study was done in which these averages were varied. Figure 4.4 shows a temporal comparison for the month of June 2004 with three cloud percentages determined using a 300-meter vertical average and a 1, 3, and 5-minute temporal average of each of the calculated parameters (optical depth, depolarization, aerosol backscatter cross-section). By using these different time averages, the overall cloud fraction does not change more than a few percent. For thin clouds, changing the temporal average has little impact on the cloud fraction. Thin clouds stretch for kilometers with small variations in optical depth, and thus averaging over time scales between 1 and 5 minutes has little impact on the cloud fraction. Thicker clouds, however, are more affected by non-linear effects in the lidar optical depth equation. By using a smaller time average, the cloud fraction increases slightly because thicker clouds are not averaged with any cloud "holes", increasing the optical depth. In contrast, when the averaging time is increased, thicker clouds are averaged with these "holes" and surrounding clear sky, therefore causing the measured optical depth to decrease.

Figure 4.5 shows 3-minute averaged cloud fractions with 150, 300, and 600 m vertical averages over the month of June 2004. By viewing this spatial averaging comparison, the cloud fraction is once again not dramatically changed by altering the vertical resolution while maintaining a constant temporal average of 3 minutes. As the resolution becomes smaller (150-meter), the cloud fraction increases for all cloud optical depths. When the spatial resolution becomes greater (600 meter), the cloud fraction is decreased for all optical depths. This is due to the fact that as the spatial resolution increases, the optical depth measurements become more

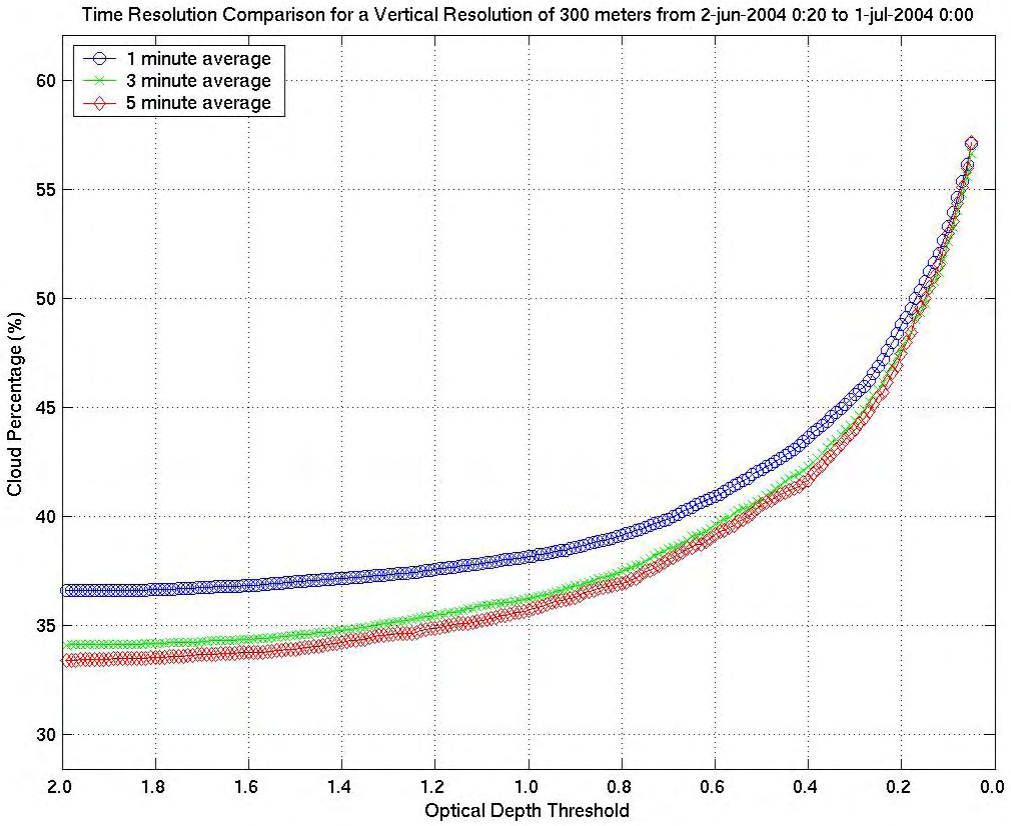

Figure 4.4 – A temporal resolution comparison plot for the month of June 2004, showing the cloud fraction for a 300-meter spatial average and a 1, 3, and 5-minute temporal average. By comparing how the various temporal averages alter the cloud percentage, one can make a visual argument that changing the temporal average does not radically affect the overall cloud fraction. When the time average is reduced to a 1-minute average, the lidar signal tends to "see" the same amount of optically thin cloud and a slight increase in the percentage of thicker clouds (optical depths greater than 1.0). In contrast, by using a 5-minute average, while the amount of detectable thin clouds remains the same, the cloud fraction for thicker clouds is reduced. This is due to averaging the edges of clouds with surrounding clear sky – effectively reducing the measured optical depth.

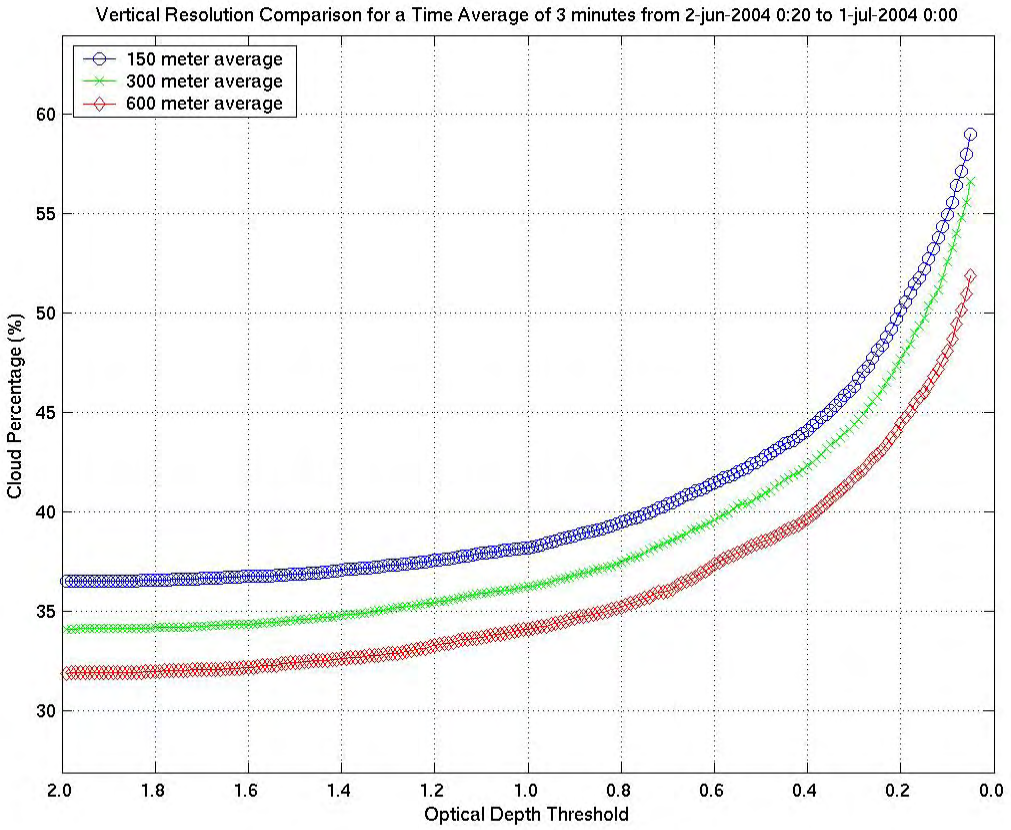

Figure 4.5 – A spatial resolution comparison plot for the month of June 2004, showing the cloud fraction for a 3-minute time average and a 150, 300, and 600-meter spatial average. Overall, the change by using difference spatial averages is only a few percent for both thick and thin clouds. By using a 3-minute time average, a compromise is set between a reasonable resolution for detection cloud boundaries and eliminating noise in the molecular signal.

susceptible to uncertainties in the molecular return. Oftentimes at cloud tops, the molecular return becomes noisy (leading to noise in the optical depth profiles), and this noise frequently causes the algorithm to register a greater optical depth, causing an increase in cloud fraction. As the resolution is decreased, these variations are averaged out, and a more accurate optical depth is recorded. As a result, a 3-minute time average was used in the remainder of this thesis as a compromise between averaging out noise when cloud tops are identified and having a suitable resolution for cloud top and base measurements.

4.4 Optical Depth Error Estimates

Section 2.6.2 explained how the errors associated with optical depths are calculated and presented an example optical depth profile. The algorithm calculated the error coupled with each optical depth profile (based on the molecular signal), and recalculated the cloud fraction based on the adding and subtracting the standard deviation (STD) of each profile. This is represented by Cloud Percentage (PERC) + STD and Cloud Percentage – STD in the text and in Figure 4.6.

There are two cases to consider that will explain both ends of the plot (thick and thin clouds). When a cloud is optically thick, the standard deviation (STD) is often very large due to the small number of returned molecular photons. Hence, percentage (PERC) + STD will yield a number larger than 2 (not included on this graph), and PERC – STD will sometimes result in a negative number (if the molecular signal drops below zero, the optical depth is undefined). For this reason, when a cloud is identified as OD ≥ 2, the STD is set to zero, to avoid such cases. In Figure 4.6, PERC+STD shows an increased cloud fraction due to clouds with OD > 1.5 being identified closer to OD = 2 while PERC-STD is equal to the original cloud fraction. In short, this states that if the cloud is thick, we are very certain of it.

When a cloud is optically thin (less than 0.1), the errors are due to the density profile and the molecular return. While the error percentage for such cases can easily exceed 100%, the actual errors are only around an optical depth of up to 0.1. Thus, for a thin cloud with

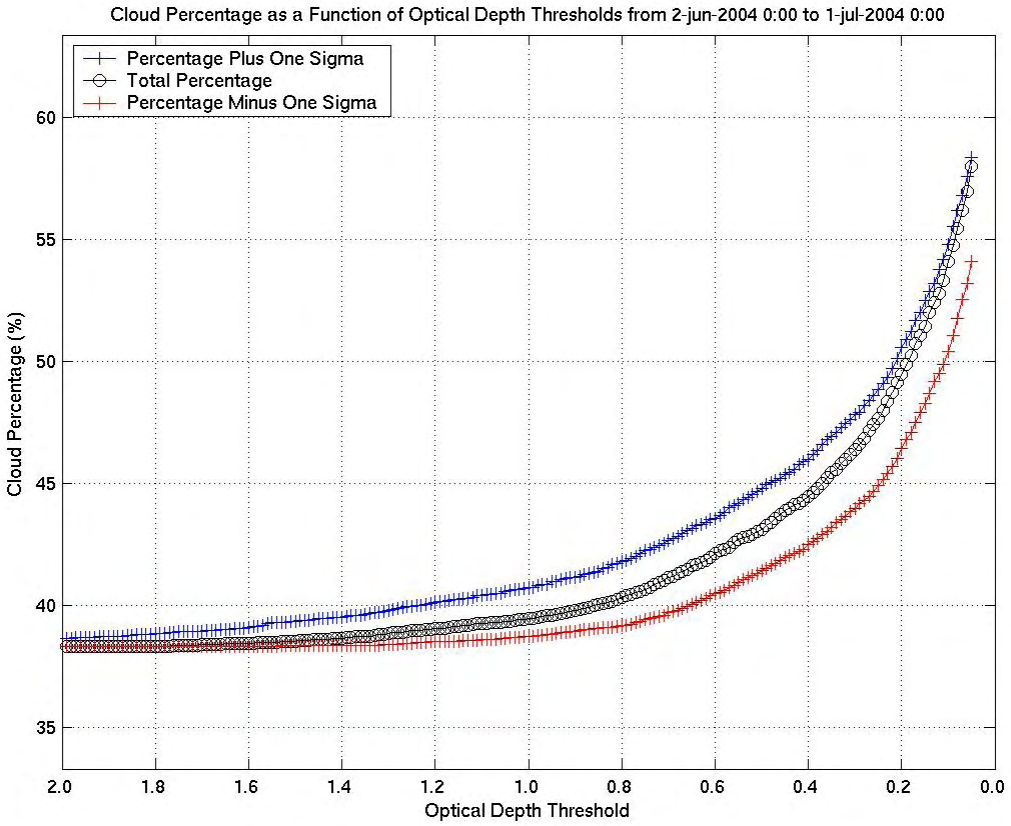

Figure 4.6 – A plot showing the total cloud fraction as well as the cloud fractions when considering the plus sigma and minus sigma values of optical depth from June 2004. Each optical depth time profile has an associated error bar due to the molecular return and the density profile (see Section 2.6.2). The error associated with thin clouds is small, mostly due to uncertainties in temperature and pressure of the radiosonde. As the thickness of the cloud increases, the errors are due to a decrease in molecular-scattered photons.

PERC+STD, the fraction increases by a trivial amount. With PERC-STD, however, the clouds can be reduced to OD = 0, or clear sky. Thus, the cloud fraction is decreased by a few percent.

This error analysis shows that using different temporal averages, spatial averages, and optical depth error estimates, the cloud fraction changes by only a few percent. Although plots in Chapter 5 will not include the associated error bars, the assumed error for cloud fraction plots will be on the same order as the "error lines" as seen in Figure 4.6.

4.5 Additional Case Studies

Along with the presented case of April 24th, 2004, two additional case studies were used to test the reliability of the algorithm. While the first example showed a case of both high cirrus and low precipitating clouds, the following two case studies focus on thin cirrus overpasses of February 16th, 2004, and May 15th, 2004. The next case study shows thin cirrus above a water cloud precipitating ice, and the final case study will show results from a single thin cirrus case.

4.5.1 February 16th, 2004

Between the hours of 8 and 12 UTC on February 16th, 2004, a layer of thin cirrus with a height of around 9 km passed over a water cloud precipitating ice between 3 and 6 km. Figure 4.7 shows the aerosol backscatter cross-section and the cloud depolarization. In the upper plot, the thin cirrus and precipitation appear as green and yellow, while the water cloud, having a high backscatter cross section, is in red. The depolarization confirms the upper clouds and precipitation are ice (shown in red) and the mid-altitude cloud between 930 and 1030 UTC is water (shown in dark blue).

In Chapter 3, the method in which the algorithm deals with multilayer clouds was discussed. To review, the program was designed to calculate the total optical depth for each time profile, and therefore the lower cloud's base and the upper cloud's top defined the total "cloud" in each profile.

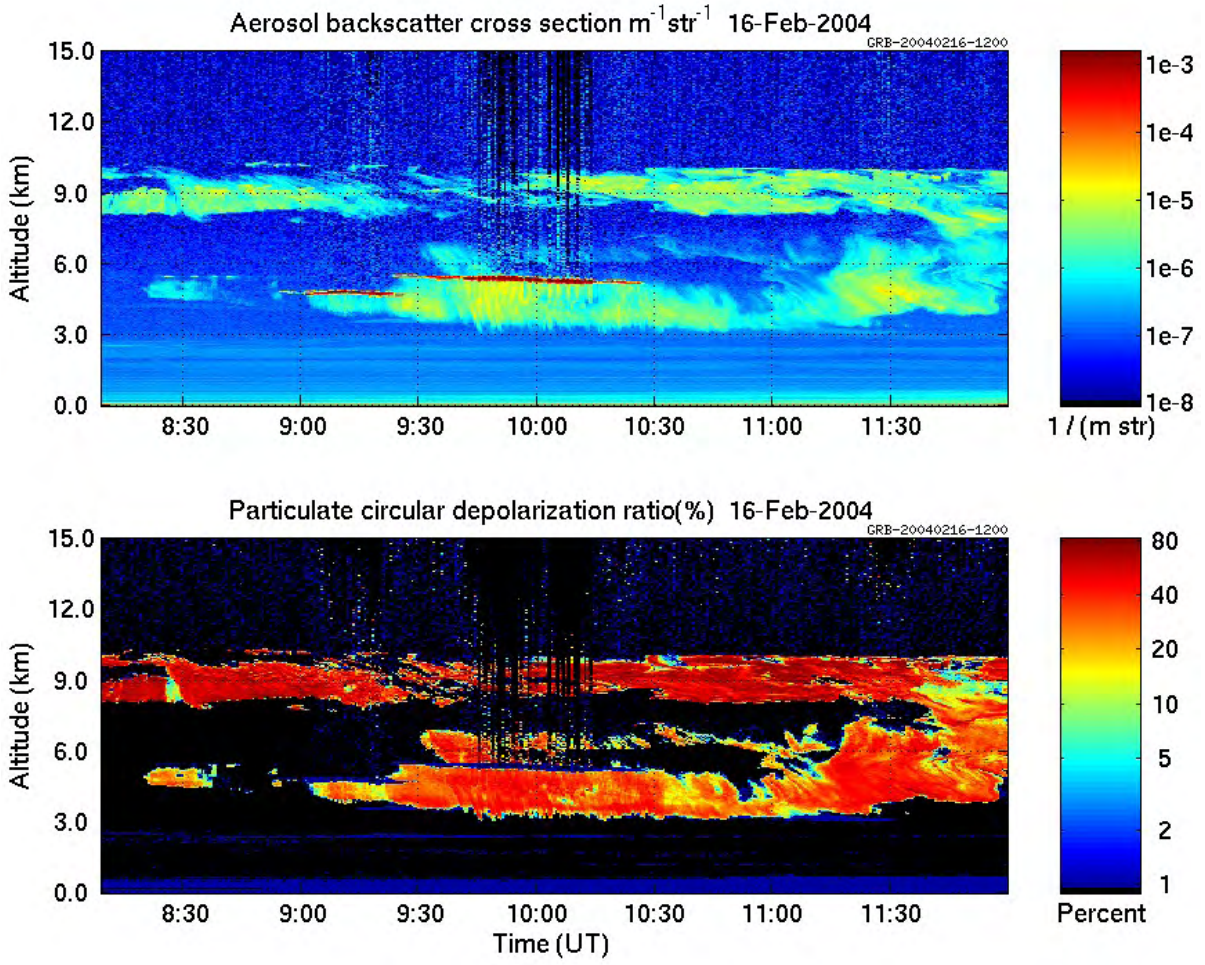

Figure 4.7 – The case study of February 16th, 2004 from 8-12 UTC. This case was chosen because of the presence of thin cirrus and a water cloud precipitating ice. Multilayer clouds are difficult for the lidar to detect, due to the common presence of opaque lower clouds. The upper plot shows the backscatter cross section of clouds while the lower plot shows the depolarization of the clouds. Red indicates ice and blue shows the presence of water.

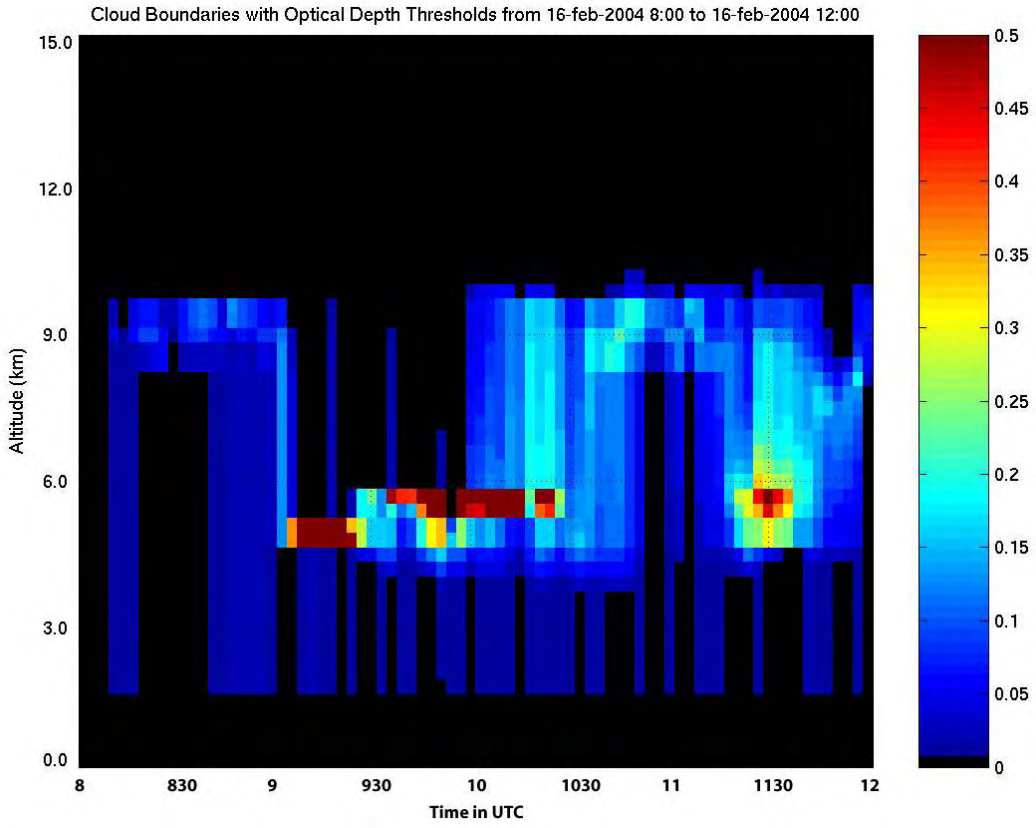

Figure 4.8 – The case study involving multilayer clouds as shown by using different optical depth thresholds. The color scale varies between 0 and 0.5. The water cloud can be seen in red, due to the high optical depth. The algorithm calculates only the total optical depth of each time profiles, and as such, the lower cloud's base and upper cloud's top determine the cloud boundaries. Also noteworthy is how at thin optical depths, the algorithm detects boundary later haze.

Applying optical depth threshold of between 0 and 0.5, the image in Figure 4.8 was created. As seen in the figure, low optical depth causes the haze in the boundary layer to be falsely detected as the cloud base. Once a threshold of around 0.1 is reached, the actual cloud boundaries can be identified. Due to the presence of multilayer clouds, the cloud base and height spans several kilometers. The thicker water cloud can be seen due to its relatively high optical depth (greater than 0.5).

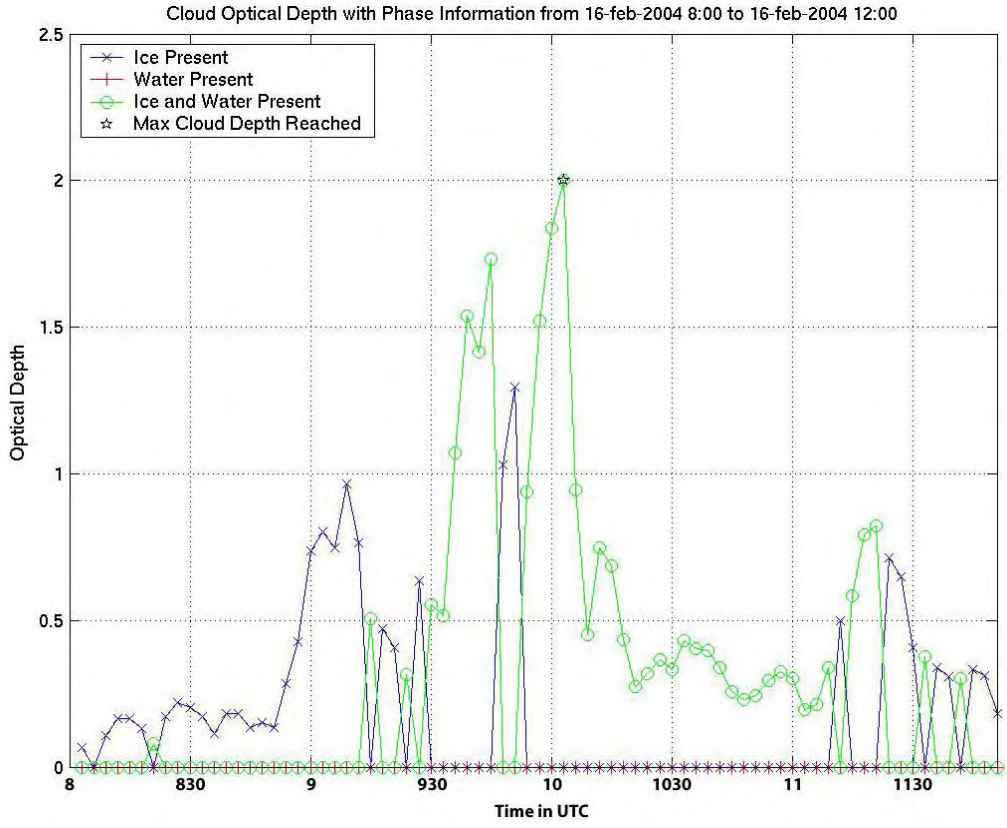

Figure 4.9 – The total optical depth of the cloud from February 16th, 2004. The phase information shows that only ice was present between 8 and 9 UTC, and that both ice and water were measured until 1130 UTC. Although the depolarization plot indicated a water cloud between 930 and 1030 UTC, the cloud was precipitating ice, causing the algorithm to be triggered at a lower altitude. The optical depth of only one time profile reaches the lidar maximum value of 2, as seen on the plot.

The phase information contained in Figure 4.9 shows that only ice was present until 9 UTC. This is due to the presence of the lower water cloud precipitating ice and the presence of the upper level ice cloud. While most of the multilayer optical depth is less than 1, the maximum detected optical depth reaches 2.0 near 10 UTC. There are no cases identified where only water was present.

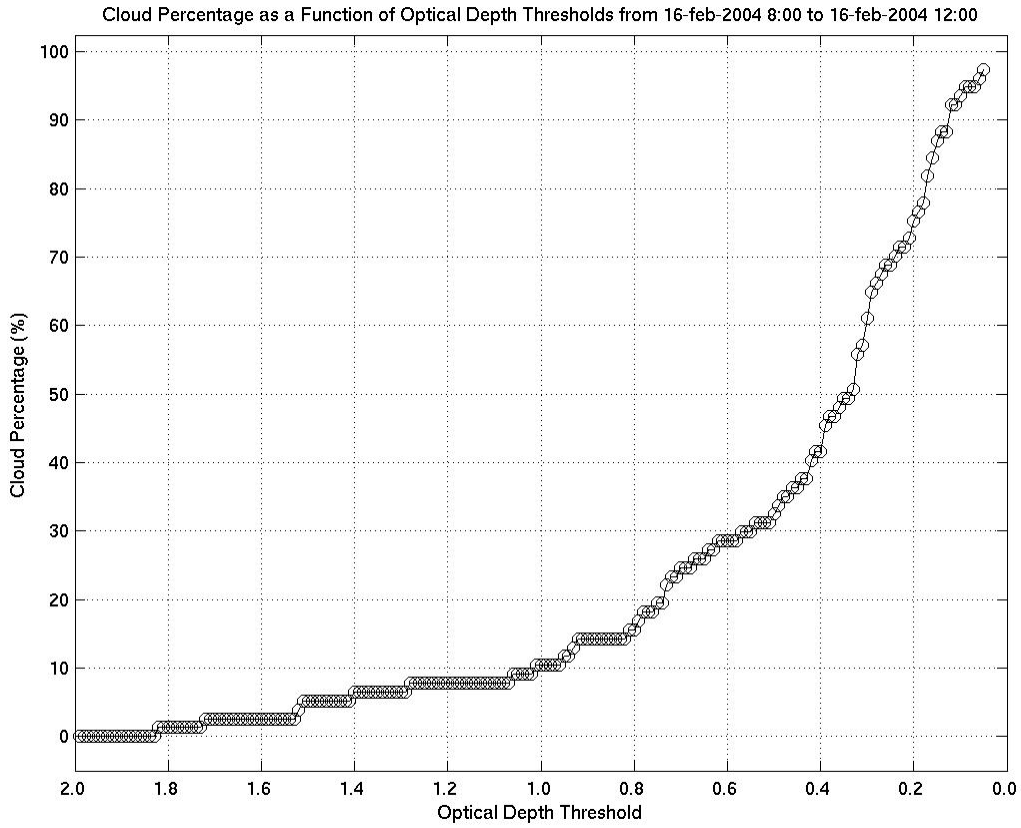

Figure 4.10 – Cloud percentage as a function of optical depth for the second case study. In this time period, nearly 100% of the sky had some measurable amount of cloud optical depth. An instrument with a lower optical depth limit of 0.4 would see around 40% cloud cover, with the percentage of detected clouds decreasing rapidly as the lower threshold increases.

By sorting the total cloud optical depth in Figure 4.9 and calculating the cloud percentage based on optical depth thresholds, Figure 4.10 was produced. The lidar detected clouds with a measurable optical depth in nearly 100% of the profiles in this case study. The amount of detectable cloud cover decreases rapidly as the optical depth threshold increases, with less than 1% of the clouds in this case having an optical depth of more than 2. An instrument with a lower optical depth threshold of 0.4 would only detect less than half the clouds present.

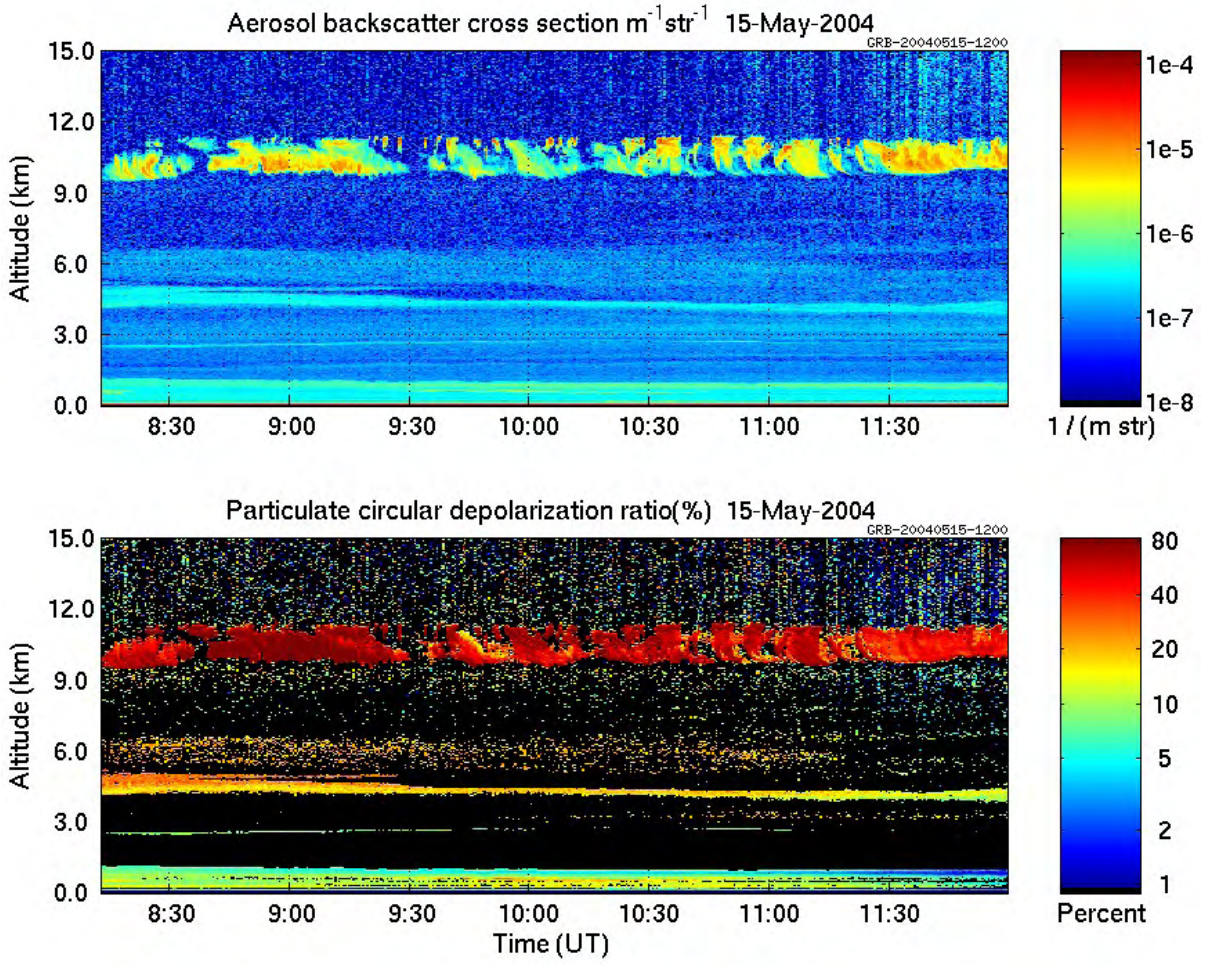

Figure 4.11 – The case study of May 15th, 2004 from 6-12 UTC. The upper plot shows the backscatter cross section of a high cirrus cloud with a hazy boundary layer. The cross polarization channel shows that the upper-level cloud is ice, as expected. Also shown is the presence of some aerosol backscatter with a height near 4-5 km with a depolarization between 15-25%.

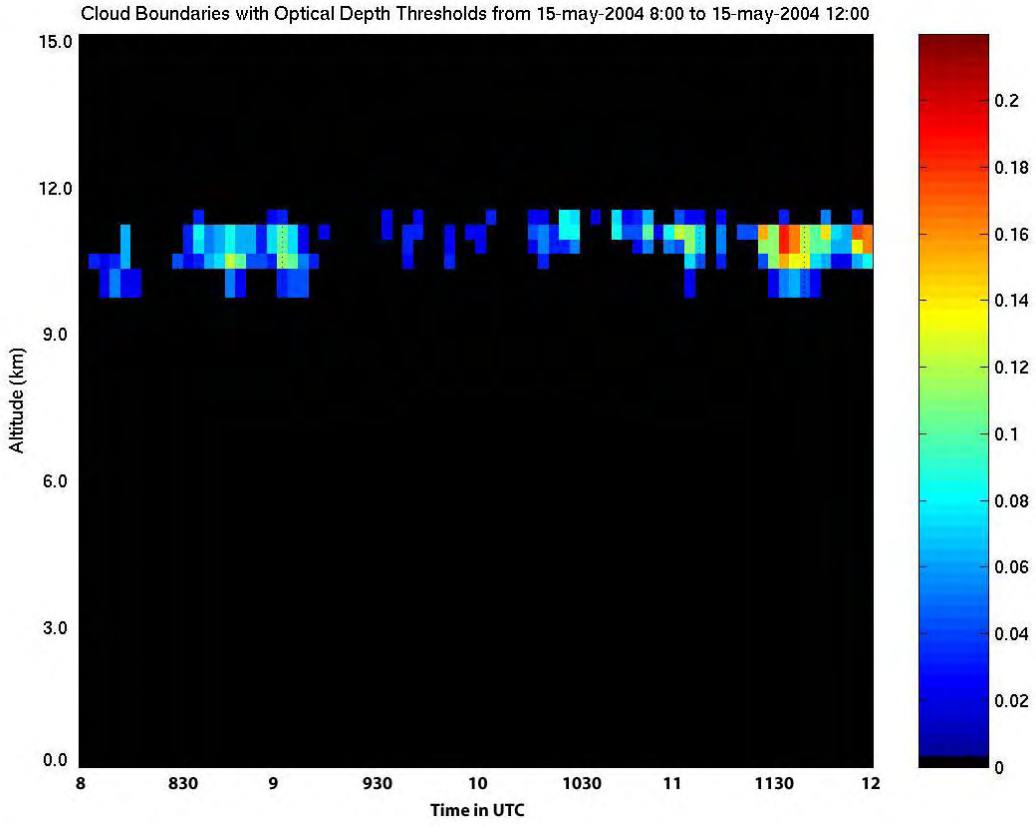

Figure 4.12 – The cloud of May 15th, 2004, as seen with optical depth thresholds between 0 and 0.25. The thickest part of the cloud occurs after 1130 UTC, although the cloud is optically very thin. While Figure 4.11 shows a small amount of backscatter around 4.5 km, time profiles containing optical depths less than 0.05 were removed to eliminate possible errors.

4.5.2 May 15th, 2004

The case of May 15th, 2004, shows a high cirrus cloud between the hours of 8-12 UTC consisting of ice. This can be seen in Figure 4.11. The boundary layer has a small amount of what can be assumed to be dust and haze, and a small amount of backscatter cross-section can be seen between 4-5 km with a depolarization of between 15 and 25%. Due to the thin optical depths, however, any profiles with a total optical depth of less than 0.05 were removed to eliminate errors near the lower optical depth detection of the lidar.

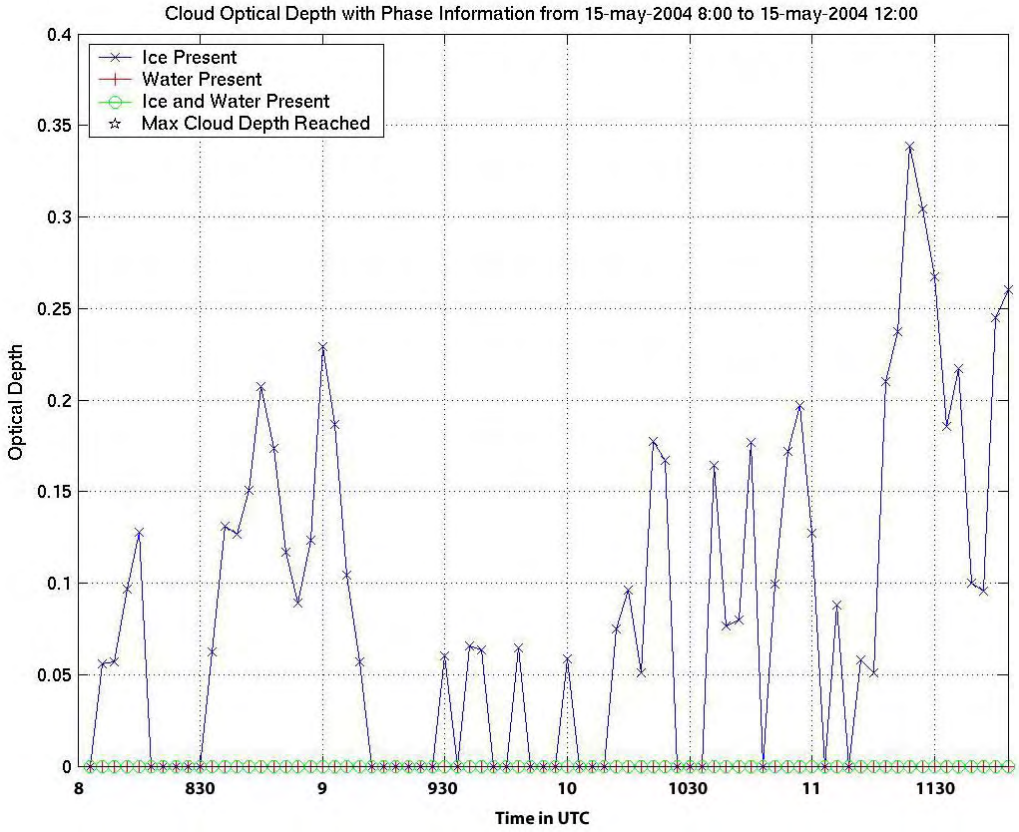

Figure 4.13 – The total cloud optical depth of the second case study (the case of May 15th, 8-12 UTC). Most of the cloud has an optical depth of less than 0.25, while the optical depth reaches a maximum of just under 0.35 around 1130 UTC. The cloud is made up of ice (as expected based on the position in the atmosphere).

Figure 4.12 shows the cloud as a series of optical depth thresholds were applied, ranging from 0.05 to 0.25. At a threshold of 0.25, only a small fraction of the cloud was visible – the period between 1130 and 12 UTC. The total cloud optical depth can be seen as a function of time in Figure 4.13.

Figure 4.14 shows similar results to that of Figure 4.10 in that a high amount of the sky has cloud coverage if the threshold is low enough. An instrument with a lower threshold of 0.3 would view clear sky. These case studies stress the importance to know the lower optical depth threshold of an instrument in order to acknowledge the amount of undetectable cirrus.

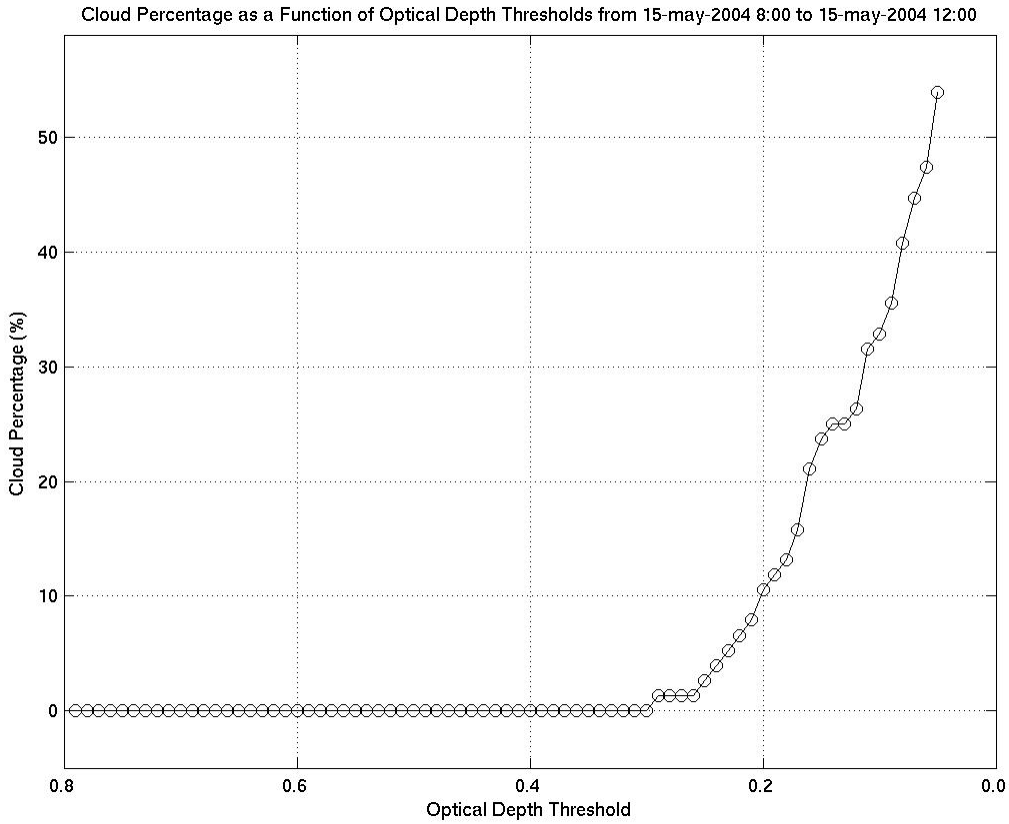

Figure 4.14 – Cloud percentage as a function of various optical depth thresholds for May 15th, 2004. Cloud coverage for this case was approximately 55% when the lower detectable limit was 0.05. A sharp decrease is shown as the threshold increases, showing a cloud percentage of approximately 10% at a lower limit of 0.2.

Chapter 5

RESULTS OF A TWELVE-MONTH STUDY AND DISCUSSION

5.1 Cloud Percentage over Twelve Months of Lidar Data

The focus of the thesis is to classify the fractional cloud coverage as a function of various optical depth thresholds. The purpose of setting a variety of these thresholds is to demonstrate how the cloud fraction changes when viewed with instruments of different optical depth detection limits. In the same style as Figure 4.3, Figure 5.1 shows how the cloud fraction varies between optical depths limits of 0.05 and 2.0 for one year of lidar data from September 2003 through August 2004. For the plots in this chapter, the lowest kilometer of lidar data was removed in order to avoid detecting the haze and dust commonly associated with the boundary layer.

While removing these lower atmosphere obstructions avoids false cloud detections, one drawback is that thin clouds at this altitude are also removed from the data set if the backscatter threshold is not greater than 1e-6 $(\text{m str})^{-1}$ at 1 km. All optically thick clouds below this altitude are included in the data set due to their higher backscatter cross-section and molecular channel attenuation at 1 km.

The most noteworthy point on this plot is that the cloud percentage increases nearly 15% when the optical depth threshold is changed from 0.05 to 2.0. Around 50% of this fraction changes between the thresholds of 0.05 to 0.5. This has major implications for instruments on satellites searching to discover the lowest detectable optical depth. If an instrument such as MODIS claims to detect clouds with an optical depth as low as 0.3, these results show it is not

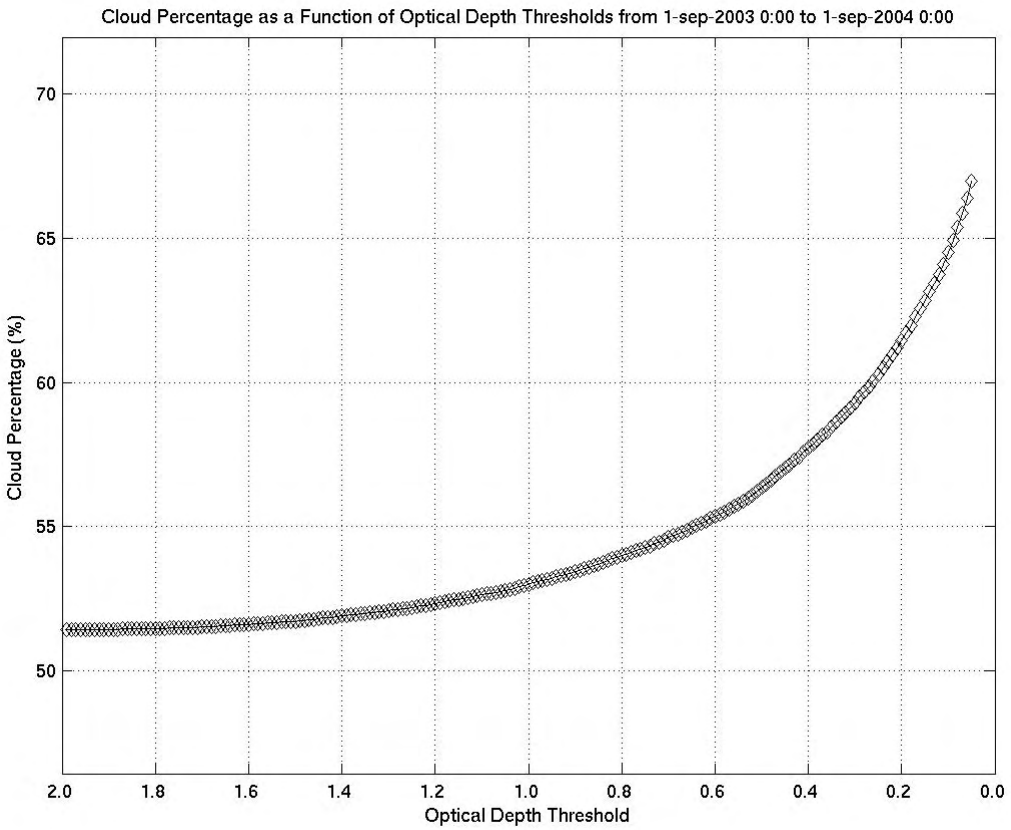

Figure 5.1 – The cloud percentage as a function of various optical depth thresholds ranging from 0.05 to 2. This plot was created from twelve-months of lidar data from September 2003 through August 2004 while the lidar was operating from a rooftop in Madison, WI. The lower kilometer of data was removed to avoid haze and dust from the boundary layer. Any low clouds below 1 km were included due to the molecular signal attenuation and high backscatter cross section present at 1 km. A 15% increase of the total cloud cover was identified as the optical depth threshold decreases from 2 to 0.05, with most of the increase occurring between the thresholds of 0.05 to 0.5.

detecting around 10% of the clouds the AHSRL can detect. Around 33% of the twelve-month period contained clouds with an optical depth less than 0.05, or what was classified as clear sky.

5.2 Optical Depth Results as a Function of Altitude

By dividing the cloud percentage found in Figure 5.1 by altitude, we gather information about the presence of thin clouds. Along with calculating the cloud coverage over the twelve-month period, the average cloud height is determined for each time profile. The cloud coverage can be determined as a function of increasing altitude and as a function of using the optical depth thresholds ranging from 2 to 0.3. For example, near the surface, mostly optically thick clouds are present. The cloud fraction is nearly the same regardless of the optical depth threshold. As the altitude increases by a few kilometers, the presence of optically thin clouds is noticeable, and the total cloud coverage increases. Therefore, a divergence will appear between optical depth thresholds depending on the amount of thin clouds. Eventually, when all clouds are detected in a give time period, the cloud fraction can be determined for each of the optical depth thresholds. This is the basis for Figure 5.2 – a "cumulative" cloud fraction based on increasing altitude.

Figure 5.2 shows the same data from the twelve month set divided into cloud fraction as a function of altitude for the various optical depth thresholds. That is, the ten curves show the cloud fraction as viewed with that optical depth or greater. A cloud with an optical depth of 0.6 would not be included in the curves with a threshold of 1. Since the change in cloud coverage is more significant with thinner clouds, more threshold curves were placed between 0.03 and 0.6 than between 0.6 and 2.

The figure shows that each of the optical depth threshold lines converge near the 1 km lower limit, due to the increased presence of clouds with a high optical depth. The cloud cover at this altitude is around 25%, and divergence between the threshold curves occurs between 2 and

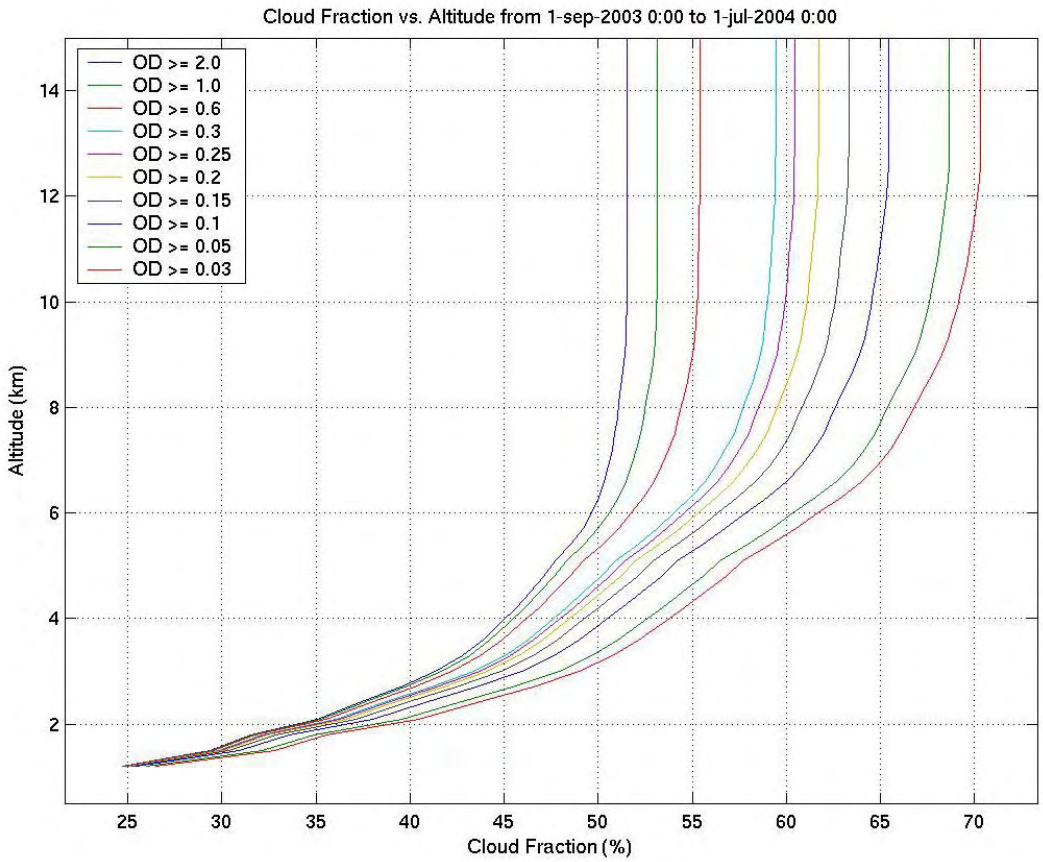

Figure 5.2 – The cloud fraction as seen looking from the ground up, as a function of various optical depth thresholds. This plot contains data from the twelve-month data set between September 2003 and August 2004. For each time profile, the average cloud height was determined, and this was performed for each of the optical depth thresholds seen in the picture. The optical depth curves converge at the lower cutoff of 1 km because of the presence of only optically thick clouds at that altitude. In this case, clouds were present at 1 km nearly 25% of the twelve-month period. The optical depth threshold lines diverge as the altitude increases due to the presence of thinner clouds. The lines eventually become vertical, showing the total cloud fraction at that optical depth threshold. As can be seen, this plot shows that the cloud fraction at a given altitude changes significantly based on the optical depth threshold used. For example, at an altitude of 6 km, there is almost a 13% change in the cloud cover as seen between instruments with an optical depth lower threshold of 2 as opposed to an instrument with a lower threshold of 0.03.

6 km. As the altitude increases, the threshold lines diverge more rapidly– indicating an increase in the presence of optically thinner clouds at higher altitudes.

Using optical depth thresholds of 0.03 and 2 for the twelve-month period, there is a 13% increase in the amount of cloud cover at 6 km and nearly a 20% increase by 12 km. By reading the values where the optical depth curves reach 15 km, the cloud fraction for each threshold can be identified. This shows that around 52% of the total cover contains clouds too opaque for the lidar to penetrate (optical depth of 2 or greater).

Figure 5.3 shows the cloud fraction as a function of altitude for various optical depth thresholds, but in a "top-down" format, such as the view from a satellite. This plot is useful for viewing the change in altitudes at which a certain cloud fraction is reached. Beginning at a cloud fraction of 0 for an altitude of 14 km (as expected based on the lack of clouds at that height), the curves separate within a few kilometers due to the presence of only optically thin clouds at that height. The cloud coverage for the threshold of 2 is 0 until 9 km. The divergence of these clouds increases as the altitude decreases, and near the ground, the presence of thick clouds causes the cloud fraction to increase significantly. The maximum divergence reaches around 15% near the surface - the same values at determined in Figures 5.1 and 5.2.

For a cloud fraction of 10%, there is nearly a 3 km average cloud height difference between the optical depth thresholds of 0.03 and 2. The difference at a cloud fraction of 20% is less than a 2 km difference, but the difference is still noteworthy. This information is useful in showing that significant difference in the average cloud height will occur depending on an instrument's optical depth limit of detection. To remind the reader, the lidar cannot see above thick clouds, and as a result, the "thin" cloud fractions (OD ≥ 0.1, ≥ 0.6, etc.) in this figure only represent those clouds that were not first obstructed by lower, thick clouds.

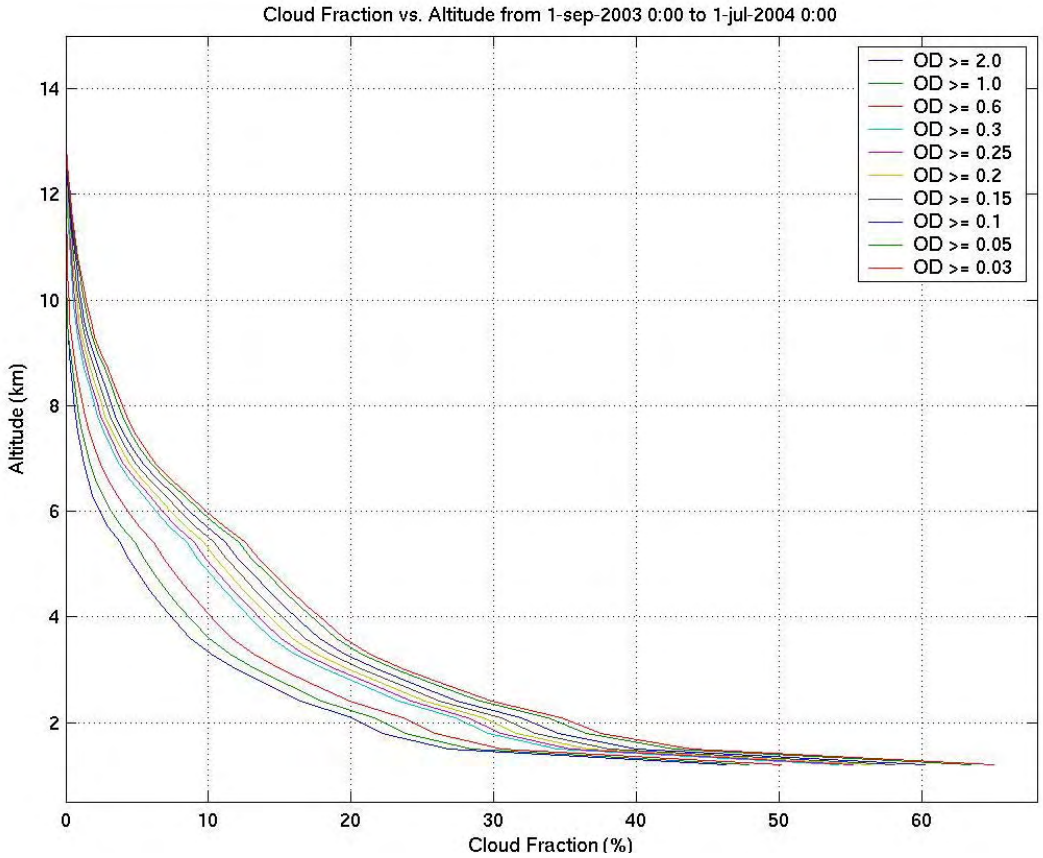

Figure 5.3 – This plot shows same information contained in Figure 5.1 in a "top down" format, such as the view a satellite would see. Each of the optical depth threshold curves converges with a cloud fraction of 0 at an altitude of 13 km (indicating the presence of no clouds at or above that altitude). As the altitude decreases by a few kilometers, only thin clouds are present, while the amount of cloud coverage seen at an optical depth threshold of 2 remains at zero. This "cumulative" cloud fraction increases as more of the atmosphere is incorporated. It is important to note that opaque clouds eliminate the lidar's chance of seeing upper lever cirrus, and this plot is representative of only single layer cirrus cases. This plot is useful for showing how the altitude of a given cloud fraction changes as the optical depth threshold is varied. For example, for a given cloud fraction of 10%, there is a difference in altitude of around 3 km for an optical depth threshold of 0.03 as opposed to 2. For a fraction of 30%, there is around a 1 km difference in the average cloud height. The maximum divergence of the threshold line is around 15% for a given altitude, as in Figures 5.1 and 5.2.

5.3 Distribution of Cloud Phases Over Twelve Months of Data

Due to their height in the atmosphere, optically cirrus clouds almost always contain ice particles. For each time profile when an optical depth is calculated (optical depths between 0 and 2), the algorithm calculates the optical depths due to ice and water. For example, if a water cloud is precipitating ice and the signal penetrates the cloud top, an optical depth value is assigned to ice and a value is assigned to water. Figure 5.4 shows a distribution of ice vs. water content over the twelve-month data set.

Nearly 22% of the cases occur when the ice and water optical depths are between 0.0 and 0.1. The figure then shows that in most cases, the thin ice clouds contain very little optical depth due to water and vise versa. It is important to reiterate that only cases in which the lidar can penetrate the cloud top are contained in this image. By neglecting opaque cloud cases, it should be noted that no assumptions are made about the optical depth due to ice and water during periods of thick clouds.

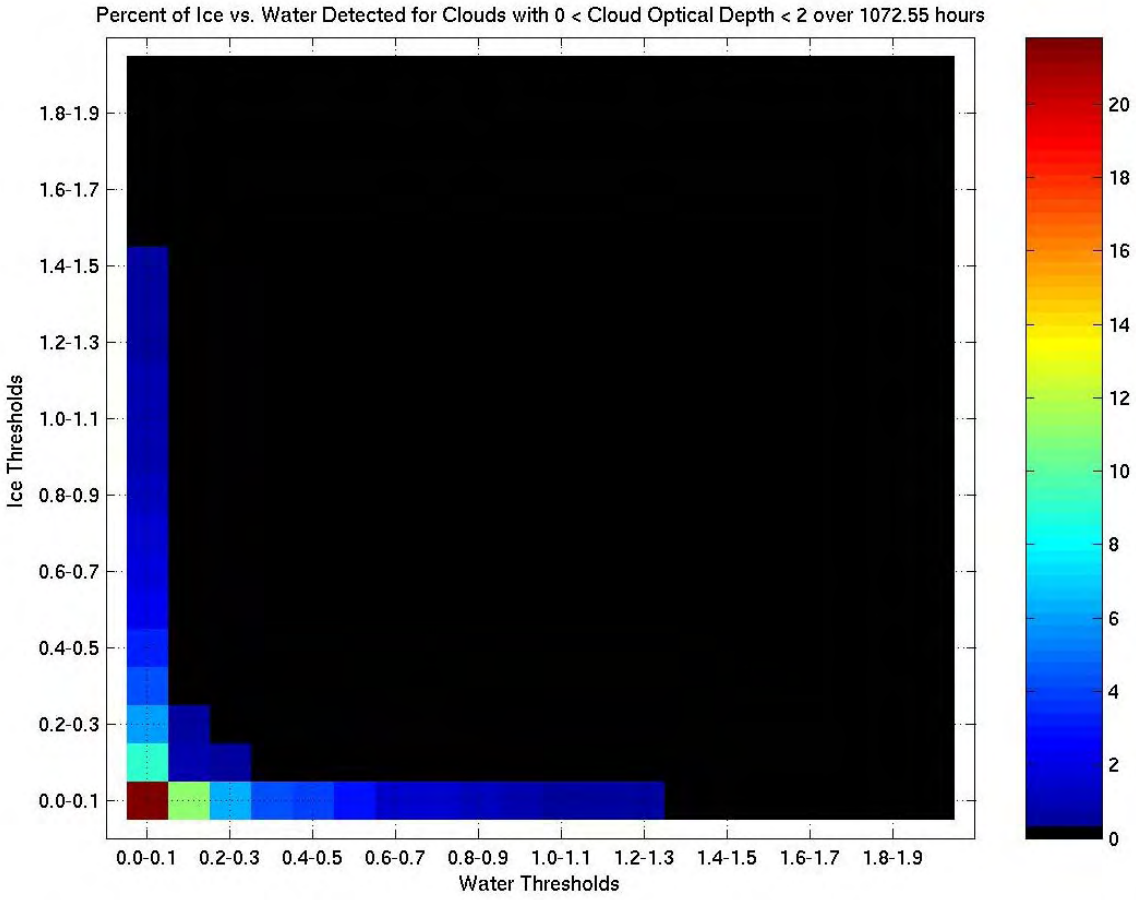

Figure 5.4 – This plot shows the distribution of ice clouds vs. water clouds over a year's worth of data as a function of optical depth thresholds. For each time profile between an optical depth of 0 and 2, the optical depth of each cloud phase is measured. This figure shows that in most cases when the lidar can penetrate the cloud top, thin ice content is associated with little or no water content, and thin water content is often linked with little or no ice content. Over 20% of the cases showed ice or water with an optical depth between 0.0 and 0.1.

5.4 Comparison with ASOS Observations at the Dane County Airport

While the previous plots in this chapter have focused on the results from twelve months of lidar data, the figures in this final section show results from the twelve individual months. Figure 5.5 shows the number of hours of data each month contains. While there is a upward trend over the course of the year due to fewer system modifications and less down-time, one cannot help but notice the lack of data in December of 2003. In the first few days of the month, the system laser began to malfunction and was shipped to the company for repairs. Data resumed just before Christmas. An important point to note is that despite the high number of hours in the early months (September through November 2003), the system was still being modified constantly, and the data gains accuracy as the months pass.

Figure 5.6 shows four data points for each month – the total cloud fraction (as defined by all clouds with an optical depth of greater than 0.05), the opaque cloud fraction (all clouds with an optical depth of greater than 2), the cloud fraction due only to single layer ice clouds, and the cloud fraction as reported by the Local Climatological Data Set gathered by NOAA at the Dane County Airport, located just 3 miles north northeast of the rooftop where the lidar collected data. The data retrieved at the Dane County Airport uses ceilometer data below 12,000 feet and satellite data with a field of view of 31x31 miles. Cloudiness was determined for each hour as a fraction of eighths. This was averaged for each month and translated into a percentage.

On the whole, it is impossible to deduct any monthly or seasonal trends from only one year's worth of data, although there does seem to be an increase in cirrus clouds over the winter months. The ice cloud fraction is not accurate of the total number of ice clouds that passed over

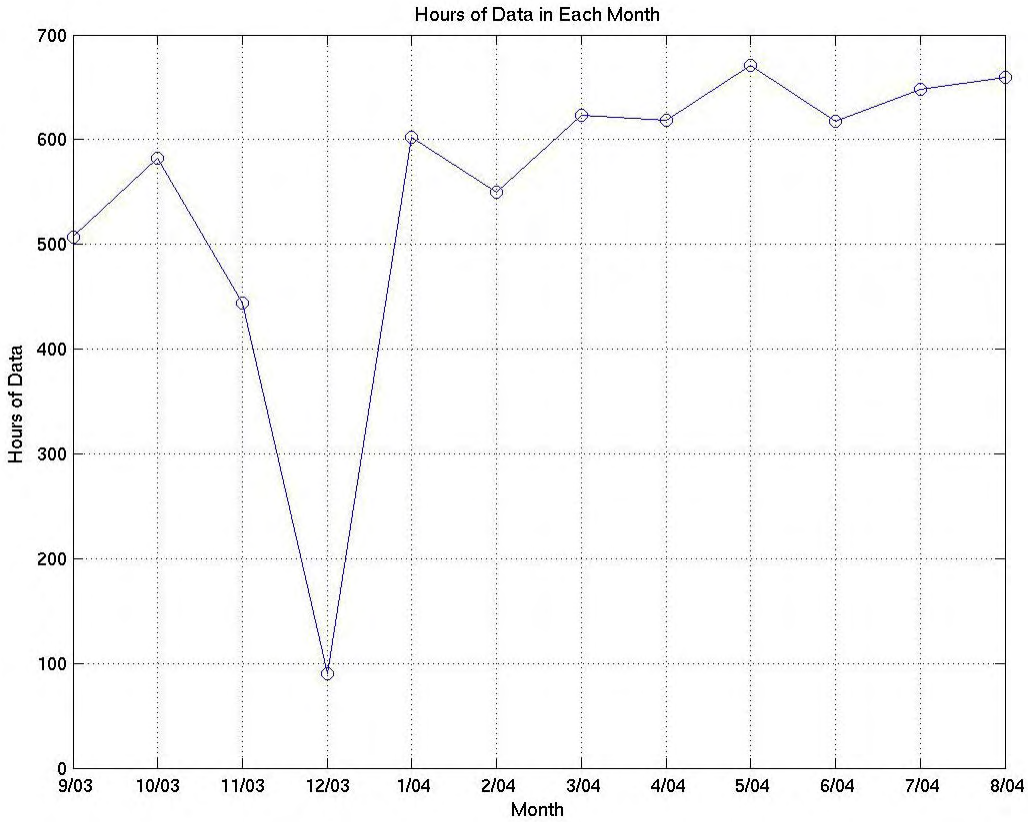

Figure 5.5 – A plot showing the number of hours of lidar data gathered in each month during operation in Madison, WI. Calibration periods and missing data have been removed, and as the months passed by, the lidar needed fewer system repairs. While there is an obvious upward trend in the amount of data gathered over the course of a year, the laser was returned to the company for repairs in December 2003, which explains the low amount of data collected.

Madison, WI, due to the lidar's inability to detect all multilayer cirrus clouds. This curve represents cirrus-only time profiles. The data gathered at the airport agrees with the lidar opaque data curve. This implies that the observations taken at the airport are recording opaque clouds and missing nearly all thin clouds. While this plot is used for a rough comparison only, the total cloud fraction as viewed by the lidar is an average value of 10-20% higher that the fraction viewed by the satellite used by the Dane County Airport.

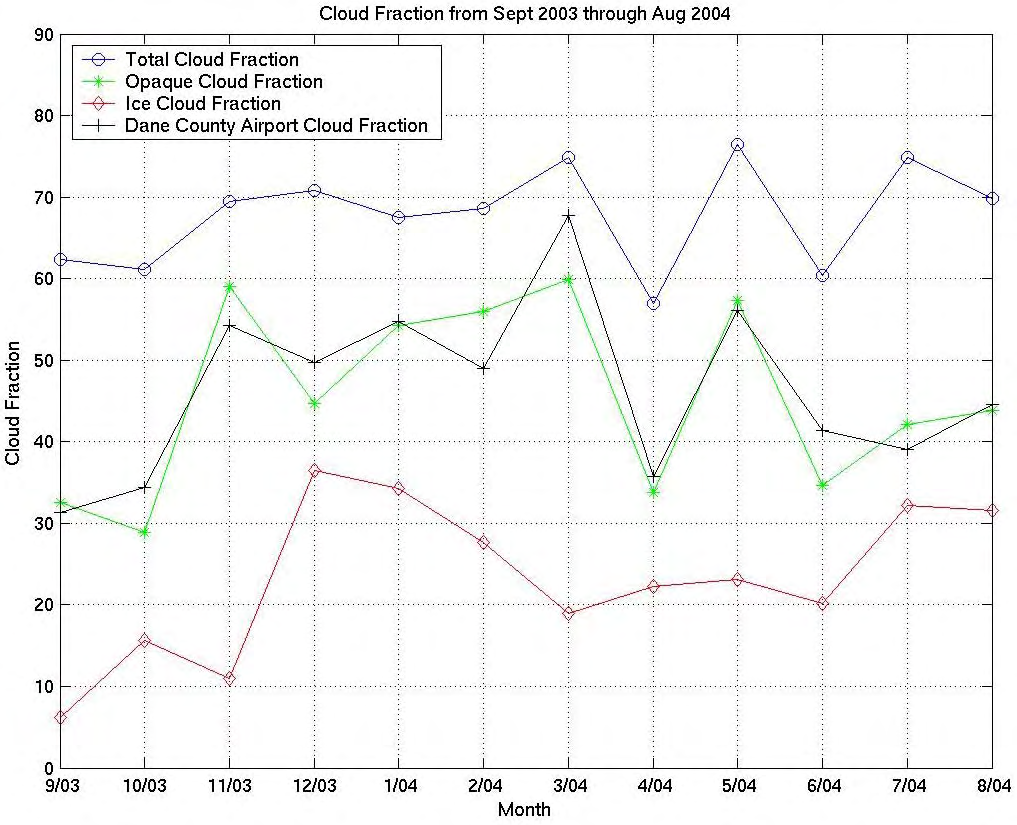

Figure 5.6 – This plot shows the cloud fraction over the course of a full year from data gathered in Madison, WI. Shown for each month is the total cloud fraction (as defined by clouds with an optical depth greater than 0.05), the opaque cloud fraction (optical depth over 2), the ice cloud fraction (cirrus clouds), and the average cloud fraction as reported at the Dane County Regional Airport. By examining the Dane County Airport cloud fraction, one can see that the Airport observations are similar to the opaque cloud fraction curve, implying that even the Airport satellite observations are missing a large fraction of clouds with a low optical depth.

Chapter 6

SUMMARY AND FUTURE WORK

Work of this nature is of great importance due to the growing need to validate satellite data with regards to optically thin cirrus. The optical depth and height of thin cirrus are often difficult to measure from satellites, and depend highly on active remote sensing instruments such as lidar for validation. The ability for scientists to confidently know the lowest detectable optical depth limit for their instrument is also of prime significance for such climatologies. The objectives and results of the four parts of this study can be summarized as:

1) Objective: Determine how the cloud percentage varies as a function of different optical depth thresholds ranging from 0.05 to 2; Result: An increase of 15% in cloud cover was observed when the optical depth threshold was changed from 0.05 to 2.
2) Objective: Study how the cloud fraction changed as a function of altitude looking from the ground up using a series of different optical depth thresholds; Result: The difference in cloud fraction increases significantly as height increases due to thinner clouds in the upper atmosphere.
3) Objective: Investigate the cloud fraction looking from above to reveal how the average cloud altitude changes when different thresholds are applied for a given cloud fraction; Result: For a given cloud fraction, there is as much as a three kilometer difference when distinguishing between thin and thick clouds.
4) Objective: Compare total cloud fraction and opaque cloud fraction over each month of the twelve-month data set; Result: Comparison with the ceilometer measurements at a near-by airport were best under the optically thick cloud conditions.

The first plot for twelve months of data (Figure 5.1) shows the total cloud percentage and Figure 5.4 reveals that in most cases, the optical depths due to water and ice are separate in the atmosphere. An increase of 15% in cloud cover was noticed when the optical depth threshold was changed from 0.05 to 2. Figure 5.2 showed how the cloud fraction varied looking from the ground up for a given altitude. The figure made clear that while the majority of clouds were in the lower 6 km, the majority of thin clouds were present above that height, as expected. The results from Figure 5.3 showed that for a given cloud fraction, the difference in average cloud altitude varies by as much as 3 km. Lastly, Figure 5.6 showed a qualitative comparison between the ice, opaque, and total cloud fractions for each month.

Although for different purposes, each part of this thesis demonstrates the importance of knowing the lowest optical depth detection limit of one's instrument in order to determine the percentage of thin clouds the instrument may not be detecting, and how the average cloud fraction would change if this percentage is known. By comparing the opaque cloud fraction for each month with data from the Dane County Airport, a reasonable effort was made to show that more research is needed in order to improve how satellites detect thin cirrus clouds.

This algorithm removed data less than one kilometer to avoid dust and haze, even at the risk of missing clouds below that vertical extent. Studies can be done dealing with the frequency of boundary layer dust and haze as well as a more specific focus on cirrus heights and optical depths. While this algorithm was developed using only lidar data, future work should include an improved comparison between lidar and satellite-derived data. Climactic trends using cloud fractions based on optical depth thresholds cannot be determined by only a year's worth of data.

References

Ackerman, Steve, Kathleen Strabala, Paul Menzel, Richard Frey, Chris Moeller, Liam Gumley, Bryan Baum, Suzanne Wetzel Seeman, and Hong Zhang). 2002. "Discriminating Clear-Sky from Cloud with MODIS Algorithm Theoretical Basis Document (MOD35)." Online. http://modis.gsfc.nasa.gov/data/atbd/atmos_atbd.html. Last viewed 6/2004.

Allen, R. J. and C. M. R. Platt. 1977. "Lidar of Multiple Backscattering and Depolarization Observations." *Applied Optics 16*: 3193-3199.

Baum, Bryan A., Richard A. Frey, Gerald G. Mace, Monica K. Harkey, Ping Yang. 2003. "Nighttime Multilayered Cloud Detection Using MODIS and ARM Data." *Journal of Applied Meteorology 42*: 905:919.

Bissonnette, L. R. 1996. "Multiple-scattering Lidar Equation." *Applied Optics 35*: 6449-6465.

Cox, Stephen K. 1971. "Cirrus Clouds and the Climate." *Journal of the Atmospheric Sciences 28*: 1513-1515.

Eloranta, E. W. 1967. "An Investigation of Lidar Pulses Doubley Scattered by Atmospheric Aerosols." MS Thesis. University of Wisconsin – Madison.

———, 1998. "Practical Model for the Calculation of Multiply Scattered Lidar Returns." *Applied Optics 37*: 2464-2472.

———, 2003. "A High Spectral Resolution Lidar for Cloud and Aerosol Optical Measurements in the Arctic." *AMS Conference on Polar Meteorology and Oceanography and Joint Symposium on High-Latitude Climate Variations. Vol. 7.*

Frey, Richard A., Bryan A. Baum, W. Paul Menzel, Steven A. Ackerman, Christopher C. Moeller, and James D. Spinhirne. 1999. "A Comparison of Cloud Top Heights Computed from Airborne Lidar and MAS Radiance Data Using CO_2 Slicing." *Journal of Geophysical Research 104*: 24,547-24,555.

Grund, C. J. 1987. "Measurement of Cirrus Cloud Optical Properties by High Spectral Resolution Lidar." Dissertation. University of Wisconsin – Madison.

———, and E. W. Eloranta. 1990. "The 27-28 October 1986 FIRE IFO Cirrus Case Study: Cloud Optical Properties Determined by High Spectral Resolution Lidar." *Monthly Weather Review 118*. 2344-2355.

Holz, Robert E. 2002. "Measurements of Cirrus Backscatter Phase Functions Using a High Spectral Resolution Lidar." MS Thesis. University of Wisconsin – Madison.

Hughes, H. G., Jerry A. Ferguson, and Donald H. Stephens. 1985. “Sensitivity of a Lidar Inversion Algorithm to Parameters Relating Atmospheric Backscatter and Extinction. Applied Optics 24: 1609-1613.

Klett, J. D. 1981 “Stable Analytical Inversion Solution for Processing Lidar Returns.” *Applied Optics 20*: 211-220.

Kuehn, Ralph E. 2001. “A Technique to Measure Cirrus Cloud Effective Particle Size Using a High Spectral Resolution Lidar.” MS Thesis. University of Wisconsin – Madison.

Léon, Jean-François, Didier Tanré, Jacques Pelon, Yoram J. Kaufman, Jim M. Haywood, and Bernadette Chatenet. 2003. “Profiling of a Saharan Dust Outbreak Based on a Synergy Between Active and Passive Remote Sensing.” *Journal of Geophysical Research 108*: SAH 2-1 – SAH 2-12.

Liou, Kuo-Nan. 1986. “Influence of Cirrus Clouds on Weather and Climate Processes: A Global Perspective.” *Monthly Weather Review 114*: 1167-1199.

Minnis, Patrick, David F. Young, Kenneth Sassen, Joseph M. Alvarez, and Christian J.Grund. 1990. “The 27-28 October 1986 FIRE IFO Cirrus Case Study: Cirrus Parameter Relationships Derived from Satellite and Lidar Data.” *Monthly Weather Review 118*: 2402-2425.

Piironen, P. 1994. “A High Spectral Resolution Lidar Based on an Iodine Absorption Filter.” Dissertation. University of Joensuu, Finland.

Platnik, Steven, Michael D. King, Steven A. Ackerman, W. Paul Menzel, Bryan A. Baum, Jérôme C. Riédi,, and Richard A. Frey. 2003. “The MODIS Cloud Products: Algorithms and Examples From Terra.” *IEEE Transactions on Geoscience and Remote Sensing 41*: 459-473.

Platt, C.M.R. 1973. “Lidar and Radiometric Observations of Cirrus Clouds.” *Journal of the Atmospheric Sciences 30*: 1191-1204.

Sassen, K. C., and James R. Campbell. 2000 – Part I. “A Midlatitude Cirrus Cloud Climatology from the Facility for Atmospheric Remote Sensing. Part I: Macrophysical and Synoptic Properties.” *Journal of the Atmospheric Sciences 58*: 481-496.

———, and Sally Benson. 2001 – Part II. “A Midlatitude Cirrus Cloud Climatology from the Facility for Atmospheric Remote Sensing. Part II: Microphysical Properties Derived from Lidar Depolarization.” *Journal of the Atmospheric Sciences 58*: 2103-2112.

———, and J. M. Comstock. 2001 – Part III. "A Midlatitude Cirrus Cloud Climatology from the Facility for Atmospheric Remote Sensing. Part III: Radiative Properties." *Journal of the Atmospheric Sciences 58*: 2113-2127.

Shipley, S. T., D. H. Tracy, E. W. Eloranta, J. T. Trauger, J. T. Sroga, F. L. Roesler, and J. A. Weinman. 1983. "High Spectral Resolution Lidar to Measure Optical Scattering Properties of Atmospheric Aerosols. 1: Theory and Instrumentation." *Applied Optics 22*: 3716-3724.

Smith, W. L., and C. M. R. Platt. 1978. "Comparison of Satellite-Deduced Cloud Heights with Indications from Radiosonde and Ground-Based Laser Measurements." *Journal of Applied Meteorology 17*: 1796-1802.

———, and R. A. Frey. 1990. "On Cloud Altitude Determinations from High Resolution Interferometer Sounder (HIS) Observations." *Journal of Applied Meteorology 29*: 658-662.

Stevens, Graeme, Si-Chee Tsay, Paul W. Stackhouse, Jr., and Piotr J. Flatau. 1990. "The Relevance of the Microphysical and Radiative Properties of Cirrus Clouds to Climate and Climatic Feedback." *Journal of the Atmospheric Sciences 47*: 1742-1753.

Stone, Robert S., Graeme L. Stephens, C. M. R. Platt, and S. Banks. 1990. "The Remote Sensing of Thin Cirrus Cloud Using Satellites, Lidar and Radiative Transfer Theory." *Journal of Applied Meteorology 29*: 353-366.

Wylie, D. P., and W. P. Menzel. 1989. "Two Years of Cloud Cover Statistics Using VAS." *Journal of Climate 2*: 380-392.

———, Paivi Piironen, Walter Wolf, and Edwin Eloranta. 1995. "Understanding Satellite Cirrus Cloud Climatologies with Calibrated Lidar Optical Depths." *Journal of the Atmospheric Sciences 52*: 4327-4343.

———, and W. Paul. Menzel. 1998. "Eight Years of High Cloud Statistics Using HIRS." *Journal of Climate 12*: 170-184

Appendix A

Instrumentation

Parameter	Value
Average transmitted power	0.5 W
Pulse repetition rate	4 KHz
Wavelength	532 nm
Telescope diameter	40 cm
Angular field of view	45 μrad
Solar noise bandwidth	8 GHz
Iodine blocking filter bandwidth	1.8 GHz
Optical detectors	2 APDs, 1 PMT
APD quantum efficiency	~ 60%
PMT quantum efficiency	~ 5%
Data acquisition	Photon counting
Range resolution	7.5 m
Max time resolution	0.5 sec

Appendix B – RESULTS FROM EACH MONTH

The following pages show each month of the data set from September 2003 through June 2004. The amount of time the system was in data-collection mode was determined by how often calibration periods were run as well as system problems. The table below shows how many days the lidar was in operation each month. This indicates non-consecutive data in that calibration periods and missing data are removed. While most months have over 25 days worth of data, November and December 2003 shows less data due to problems involving the laser. The total amount of data for the ten-month data set covered nearly 225 days of non-consecutive data.

Month	Time bins	Minutes	Hours	Days
September 2003	10145	30435	507.25	21.14
October 2003	11643	34929	582.15	24.26
November 2003	8871	26613	443.55	18.48
December 2003	1810	5430	90.5	3.77
January 2004	12051	36153	602.55	28.30
February 2004	10990	32970	549.5	22.9
March 2004	12458	37374	622.9	25.95
April 2004	12374	37122	618.7	25.78
May 2004	13413	40239	670.65	27.94
June 2004	12349	37047	617.45	25.73
Total amount of data				224.25

Important comparisons can be done between the months shown in this study. For example, the amount of cloud cover at 1 km can be identified in each "looking up from the ground" image where the optical depth threshold lines converge due to lower clouds. While September, December, and February had between 20-25% of cloud cover, the months of

November, March, and May had more precipitation, and therefore an increase in the amount of lower clouds (up to 50% cloud cover in November).

By isolating each month, the approximate height of thin clouds can also be qualitatively studied. This is seen in which altitude region the divergence of the curves occurs. For example, in September, most thin clouds are located between 3 and 8 km, while in November shows that most curves diverge between 6 and 11 km. Similarly, January shows most thin clouds are located between 4 and 10 km, and in June, a large amount of divergence occurs between 2 and 7 km.

The difference in cloud fraction between an optical depth limit of 0.03 and 2 high in the atmosphere shows the relative amount of cirrus that instruments could be missing in each month. Months such as January, February, and March have only a 10-15% increase in the detectable cloud cover. September, October, April, and June show that if an instrument had a lower optical depth threshold limit of 2, it would not detect up to 32% of thin cirrus. This is indeed a significant amount of clouds missed, and studies of this type will hopefully play some role in aiding the detection of this cirrus by satellite remote sensing instruments.

SEPTEMBER 2003

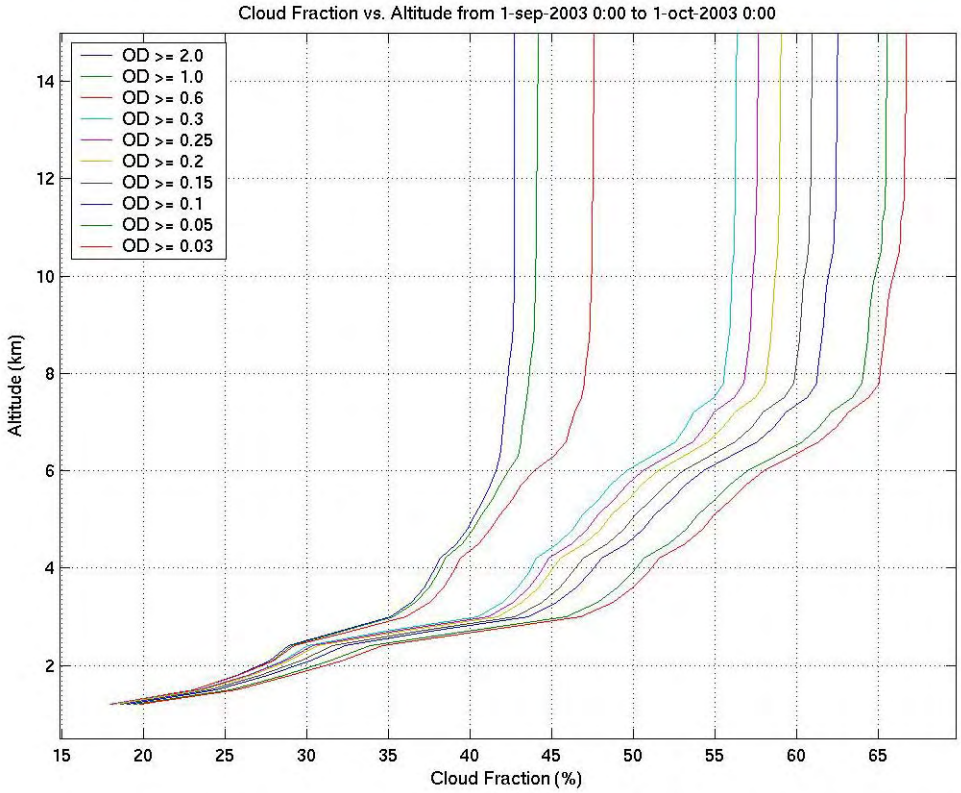

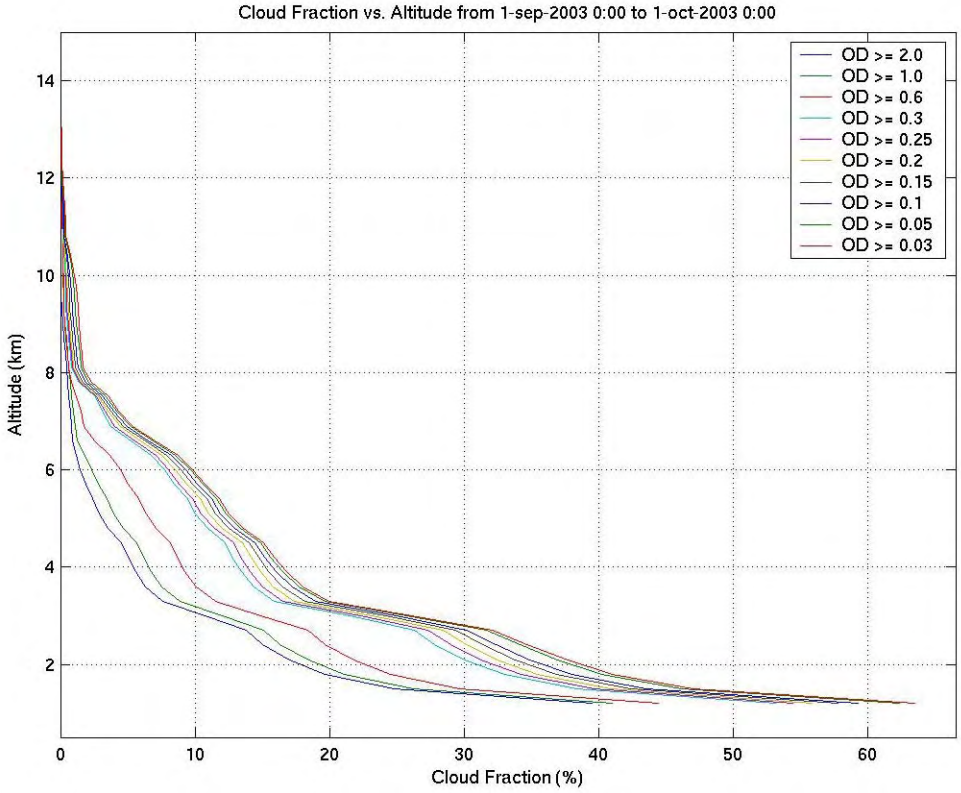

OCTOBER 2003

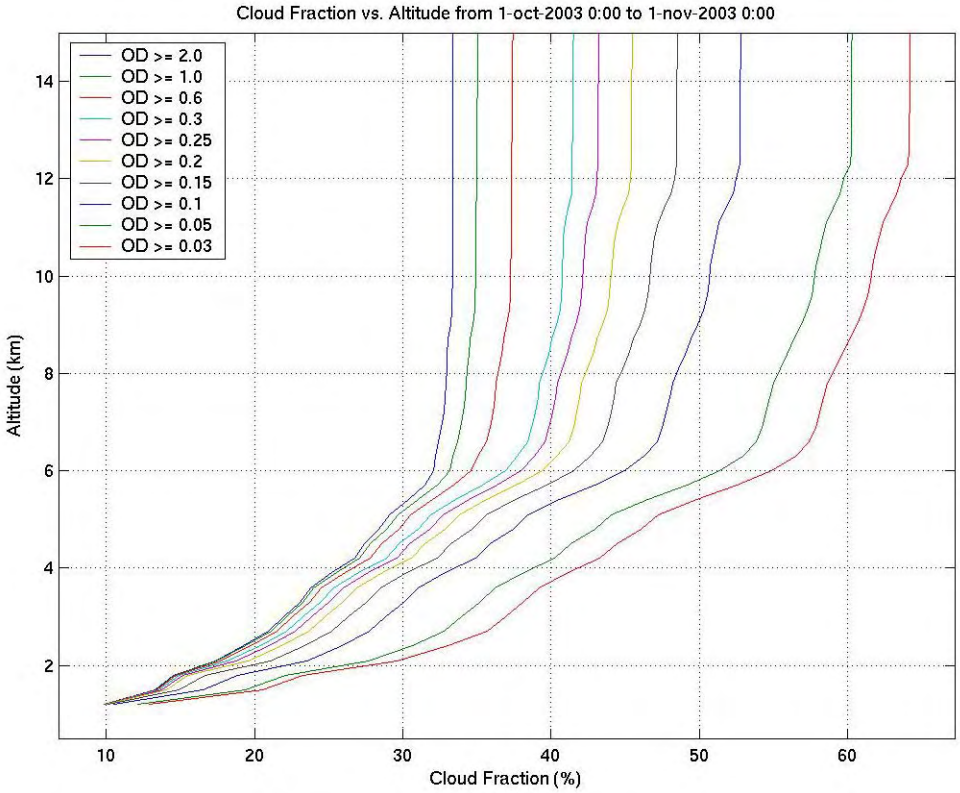

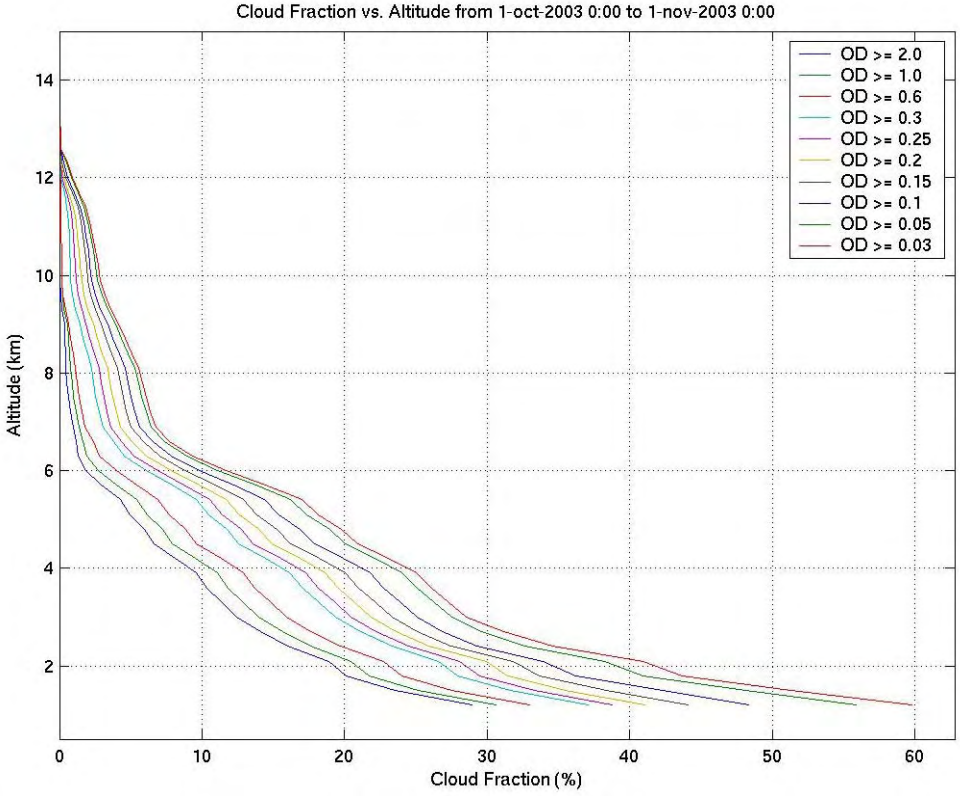

NOVEMBER 2003

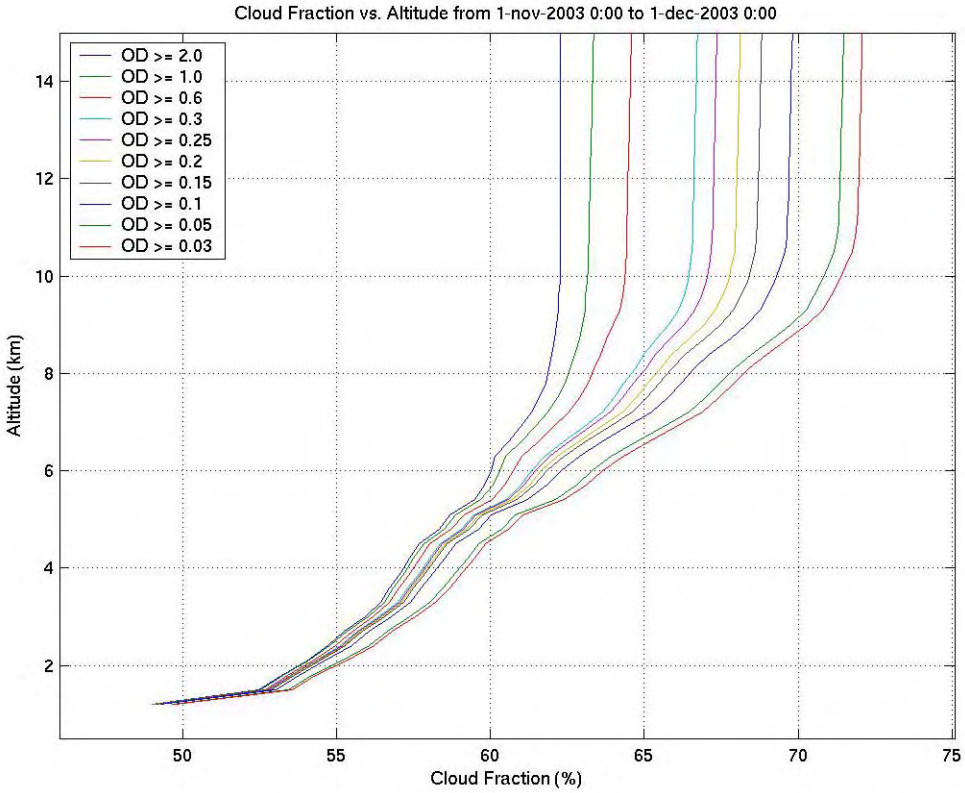

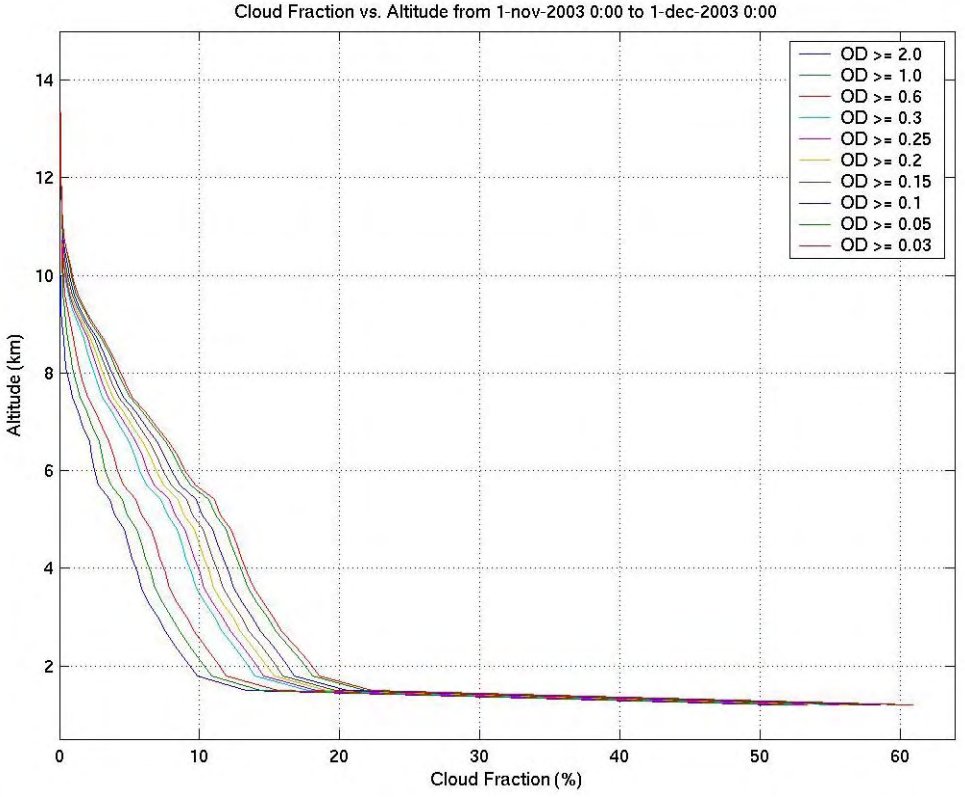

DECEMBER 2003

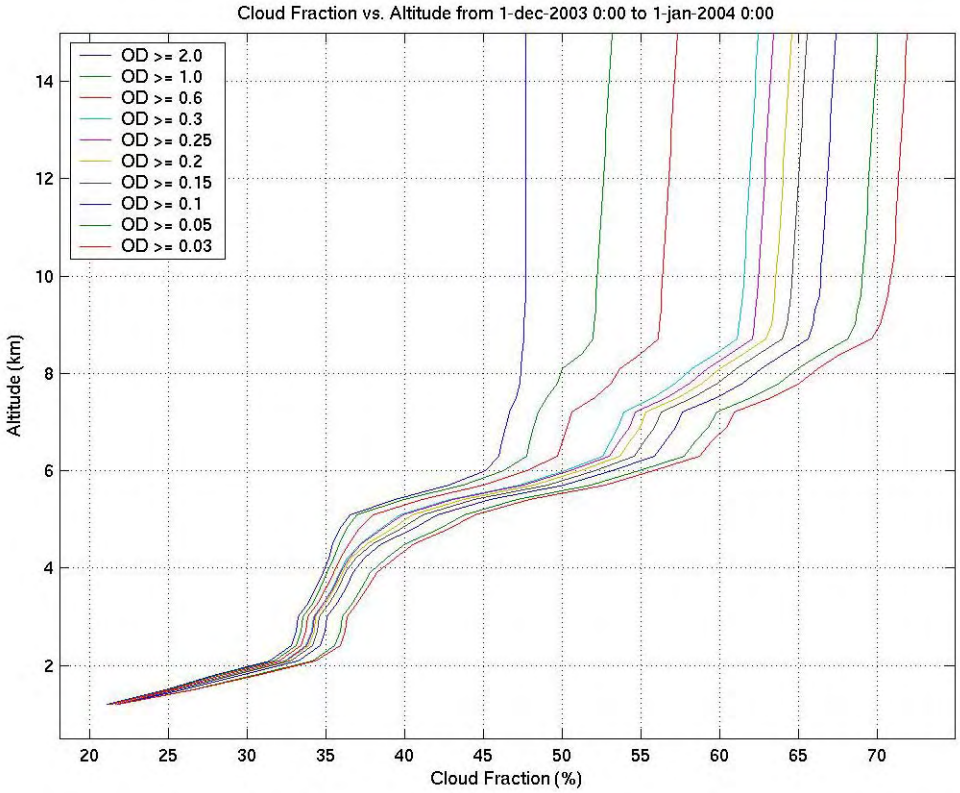

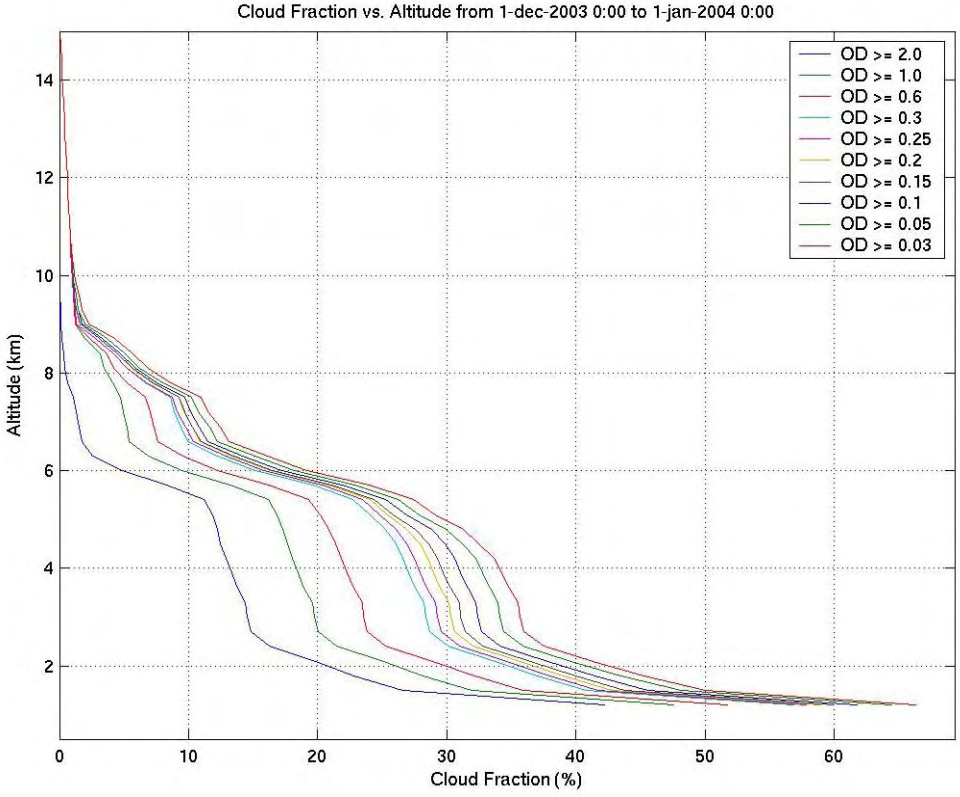

JANUARY 2004

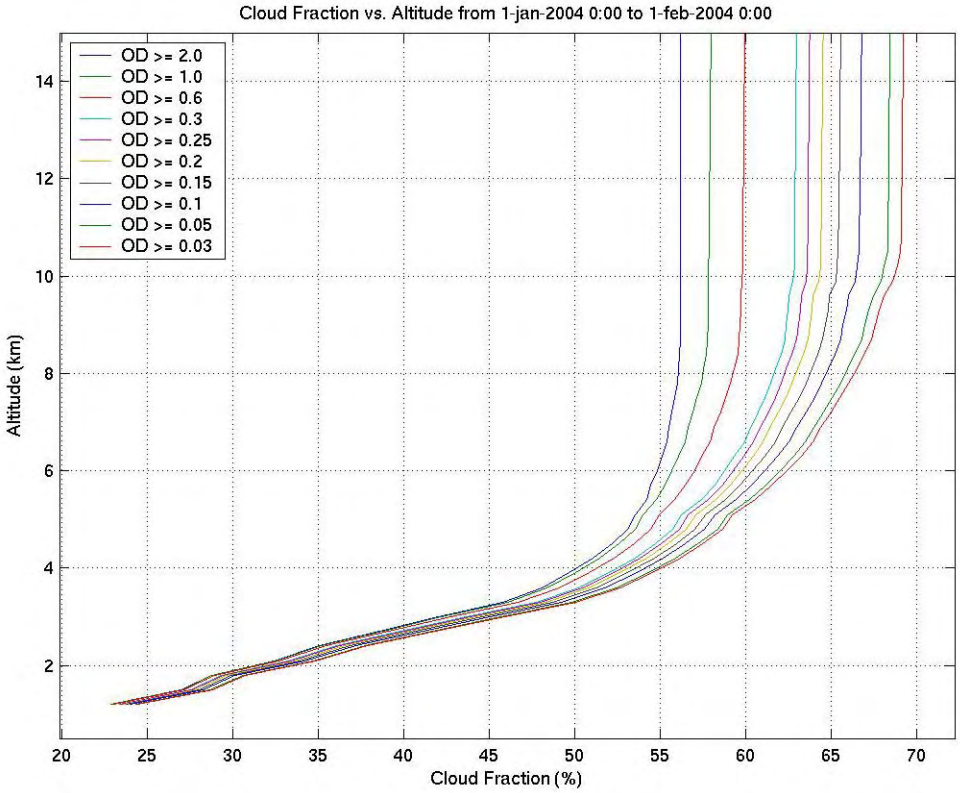

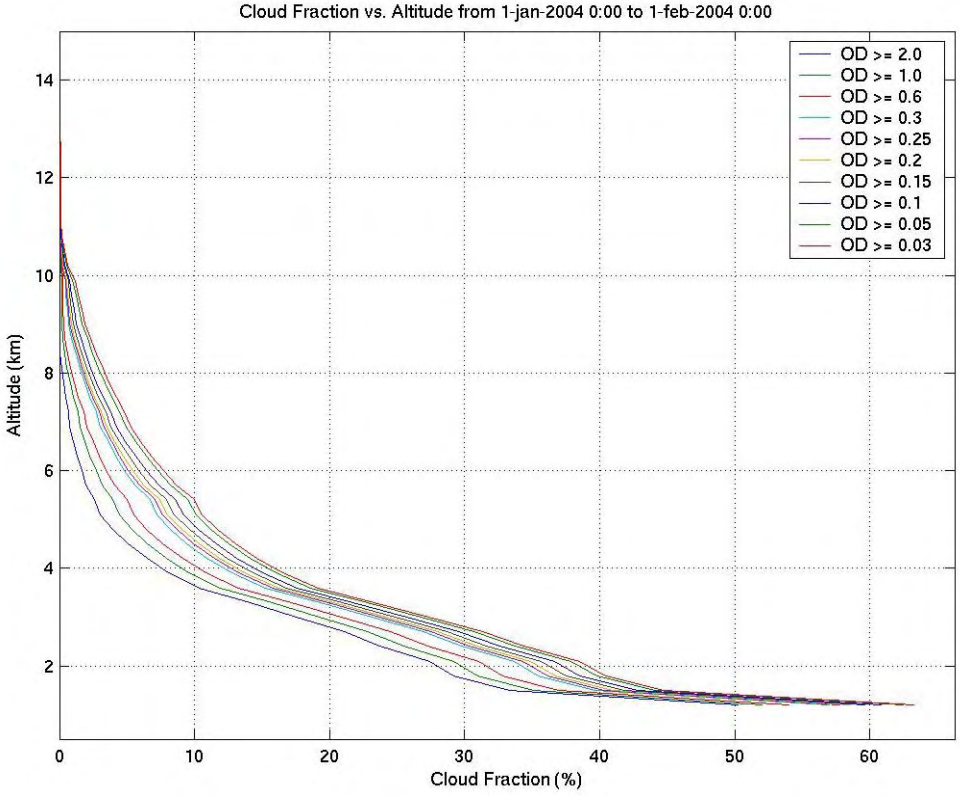

FEBRUARY 2004

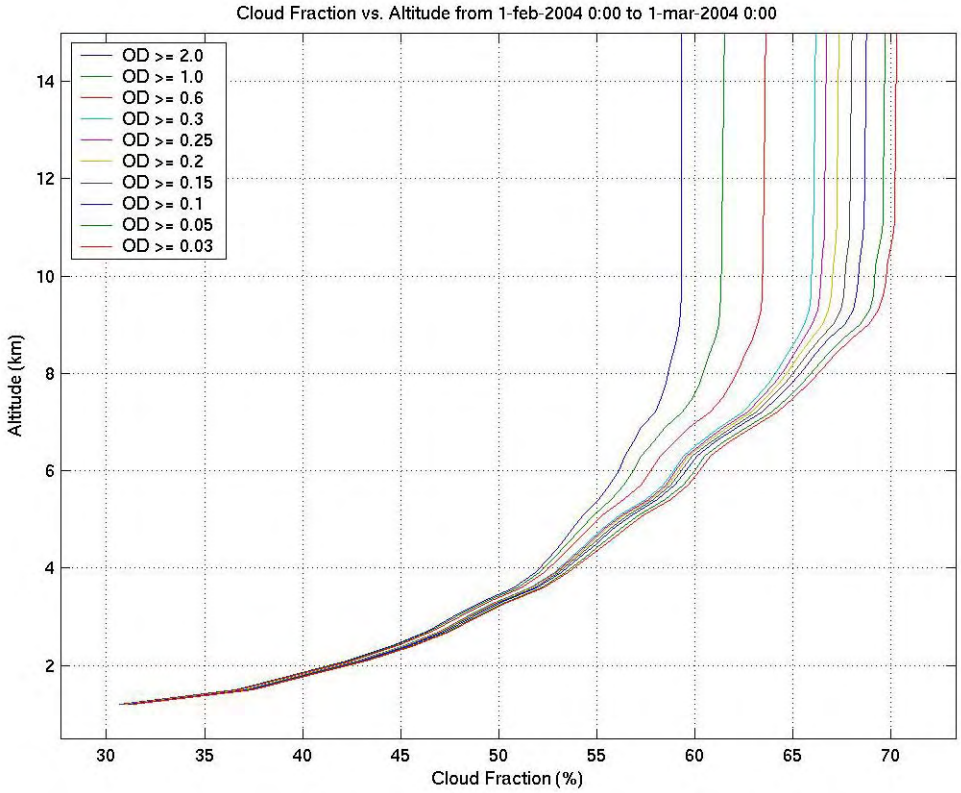

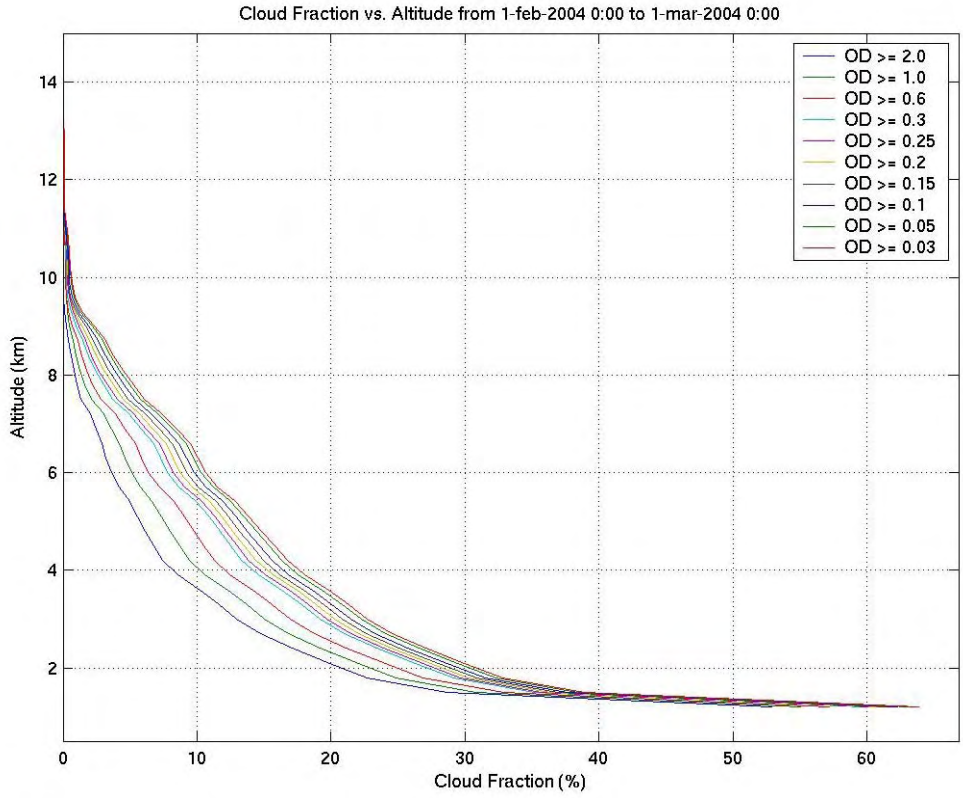

MARCH 2004

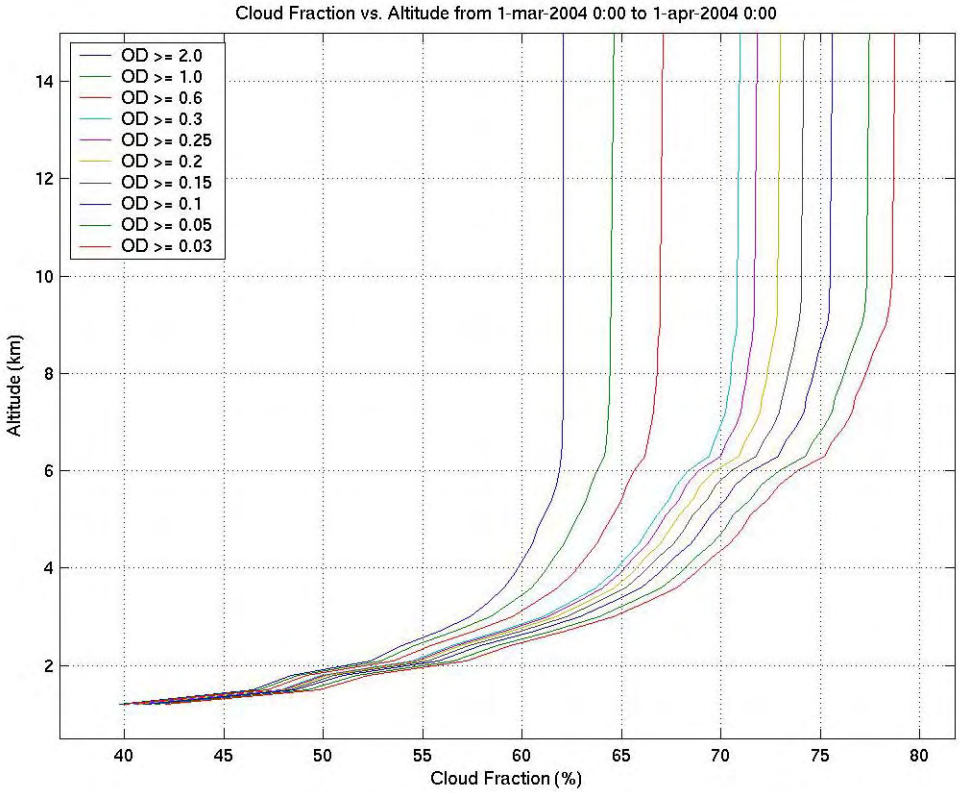
Cloud Fraction vs. Altitude from 1-mar-2004 0:00 to 1-apr-2004 0:00
OD >= 2.0
OD >= 1.0
OD >= 0.6
OD >= 0.3
OD >= 0.25
OD >= 0.2
OD >= 0.15
OD >= 0.1
OD >= 0.05
OD >= 0.03
Altitude (km)
Cloud Fraction (%)

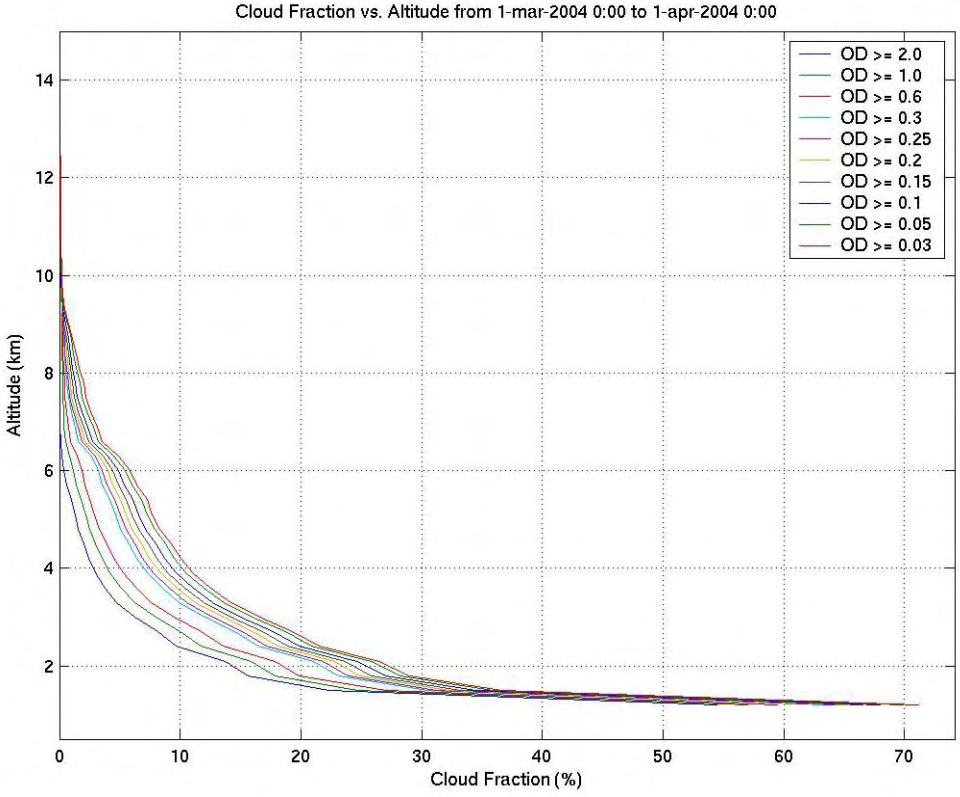
Cloud Fraction vs. Altitude from 1-mar-2004 0:00 to 1-apr-2004 0:00
OD >= 2.0
OD >= 1.0
OD >= 0.6
OD >= 0.3
OD >= 0.25
OD >= 0.2
OD >= 0.15
OD >= 0.1
OD >= 0.05
OD >= 0.03
Altitude (km)
Cloud Fraction (%)

APRIL 2004

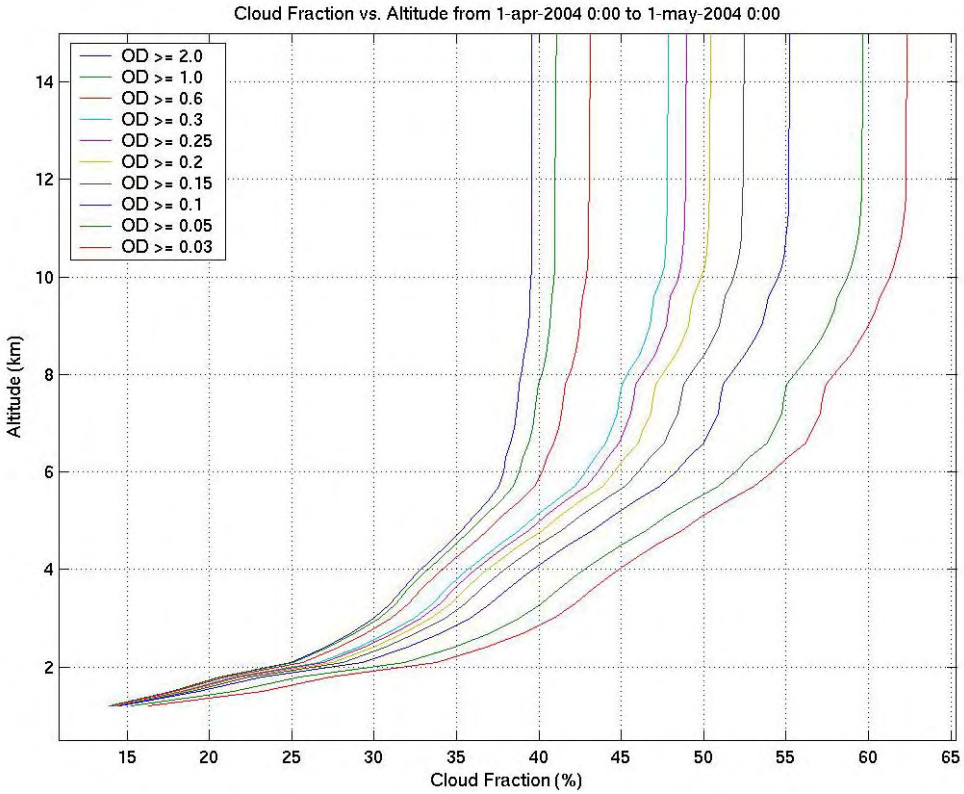
Cloud Fraction vs. Altitude from 1-apr-2004 0:00 to 1-may-2004 0:00
OD >= 2.0
OD >= 1.0
OD >= 0.6
OD >= 0.3
OD >= 0.25
OD >= 0.2
OD >= 0.15
OD >= 0.1
OD >= 0.05
OD >= 0.03
Altitude (km)
Cloud Fraction (%)

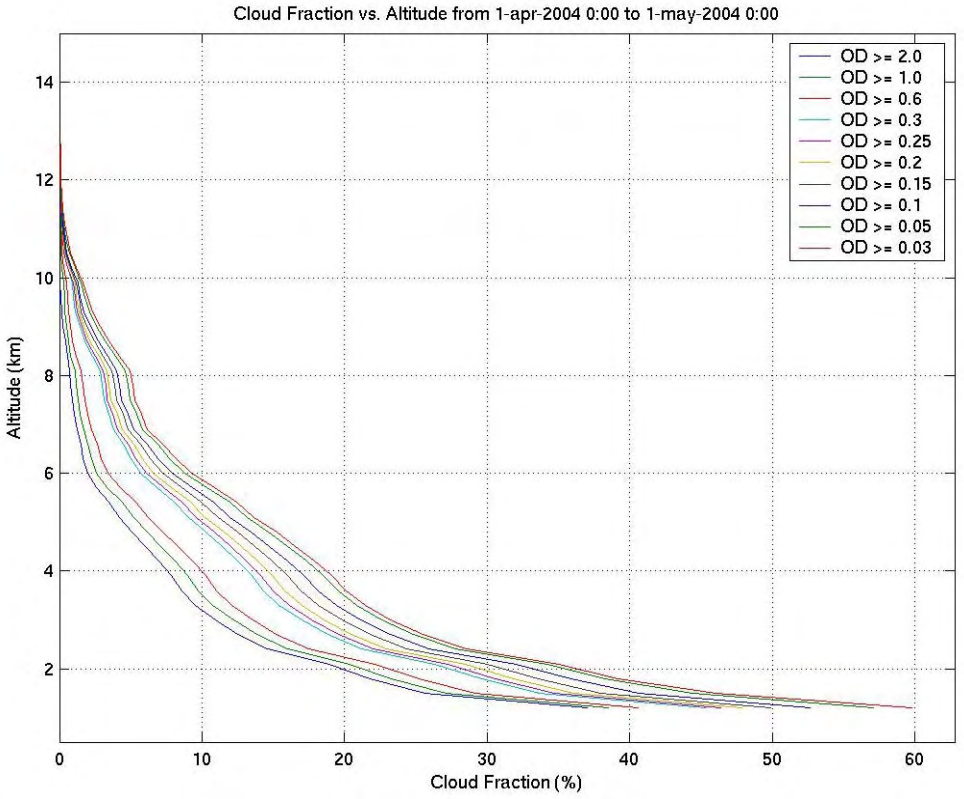
Cloud Fraction vs. Altitude from 1-apr-2004 0:00 to 1-may-2004 0:00
OD >= 2.0
OD >= 1.0
OD >= 0.6
OD >= 0.3
OD >= 0.25
OD >= 0.2
OD >= 0.15
OD >= 0.1
OD >= 0.05
OD >= 0.03
Altitude (km)
Cloud Fraction (%)

MAY 2004

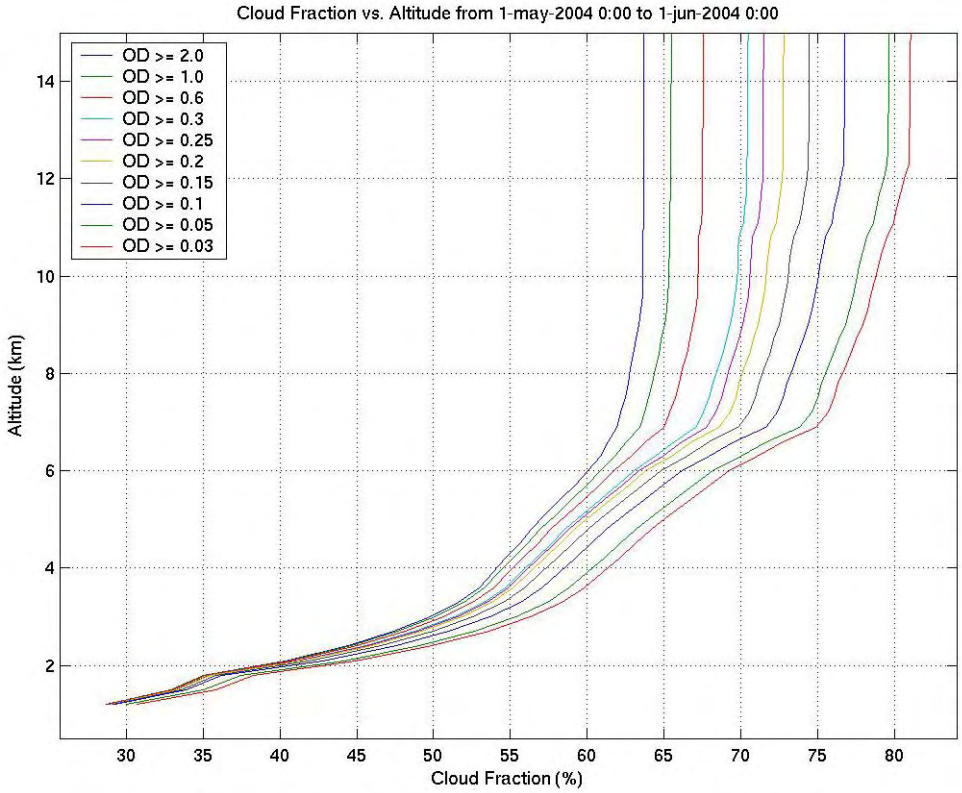
Cloud Fraction vs. Altitude from 1-may-2004 0:00 to 1-jun-2004 0:00
OD >= 2.0
OD >= 1.0
OD >= 0.6
OD >= 0.3
OD >= 0.25
OD >= 0.2
OD >= 0.15
OD >= 0.1
OD >= 0.05
OD >= 0.03
Altitude (km)
Cloud Fraction (%)

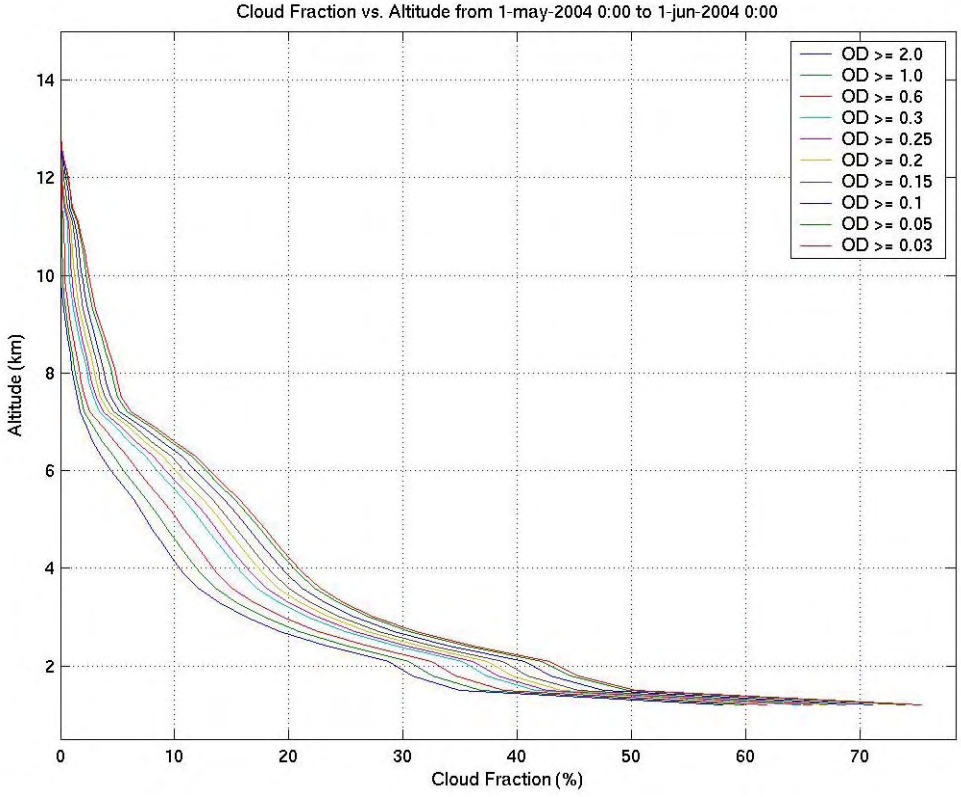
Cloud Fraction vs. Altitude from 1-may-2004 0:00 to 1-jun-2004 0:00
OD >= 2.0
OD >= 1.0
OD >= 0.6
OD >= 0.3
OD >= 0.25
OD >= 0.2
OD >= 0.15
OD >= 0.1
OD >= 0.05
OD >= 0.03
Altitude (km)
Cloud Fraction (%)

JUNE 2004

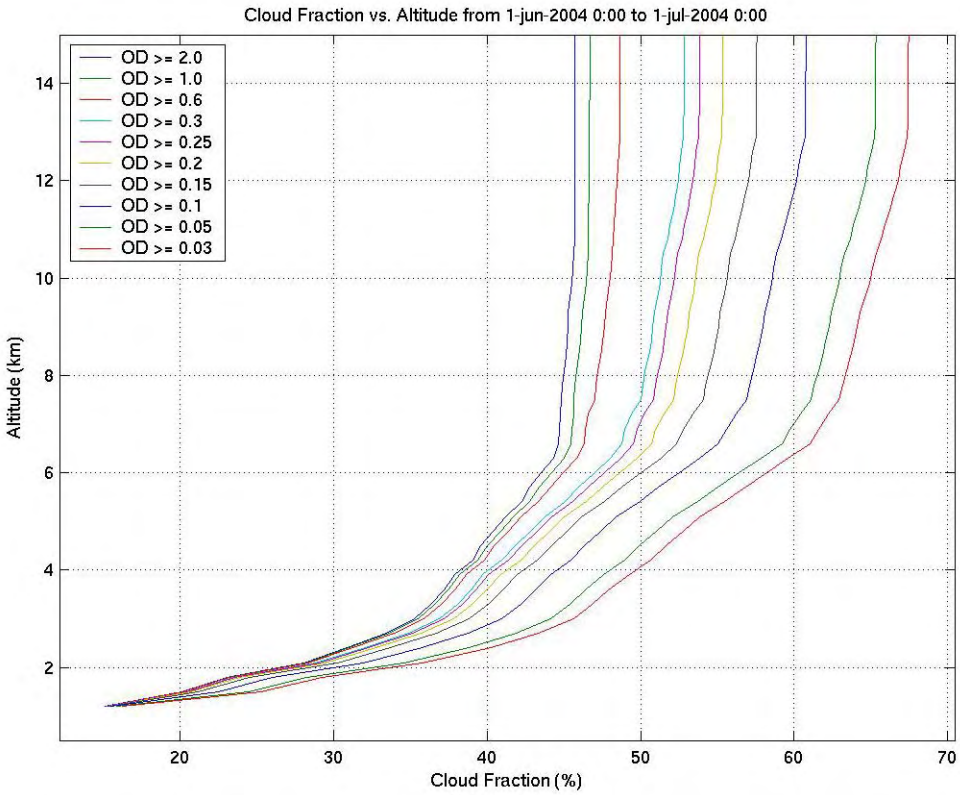
Cloud Fraction vs. Altitude from 1-jun-2004 0:00 to 1-jul-2004 0:00
OD >= 2.0
OD >= 1.0
OD >= 0.6
OD >= 0.3
OD >= 0.25
OD >= 0.2
OD >= 0.15
OD >= 0.1
OD >= 0.05
OD >= 0.03
Altitude (km)
Cloud Fraction (%)

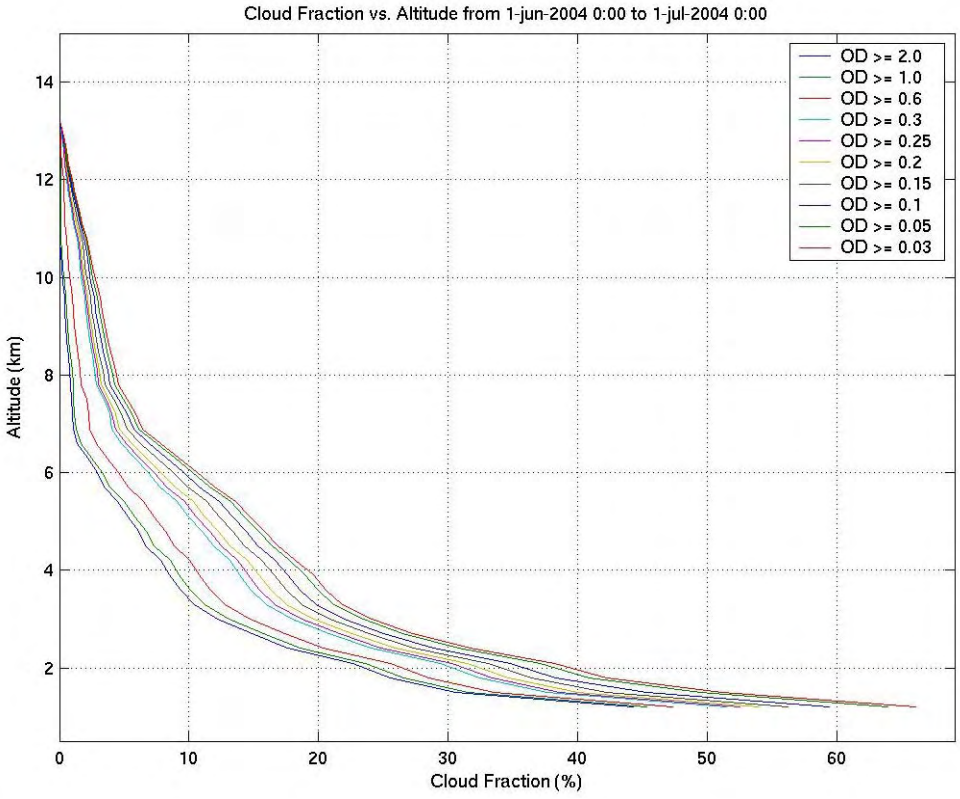
Cloud Fraction vs. Altitude from 1-jun-2004 0:00 to 1-jul-2004 0:00
OD >= 2.0
OD >= 1.0
OD >= 0.6
OD >= 0.3
OD >= 0.25
OD >= 0.2
OD >= 0.15
OD >= 0.1
OD >= 0.05
OD >= 0.03
Altitude (km)
Cloud Fraction (%)

JULY 2004

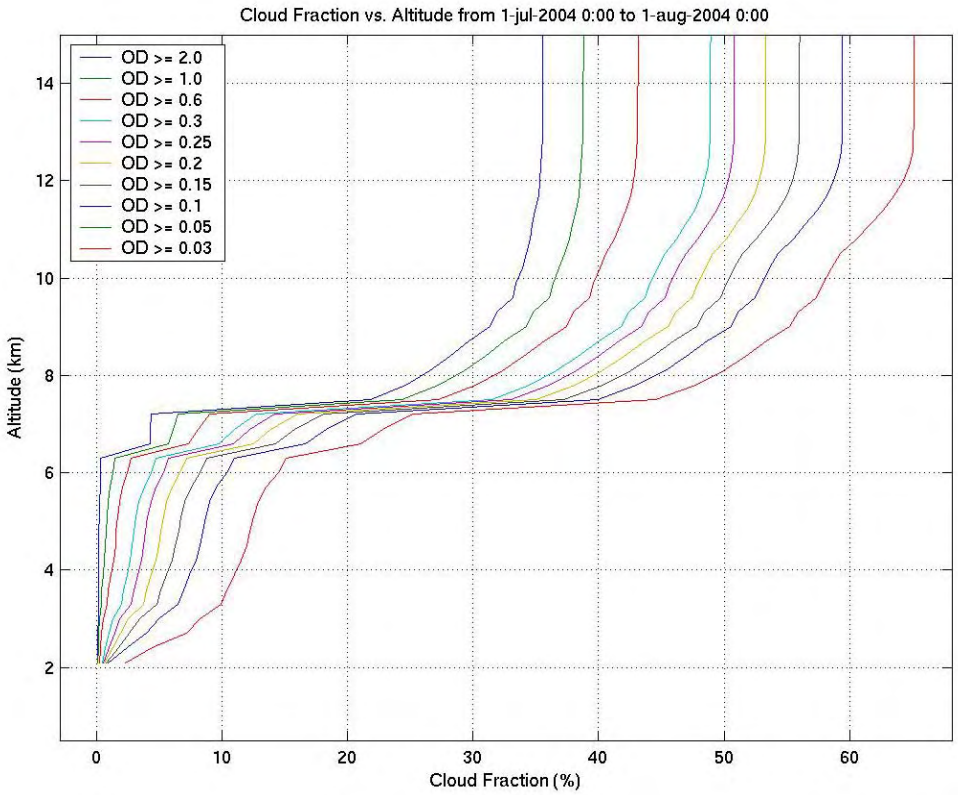
Cloud Fraction vs. Altitude from 1-jul-2004 0:00 to 1-aug-2004 0:00
OD >= 2.0
OD >= 1.0
OD >= 0.6
OD >= 0.3
OD >= 0.25
OD >= 0.2
OD >= 0.15
OD >= 0.1
OD >= 0.05
OD >= 0.03
Altitude (km)
Cloud Fraction (%)

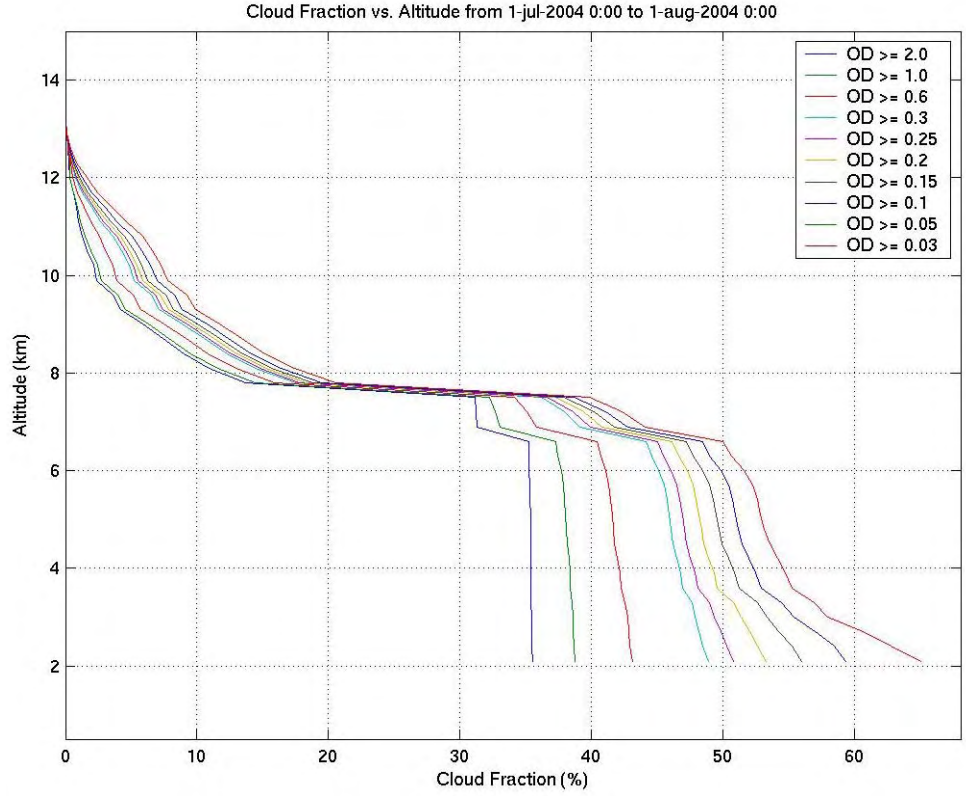
Cloud Fraction vs. Altitude from 1-jul-2004 0:00 to 1-aug-2004 0:00
OD >= 2.0
OD >= 1.0
OD >= 0.6
OD >= 0.3
OD >= 0.25
OD >= 0.2
OD >= 0.15
OD >= 0.1
OD >= 0.05
OD >= 0.03
Altitude (km)
Cloud Fraction (%)

AUGUST 2004

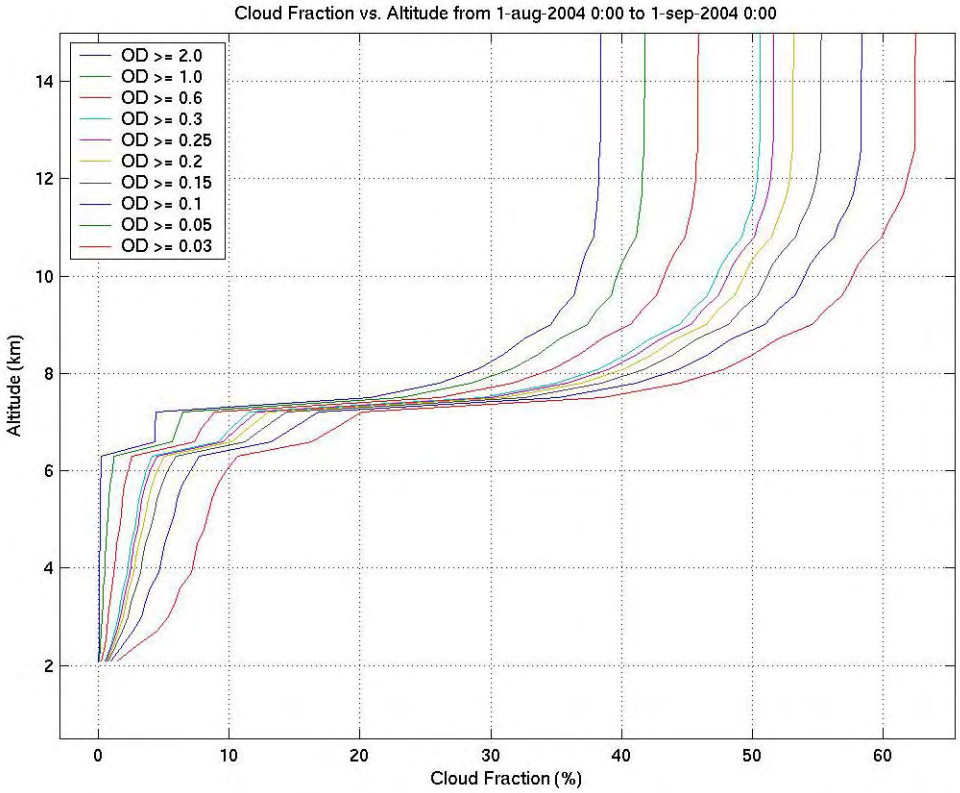
Cloud Fraction vs. Altitude from 1-aug-2004 0:00 to 1-sep-2004 0:00
OD >= 2.0
OD >= 1.0
OD >= 0.6
OD >= 0.3
OD >= 0.25
OD >= 0.2
OD >= 0.15
OD >= 0.1
OD >= 0.05
OD >= 0.03
Altitude (km)
Cloud Fraction (%)

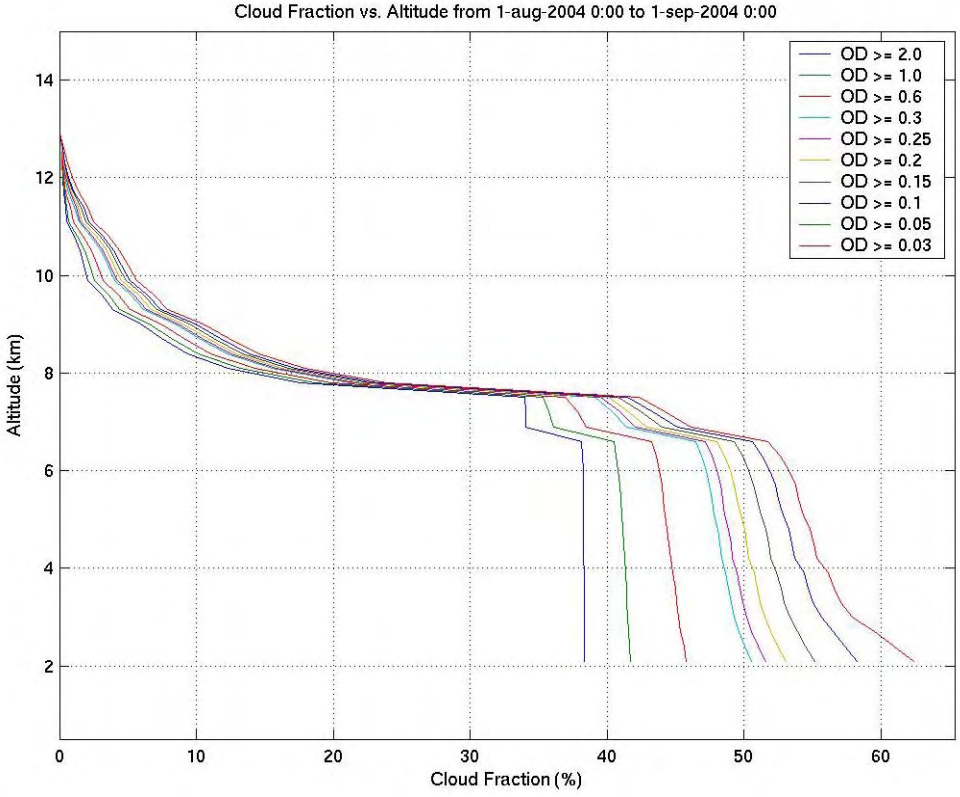
Cloud Fraction vs. Altitude from 1-aug-2004 0:00 to 1-sep-2004 0:00
OD >= 2.0
OD >= 1.0
OD >= 0.6
OD >= 0.3
OD >= 0.25
OD >= 0.2
OD >= 0.15
OD >= 0.1
OD >= 0.05
OD >= 0.03
Altitude (km)
Cloud Fraction (%)